Analysis and design of Li ion flow in the materials for batteries

Junmo Moon

Analysis and design of Li ion flow in the materials for batteries

A Doctoral Dissertation by

Junmo Moon

2023

Graduate School of Engineering,

Department of Chemical System Engineering,

Nagoya University

Table of contents

Abstract 1

Chapter 1. Background 5

1.1 Social background 5

1.2 Battery for Automobiles 5

1.2.1 lead-acid battery 5

1.2.2 Nickel metal hydride battery 6

1.2.3 Lithium-ion battery 6

1.2.4 All solid-state lithium-ion battery 6

1.3 Current and Next Batteries for automotive drive 7

1.3.1 Current battery (LIB) 7

1.3.2 Next candidate battery (All solid-state LIB) 7

1.4 Difficulty in the diffusion path of lithium ions. 7

1.5 Structure and correlation of electrode and solid electrolyte materials. 8

1.6 Multivariate analysis 8

1.7 Research Objectives 9

1.8 References at Chapter 1 9

Chapter 2. Methodology 13

2.1 Structural Evaluation 13

2.1.1 X-Ray Diffraction (XRD) 13

2.1.2 Raman spectral microscopy (Raman) 13

2.1.3 Scanning Electron Microscopy (SEM) and Energy-Dispersed X-ray Spectroscopy (EDX) 14

2.2.4 Brunauer-Emmett-Teller surface area analysis (BET) 14

2.2 Electrical Analysis 14

2.2.1 Electrochemical Impedance Evaluation 14

2.2.2 Charge and Discharge Evaluation 15

2.3 Statistical analysis 16

2.3.1 P-value 16

2.4 Reference of Chapter 2. 16

Chapter 3. Introduction of Zr ions through easy and fast synthesis to improve lithium-ion conduction for LiF solid-state electrolyte. 20

3.1 Introduction 20

3.2 Experimental 22

3.2.1 Materials 22

3.2.2 Synthesis of LiZrF and Li rich-LiZrF by liquid-mediated. 22

3.2.3 Structure characterizations. 23

3.2.4 Lithium-ion conduction performance evaluation. 23

3.3 Results and Discussion 24

3.3.1 Structure Analysis of LiZrF 24

3.3.2 Morphology Analysis of LiZrF 26

3.3.3 Analysis of lithium-ion conductivity of LiZrF 28

3.4 Conclusion 30

3.5 Reference of chapter 3 31

Chapter 4. Flow of Lithium ion in Carbon materials by Multivariate analysis. 36

4.1 Introduction 36

4.2 Experimental 38

4.2.1 Materials 38

4.2.2 Characterization of materials properties 38

4.2.3 Cell fabrication and electrochemical testing 38

4.3 Results and Discussion 40

4.3.1 Data Extraction on Multiscale 40

4.3.2 Descriptor Vector for Multivariate Analysis 42

4.3.3 Select Descriptor and verified by statistical method. 45

4.3.4 Results of applying Hill equation 49

4.3.5 Predict equation of capacity. 51

4.3.6 Candidate structure of carbon materials 52

4.4 Conclusion 53

4.5 References of chapter 4 54

4.6 Appendix of Chapter 4 57

Chapter 5. Summary 123

Achievement 125

Acknowledgement

I am truly happy to express my deep gratitude to Professor Nagahiro Saito (Department of Chemical Systems Engineering at Nagoya University) for his professional guidance and continuous encouragement to me doing this research. I think the period of research in Saito lab is the best experience and gift of my life. This experience is a weapon that can solve many challenges in life in the future and move forward, and I am confident that it will be a great strength. I would also like to thank Yasuyuki Sawada, an associate professor of chemical systems engineering at Nagoya University's Graduate School of Engineering, for his efforts to operate the laboratory. And I would like to sincerely thank associate professor Kyusung Kim (Nagoya University's Department of Chemical Systems Engineering) for his generous guidance and help in various aspects, including research counseling, thesis writing, and academic presentation. Also, I would like to sincerely thank Kondo Eriko, the head of the research department, for his continued support throughout my research period. Thank you very much for your willingness to do business until completing my PhD. I sincerely thank all the members of Saito Institute for their constant support for their advice and cooperation from the beginning of the Ph.D. course to the present. Finally, I deeply appreciate the love, care, and sacrifice of my family in educating and preparing me.

Abstract

As environmental issues are attracted much more, attention on “carbon zero” has been focused much more. Upon this attention, the demand for electric vehicles, not conventional vehicles using fossil fuels, has been increasing. However, on the current electric vehicles with lithium (Li) ion battery (LIB), once the battery is damaged by an accident, a fire may occur due to unusual reactions with Li ions caused by unexpected contact between electrodes and its exposure to air, which is a huge problem on instability. Furthermore, the current electric vehicles have disadvantages on short mileage and low charging speed of the battery. To solve these problems, two developments on the battery materials are required. One is the development of a solid-state electrolyte, which has been focused as an alternative of a liquid electrolyte for the stability, and the other is the improvement of the electrode of the battery. Therefore, active research for developing both a solid-state electrolyte and the electrode has been continued to improve mileage and charging speed with the stability. However, there have been two problems that the conductivity of Li ion in solid-state electrolytes is generally lower than that in liquid electrolytes, and the flow of Li ion in electrodes has not been known well because it has a discrepancy that it requires higher crystallinity with smaller Li ion flow. Therefore, these are the barrier to achieve the long mileage and fast charging with its stability of a battery.

From the viewpoint of the flow of Li ions in materials, the development of materials for soli d state electrolytes and electrodes would help improve the performance and stability of batteries. The refore, this research developed battery materials to improve the Li ion conductivity of stable solid-state electrolyte and the capacity of anode. For the development of a solid-state electrolyte, a novel synthesis method, which can fabricate it easily and quickly, was proposed. F urthermore, it was found that the conductivity of Li ion was improved. On the other hand, for the im provement of the performance in the anode, the parameter sets related to the characteristics were con structed and with these sets, the correlation function that can predict specific capacity and electrical c onductivity for carbon materials was successfully proposed.

In Chapter 1, a general introduction to the batteries, lithium-ion batteries, and solid-state batteries that have been used so far. In addition, lithium ions move when charging and dischargi ng with lithium-ion batteries and solid-

state batteries currently in use and under R&D. The reasons and difficulties of looking at this flow of lithium ions were explained. The structure of the material used for the solid-state electrolyte and the electrode and a method for solving the above difficulties were presented. Finally, we explained the purpose and concept of this study.

In Chapter 2, the analysis device and analysis method used in this study were introduced; XRD: for measuring the crystal structure of the material, Raman: for investigating at the crystal state of the surface, SEM: for observing the particle state on micro scale, EDX: for detecting the distribution of elements, and BET: for calculating the surface area of the material. In addition, a method for measuring Li ion conductivity and capacity, which are important for results in this study, was also introduced. Finally, because of the method to verify whether it is statistically meaningful, we conclude this chapter with an explanation of the p-value.

In Chapter 3, Zr was introduced as a substrate adding to LiF due to its stability, and LiZrF was synthesized with a simple method to improve lithium ion conductivity. quickly adding Zr into LiF through liquid methanol as a medium. The interfacial contact with the electrode, which was one of the essential factors related to the battery performance in the solid state electrolyte, was examined with SEM by mixing it with the cathode material. Compared to LiF with the cube structure, LiZrF showed rock salt structure, therefore it was found the contact would lead to be smoother movement of Li ions. As a result, it was found that Li ion conductivity was improved with the addition of Zr by changing from the FCC structure of LiF to the P31m structure of LiZrF.

In Chapter 4, the characteristics and predict equation of carbon materials used as conductive agents and anode materials in batteries were presented. On various carbon materials, such as graphite, SWCNT, MWCNT and carbon black, etc., data for the crystallinity was collected and it was examined with correlation analysis from nano to micro scales. Among these characteristics, capacity was largely influenced by the crystallinity along the c-axis, which was important factor in battery performance. In the aspect of the Li ion flow, when Li ion were intercalated between two graphene layers, the gap between the graphene layers increased, and during its intercalation, the increased area in the gap then decreased after Li ion passed away along its basal plane. Based on these results, a predict equation as well as the major factors and the phenomena for predicting capacity was proposed. As a result of validation process of the proposed function with the known results of previous research and statistical method, it was found that the function showed high predictivity.

In Chapter 5, a summary of the doctoral thesis and future directions were presented. In Chapter

1, introduction of the necessity and direction of research on a battery for electric vehicles was described. In Chapter 2, Introduction of the way to measure Li ion conductivity and capacity, including how to analyze the structure and properties of materials, and of the way to statistically verify the results was presented. In Chapter 3, the novel synthesis method of LiZrF material for improving low lithium-ion conductivity was presented with a fast and easy fabrication process, which lead to improve the Li ion conductivity as a problem of solid-state electrolyte of the battery. In Chapter 4, the high-predictable function as well as the major factors and the phenomena, which were related to the capacity of carbon materials, used as anodes and conductive agents in batteries, were presented.

This Ph.D. thesis designed and analyzed materials that will improve the stability and performance of the batteries for electric vehicles from the point of view of the Li ion flow. With considering these results, this research could provide novel and possible motivations to scientists and engineers who are dedicated to the research of battery materials and other energy devices for further improvement of its stability and performance.

Chapter 1

Background

Chapter 1. Background

1.1 Social background

As climate change worsens, the demand for "carbon zero" is also increasing. This sees climate change as the main cause of carbon dioxide and the conventional fossil fuel car, which generates large amounts of carbon dioxide, as a problem [1, 2]. As a result, interest in electric vehicles that operate electricity as an energy source, not fossil fuels, has recently been increasing [3-5]. Batteries are used to use electricity as an energy source, and the most widely used electric vehicle battery is lithium-ion battery (LIB).

1.2 Battery for Automobiles

1.2.1 lead-acid battery

Lead-acid batteries are relatively simple energy storage devices based on lead electrodes that operate in aqueous electrolytes containing sulfuric acid invented about 160 years ago [6]. It is currently used in uninterruptible power modules, electrical grids, and automotive applications, including all hybrid and LIB powered vehicles, as well as independent 12-volt supplies to support starting, lighting and ignition modules as well as critical systems when disconnecting low and high voltage batteries [6]. However, as the cell's active substances are continuously dissolved and re-deposited throughout each charge/discharge cycle, both the anode and cathode shapes and microstructures are constantly changing [6]. These structural changes generally enable corrosion of electrode grids made of pure lead, lead-calcium, or lead-antimony alloys, and have disadvantages that affect battery cycle life and material utilization efficiency. And having a lower energy density than lithium-ion batteries is also insufficient for its role as a major battery for electric vehicles.

1.2.2 Nickel metal hydride battery

A rechargeable nickel-metal hydride battery (NiMH or Ni-MH battery) is a battery that has a similar chemical reaction to a nickel-cadmium battery and uses a hydrogen-absorbing alloy for the cathode instead of cadmium [6]. The batteries are used in electric or hybrid vehicles such as Ford Ranger Ev, General Motors EV1, and Honda Electric Vehicle [6]. The NiMH battery has a longer life and better energy efficiency than the lithium-ion battery, but if the ratio, self-discharge, and charging speed are higher than C/10, gas is generated and heated from the electrode, which is mentioned as a slower charging speed than the lithium-ion battery.

1.2.3 Lithium-ion battery

Lithium-ion batteries are widely used in electric vehicles and various portable electronic devices. In a lithium-ion battery, as the name suggests, lithium ions move between the cathode and the anode to charge and discharge. Lithium-ions lighter than the lead acid or NiMH battery described above are used in various advantages, but there is a stability problem in which a fire occurs when lithium ions in a liquid electrolyte contact air and water vapor in an accident [7].

1.2.4 All solid-state lithium-ion battery

A solid-state battery is converted into a solid electrolyte rather than a liquid electrolyte and refers to a battery in which all the cathode, the anode, and the electrolyte are solid. Therefore, stability and energy density such as electrolyte leakage and combustion risk of the liquid electrolyte may also be increased [7]. However, switching from liquid to solid has the above advantages and disadvantages of decreasing the conductivity of lithium-ion. In addition, there is also a problem in that an irregular electric field caused by an interface contact problem with an electrode promotes dendritic deposition, causing a short circuit [7]. However, if the lithium-ion conductivity and interfacial contact problems are solved, they will be used as an ideal battery.

1.3 Current and Next Batteries for automotive drive

1.3.1 Current battery (LIB)

Currently, lithium-ion batteries (LIB) are commonly used as batteries for electric vehicles. It can be charged in comparison with other batteries mentioned above, due to its high energy density and high output power. However, lithium-ion batteries are still lacking in mileage and charging speed to replace conventional cars [8]. It is believed that the flow of lithium ions to the inside of the electrode material is insufficient, and the intercalation of lithium ions also is insufficient even though more lithium ions should be stored in the electrode.

1.3.2 Next candidate battery (All solid-state LIB)

Solid state batteries are promising as the next generation of lithium-ion batteries. This is because in the case of lithium-ion batteries, liquid electrolytes are used, and in the event of an accident, there is a risk of explosion or fire as the liquid electrolytes are exposed to air and water vapor [7]. To solve this problem, batteries that use solid electrolytes instead of liquid electrolytes are rising to the surface. However, since it is a solid electrolyte, there is a limitation of having lower lithium-ion conductivity than liquid electrolytes. Accordingly, the conduction of lithium-ion from the crystal structure of the solid electrolyte is to be investigated.

1.4 Difficulty in the diffusion path of lithium ions.

Both lithium-ion batteries and solid-state batteries operate as batteries as lithium-ion moves. In other words, the behavior of lithium ions determines the performance of a battery, so it is necessary to know the behavior of lithium ions. To see the flow of lithium ions, it is necessary to observe and measure lithium-ion. But this is not a simple story. This is because lithium ions are the lightest metal ions and have only two electrons, so the size of the ions is also very small [9]. To overcome these

difficulties, it would be more useful to see the interaction with the material, rather than looking directly at lithium-ion. This is because the behavior of lithium-ion will eventually be affected by the properties and structure of the material.

1.5 Structure and correlation of electrode and solid electrolyte materials.

Carbon materials are often used as anode materials [10-12]. Carbon materials are mainly made up of hexagonal rings by sp2 bonding. If these hexagonal rings continuously form a quadratic plane, they are called graphene. The size of the graphene, sp2 crystallinity, degree to which the graphene layer is stacked, etc. show the characteristics of the carbon material.

Solid electrolyte is like the carbon material mentioned above. The higher the crystallinity of the basic unit, the higher the safety, but the more difficult the material becomes to flow. On the contrary, if crystallinity is reduced through defect, the material is unstable, but the flow through the low crystallinity part improves [13-15].

In the microscale, the degree of exposure to the material packaging and ions varies by the morphology, size, and size distribution of the material. It is a property to be considered along with the properties of the material.

As the battery operates according to the flow of lithium ions, the characteristics of the material that determines the behavior of lithium ions in the nano to micro scale are important considerations. However, each of these characteristics is not independent and has a relationship with each other, so it has complexity. However, considering these matters, the diffusion of lithium-ions can be explained by various structural factors and connected to battery performance variables.

1.6 Multivariate analysis

As mentioned earlier, structural factors are correlated with each other, making it difficult to

know their effects properly. To solve this problem, there is a way to build a database by collecting various variables into data and find out their relevance. This is called multivariate analysis, and the relationship between the objective variable measured in each experiment and the explanatory variable called the structural factor is important [16]. And structural variables should be easily measured and obtained. The physical analysis of explanatory variables as object variables and the effectiveness of them are sometimes evaluated quickly using easy alternative models, which are approximations. Methods include principal component analysis (PCA) [17], multiple regression analysis [18], and cluster analysis [19]. These methods are also used in fields such as Nanomaterials, Catalyst, and Biomaterials [16].

1.7 Research Objectives

The importance of lithium-ion batteries is gaining significance with the increase in the demand for electric vehicles with "carbon zero. However, it is still insufficient to replace existing cars due to problems such as safety, mileage, and charging speed. To cope with this, solid electrolytes have excellent stability, but lithium-ion conduction is insufficient, and carbon materials used in electrodes are difficult to analyze to satisfy mileage and charging speed due to their complexity. Therefore, attention will be paid to the part where lithium ions flow in the end when charging and discharging the battery. And to solve the complexity, I would like to analyze it with multivariate analysis. Thus, the structural factors obtained from the material matrix and the dynamic behavior of lithium-ion are explained and the direction for the development of battery materials is presented.

1.8 References at Chapter 1

[1] Plass, G.N., The carbon dioxide theory of climatic change. Tellus, 1956. 8(2): p. 140-154.

[2] Madden, R.A. and V. Ramanathan, Detecting climate change due to increasing carbon dioxide. Science, 1980. 209(4458): p. 763-768.

[3] Liu, W., T. Placke, and K. Chau, Overview of batteries and battery management for electric vehicles.

Energy Reports, 2022. 8: p. 4058-4084.

[4] S. Rangarajan, S., et al., Lithium-ion batteries—The crux of electric vehicles with opportunities and challenges. Clean Technologies, 2022. 4(4): p. 908-930.

[5] Asef, P., et al., Future Trends and Aging Analysis of Battery Energy Storage Systems for Electric Vehicles. Sustainability, 2021. 13(24): p. 13779.

[6] Arun, V., et al., Review on li-ion battery vs nickel metal hydride battery in EV. Advances in Materials Science and Engineering, 2022. 2022.

[7] Huo, H., et al., A flexible electron-blocking interfacial shield for dendrite-free solid lithium metal batteries. Nature Communications, 2021. 12(1): p. 176.

[8] Marom, R., et al., A review of advanced and practical lithium battery materials. Journal of Materials Chemistry, 2011. 21(27): p. 9938-9954.

[9] Qian, J., et al., High capacity and rate capability of amorphous phosphorus for sodium ion batteries. Angewandte Chemie, 2013. 125(17): p. 4731-4734.

[10] Ogihara, N. and Y. Itou, Impedance Analysis Using Symmetric Cells for Understanding Electrochemical Behaviour of Porous Electrodes for Lithium-ion Batteries. R&D Rev. Toyota CRDL, 2017. 48: p. 17-24.

[11] Han, H., et al., Microstructure control of the graphite anode with a high density for Li ion batteries with high energy density. Electrochimica acta, 2015. 166: p. 367-371.

[12] Agubra, V. and J. Fergus, Lithium ion battery anode aging mechanisms. Materials, 2013. 6(4): p. 1310-1325.

[13] Luo, X., et al., Heterovalent cation substitution to enhance the ionic conductivity of halide electrolytes. ACS Applied Materials & Interfaces, 2021. 13(40): p. 47610-47618.

[14] Bachman, J.C., et al., Inorganic solid-state electrolytes for lithium batteries: mechanisms and properties governing ion conduction. Chemical reviews, 2016. 116(1): p. 140-162.

[15] Liang, J., et al., Metal halide superionic conductors for all-solid-state batteries. Accounts of Chemical Research, 2021. 54(4): p. 1023-1033.

[16] Le, T., et al., Quantitative structure–property relationship modeling of diverse materials properties.

Chemical reviews, 2012. 112(5): p. 2889-2919.

[17] Bro, R. and A.K. Smilde, Principal component analysis. Analytical methods, 2014. 6(9): p. 2812-2831.

[18] Darlington, R.B., Multiple regression in psychological research and practice. Psychological bulletin, 1968. 69(3): p. 161.

[19] Edwards, A.W. and L.L. Cavalli-Sforza, A method for cluster analysis. Biometrics, 1965: p. 362-375.

Chapter 2

Methodology

Chapter 2. Methodology

2.1 Structural Evaluation

2.1.1 X-Ray Diffraction (XRD)

X-Ray Diffraction is one of the most used analytical methods in materials science. When X-rays are irradiated to the material, reflections occur continuously and repeatedly in the same pattern, that is, where crystallinity exists, and record them. Depending on the type of crystallinity, it appears at the position of 2 theta related to the incident and irradiation angle [1]. Therefore, where crystallinity has developed, reflection occurs clearly and shows a sharp peak. However, in the case of amorphous, various insufficiently developed crystallinity' peak overlap and may appear broad. Quantitative analysis through the reference intensity ratio method is also possible using the ratio of peaks [2, 3]. In addition, the spacing and average size according to the type of crystal can be determined, which can be calculated by Bragg's equation and Scherrer's equation, respectively [4, 5].

2.1.2 Raman spectral microscopy (Raman)

Raman spectroscopy is an analysis device that is widely used to investigate the surface crystallinity of materials. When a sample is irradiated with a monochromatic light source according to the wavelength, the molecules that make up the sample vibrate as much as the energy absorbed and absorbed, resulting in inelastic scattering [1]. And by interpreting this, we can know the properties of the bonding of elements. For example, in the case of graphene, carbon atoms form a hexagonal shape with sp^2 bonds. However, if a hexagon such as an edge is not formed, it vibrates in breathing mode when it interacts with light and measures it [6-11].

2.1.3 Scanning Electron Microscopy (SEM) and Energy-Dispersed X-ray Spectroscopy (EDX)

Scanning electron microscopy (SEM) is a type of microscope that allows you to directly see the sample on a microscale. When electrons from SEM are accelerated and collide with the sample, secondary electrons come out from the sample [12, 13], and an image is formed based on them, and the shape, size, and surface of the sample can be observed while looking directly. Through this, factors such as aspect ratio, particle size, and size distribution can be extracted. And there is Energy-Dispersed X-ray Spectroscopy (EDX), which is commonly attached to SEM devices [13]. It is possible to interpret roughly the elemental composition of the sample by interpreting the secondary electrons for each element constituting the sample.

2.2.4 Brunauer-Emmett-Teller surface area analysis (BET)

BET is a method of obtaining a surface area by assuming that gas molecules are adsorbed on a solid surface in a multilayer structure [14]. Nitrogen gas (N_2) is widely used as a gas molecule, and the surface part can be obtained by measuring the amount of nitrogen gas adsorbed on the powder surface and calculating it in a BET method. To find the amount of nitrogen gas adsorbed, the sample is degassed under high temperature vacuum and the pressure of the adsorption gas is changed, and the adsorption amount is obtained by the pressure change of the vacuum chamber. Through this, it is used to measure the surface area per unit weight of the sample, pore size distribution, porosity, and particle size of the powder.

2.2 Electrical Analysis

2.2.1 Electrochemical Impedance Evaluation

EIS analysis is a method of interpreting the electrochemical reaction occurring between two electrodes and the electrolyte between them as an equivalent circuit [15]. The current generated by

periodically changing the direction of the AC voltage is analyzed, and resistance (R), capacitance (C), and inductance (L) are measured. Impedance Z is defined as the ratio of voltage and current of a specific frequency in an AC circuit [16-18]. Thus, impedance Z can be expressed as a V/I of a specific frequency, and the real part of impedance can be divided into resistance, and the imaginary part can be divided into capacitance and inductance. Depending on the frequency, the relationship between these two is called a Nyquist plot, and in the case of a semicircular shape, an equivalent circuit can be represented by a parallel connection of resistance and capacitance, and electrochemical characteristics can be measured through each value [16-18].

2.2.2 Charge and Discharge Evaluation

Measuring the capacity of the battery is one of the performances of the battery, and in the case of lithium-ion battery, it is one of the important purposes because lithium-ions are moved and stored with charging and discharging. First, the range of voltage is required for charging and discharging of the battery. In the case of a lithium-ion battery, the voltage is mainly used from 4.2 to 4.5 V and from 2.5 to 3 V during charging and discharging [19, 20]. It is known that overcharge is performed at a higher charging voltage and stability of the battery is degraded at a lower discharge voltage [19, 20]. In this case, the charging and discharging range was set from 3 to 4.2 V. Charging and discharging of a battery requires the entry and exit of current. However, the charging and discharging time varies depending on the magnitude of the current. This is expressed as a C-rate, and for example, the rechargeable current up to the maximum charging voltage set for 1 hour is represented as 1 C. Alternatively, if you do it for 10 hours, it is expressed as a reciprocal of 0.1 C-rate. The current corresponding to 1 C-rate may be expressed as a product of the capacity (mAh/g) of the electrode and the mass (g) of the electrode being measured.

2.3 Statistical analysis

2.3.1 P-value

The p-value, which is one of the statistical methods, is assumed to be a null hypothesis. The p-value of 0.05 is usually used for the significance level, which means that there has a correlation with a probability of 5%. If the p-value is less than or equal to 0.05, It means that there has a correlation because the null hypothesis is wrong. In other words, the lower p-value, the greater correlation between each other [21, 22].

2.4 Reference of Chapter 2.

[1] Vereda, F., Introduction to standard spectroscopic methods: XRD, IR/Raman, and Mössbauer. Iron Oxides: From Nature to Applications, 2016: p. 293-324.

[2] Hubbard, C.R. and R.L. Snyder, RIR-measurement and use in quantitative XRD. Powder Diffraction, 1988. 3(2): p. 74-77.

[3] Schreiner, W.N., A standard test method for the determination of RIR values by X-ray diffraction. Powder Diffraction, 1995. 10(1): p. 25-33.

[4] Li, Q., et al., Substrate effect on thickness-dependent friction on graphene. physica status solidi (b), 2010. 247(11-12): p. 2909-2914.

[5] Pezzini, S., et al., High-quality electrical transport using scalable CVD graphene. 2D Materials, 2020. 7(4): p. 041003.

[6] SATO, H., et al., Raman spectra and rate capability of graphite anode for lithium ion battery. Denki Kagaku oyobi Kogyo Butsuri Kagaku, 1998. 66(12): p. 1253-1259.

[7] Bar-Tow, D., E. Peled, and L. Burstein, A study of highly oriented pyrolytic graphite as a model for the graphite anode in Li-Ion batteries. Journal of the Electrochemical Society, 1999. 146(3): p. 824.

[8] Canal-Rodríguez, M., et al., Graphitized carbon xerogels for lithium-ion batteries. Materials, 2019. 13(1): p. 119.

[9] Hwang, J.U., et al., Characteristics of an artificial graphite anode material for rapid charging: manufactured with different coke particle sizes. Journal of Materials Science: Materials in Electronics, 2022. 33(25): p. 20095-20105.

[10] Im, U.-S., et al., The effect of mild activation on the electrochemical performance of pitch-coated graphite for the lithium-ion battery anode material. Materials Letters, 2020. 278: p. 128421.

[11] Ge, C., et al., Novel hard carbon/graphite composites synthesized by a facile in situ anchoring method as high-performance anodes for lithium-ion batteries. RSC advances, 2018. 8(60): p. 34682-34689.

[12] Vernon-Parry, K.D., Scanning electron microscopy: an introduction. III-Vs review, 2000. 13(4): p. 40-44.

[13] Zadora, G. and Z. Brożek-Mucha, SEM–EDX—a useful tool for forensic examinations. Materials chemistry and physics, 2003. 81(2-3): p. 345-348.

[14] Fagerlund, G., Determination of specific surface by the BET method. Matériaux et Construction, 1973. 6: p. 239-245.

[15] Günter, F.J., et al., Introduction to electrochemical impedance spectroscopy as a measurement method for the wetting degree of lithium-ion cells. Journal of The Electrochemical Society, 2018. 165(14): p. A3249.

[16] Xie, J., et al., Atomic layer deposition of stable LiAlF4 lithium ion conductive interfacial layer for stable cathode cycling. Acs Nano, 2017. 11(7): p. 7019-7027.

[17] Li, X., et al., Water-mediated synthesis of a superionic halide solid electrolyte. Angewandte Chemie, 2019. 131(46): p. 16579-16584.

[18] Zhang, D., et al., Rate-determining process at electrode/electrolyte interfaces for all-solid-state fluoride-ion batteries. ACS Applied Materials & Interfaces, 2021. 13(25): p. 30198-30204.

[19] Zhang, D., et al., Studies on capacity fade of lithium-ion batteries. Journal of Power Sources, 2000. 91(2): p. 122-129.

[20] An, S.J., et al., Fast formation cycling for lithium ion batteries. Journal of Power Sources, 2017. 342: p. 846-852.

[21] Hung, H.J., et al., The behavior of the p-value when the alternative hypothesis is true. Biometrics, 1997: p. 11-22.

[22] Panagiotakos, D.B., The value of p-value in biomedical research. The open cardiovascular medicine journal, 2008. 2: p. 97.

Chapter 3

Introduction of Zr ions through easy and fast synthesis to improve lithium-ion conduction for LiF solid-state electrolyte.

Chapter 3. Introduction of Zr ions through easy and fast synthesis to improve lithium-ion conduction for LiF solid-state electrolyte.

Crystalline lithium fluoride (LiF) with crystalline has been sought as a potential solid electrolyte (SE) due to its good electrochemical and chemical stability. However, LiF is still challenging practical SE applications due to its low lithium-ion conductivity. We propose to study the LiZrF complex-based SE by liquid-mediated synthesis. Methanol was evaluated mainly as a liquid-mediated precursor for the synthesis of LiZrF complexes under the stoichiometric ratio of LiF and ZrF_4 (2:1 and 2:0.8). The synthesized LiZrF composite was mainly Li_2ZrF_6 (*P21/c*), Li_2ZrF_6 (*P31m*), and Li_4ZrF_8 (*Pnma*) octahedral structures, which are known to have good lithium-ion conduction. Furthermore, the effect of cation Zr^{4+} stack sub-lattice on lithium-ion conduction of LiZrF complexes was investigated using Electrochemical Impedance Spectroscopy (EIS). With Zr^{4+} displacement, Li_2ZrF_6 (*P31m*)-based SE showed the highest ionic conductivity, increased to 2.40×10^{-8} S/cm and 3.89×10^{-8} S/cm, respectively, at the stoichiometric ratios of LiF and ZrF_4 2:1 (LiZrF) and 2:0.8 (Li-Rich LiZrF). In addition, the formation energy (*Ea*) of LiF shows a maximum of 0.78 eV, but the synthesized LiZrF achieves 0.21 eV formation energy (*Ea*) in the battery.

3.1 Introduction

For environmental interest and sustainable development, solid-state batteries (SSBs) are considered candidates for the next generation of battery technologies that play an essential role in adapting lithium metal anodes to high-capacity cathodes [1]. In general, SE can primarily address electrolyte leakage, combustibility, and limited energy density in liquid electrolytes [2], providing higher safety with similar operational durability and range [3,4]. Despite the above advantages, the instability of the metal anode and SE due to an interface problem between the electrode and the SE during manufacture still poses a challenge to practical use. Irregular electric field distribution due to

interfacial contact problems with electrodes may further promote dendritic deposition and result in a rapid short circuit of SSB [2]. To solve the interface, contact between the SE and the electrode, studies such as a solid polymer electrolyte (SPE), an inorganic ceramic electrolyte (ICE), and solid composite electrolytes (SCE) [5, 6] have been conducted. Among them, halide SE (fluoride, chloride, bromide, etc.) with electronegative anion compounds [7] can achieve a wide thermodynamic electrochemical stability window with electrode materials [6,8]. Crystalline LiF (Lithium Fluoride) among halide SE materials is emerging as a candidate for a wide electrochemical stability range (0-6.4 V vs Li/Li^+), a high energy density of the battery, and good chemical stability with the electrode [9, 10]. However, the strong bond between Li and F ions provides high stability for LiF, which interferes with the diffusivity of lithium ions, resulting in a low lithium-ion conductivity of 10^{-8} S/cm at RT. Therefore, it would be desirable to design a lattice structure that causes rapid diffusion of lithium-ion by preventing the binding of Li-F without compromising high electrochemical stability [9, 11]. To solve this problem, the relationship between the ion conductivity of the electrolyte and their structural arrangement is expected to improve the ion conductivity of LiF with low activation energy (*Ea*) [6, 12] while controlling the empty space, gap, gap, and partial occupancy of the lattice [13]. Therefore, the structure of Li-M-F and M as metal-transition cations can be implied in high oxidation states (: Co, Ni; : Mn, V, Cr, Ni, : Cr) [14], and the known tuning-defect chemistry can also improve the chemical structure of heterogeneous cation substitution [13, 15]. Through the empty mechanism, the lithium-ion hopping process is sensitive to active lithium-ion and empty concentrations and can induce changes in ion conductivity. However, related studies have the problem of being synthesized in energy-intensive and time-consuming paths such as high-energy ball-milling and high-temperature annealing processes [5, 9, 16-18]. To solve this problem, a method of synthesizing Li-M-F compounds in an energy-friendly and time-saving liquid-mediated synthesis path will be proposed. However, not many publications are yet able to study the synthesis of halide electrolytes for SE in aqueous solutions, such as aqueous solutions or ethanol media. In this research, LiZrF, which produced an empty cluster with tetravalent cations (Zr) through easy synthesis with methanol as a medium, energy-friendly conditions, short synthesis time, and post-treatment, was studied. Zirconium (Zr), a metal element of group 4, has the highest tetravalent atomic state and has three unique empty spaces proposed to introduce a laminated layer of stabilized metal halide structure to form LiZrF crystals. Different radial atoms are affected by the arrangement of crystal lattice based on electrostatic forces, with an atomic radius of Li^+ (0.76 Å) of Zr^{4+} (0.72 Å), which is considered a good structural engineer for determining intrinsic lithium-ion conductivity due to empty size matching. The synthesized LiZrF has a LiF_6 octahedron between a layer

of layered Li_2ZrF_6 polyhedron and a rigid skeleton as an isolated lager in the bc-plane consisting of a stabilized structure and an edge-sharing ZrF_8 polyhedron. In the Electrochemical Impedance Spectroscopy (EIS) test, when the stoichiometric ratio of LiF and ZrF_4 was synthesized differently (LiZrF and Li-Rich LiZrF) and LiF-based SE (1×10^{-8} S/cm), the conductivity of lithium was improved by 2.40×10^{-8} S/cm, and 3.89×10^{-8} S/cm. This significant relationship is consistent with the fact that crystal formation and preferred orientation have a direct effect on the polyhedron in which lithium ions can move in a crystalline conductor, allowing fast lithium-ion movement with low activation energy.

3.2 Experimental

3.2.1 Materials

LiF (Lithium fluoride) with high purity ≥99.98% trace metal basis (≤100 μm), and ZrF_4 (Zirconium (IV) fluoride) with high purity 99.9% and NCM811 ($LiNi_{0.8}Co_{0.1}Mn_{0.1}O_2$) trace metal basis and carbon black were supplied from Sigma Aldrich. Methanol, guaranteed reagent grade > 99.8% (GC) was purchased from Kanto Chemical CO., INC. PVDF (average Mw to 534,000 by Powder) and NMP (1-Methyl-2-pyrrolidone) (MW: 99.13) were provided by Sigma Aldrich. All chemical reagents were used without further purification.

3.2.2 Synthesis of LiZrF and Li rich-LiZrF by liquid-mediated.

The starting materials, high purity LiF and ZrF_4, were successfully synthesized with methanol as a solvent. The mixed suspension of Li_F, ZrF_4, and methanol was subjected to ultrasonic treatment in room temperature (RT) under air for 10 minutes. The reaction continued until the color of the entire solution was completely dissolved and transparent. Next, the homogenized transparent solution was first dried in air at 50 °C to obtain a dried powder. The obtained precursor powder was heated at 150 °C for 2 hours under vacuum. Finally, to additionally heat-treat the sample at 200 °C for 1 hour, all impurities and humidity of the organic solvent were removed in the furnace. **Fig 3.1** shows the process of preparing the LiZrF composite through a methanol solvent. To find out the lithium-ion rich state,

the sample named Li-Rich LiZrF was adjusted to 2:0.8 instead of LiZrF stoichiometric molar ratio of 2:1, and Li-Rich LiZrF obtained the same method, above-mentioned.

3.2.3 Structure characterizations.

The synthesized LiZrF crystal structure was confirmed by XRD (X-ray Diffraction Analysis) using a Rigaku SmartLab (Rigaku) machine equipped with Cu Kα irradiation (λ = 1.54056Å) with a 2θ angle range of 10-90°, a scan speed of 2°/min, and a scan step of 0.02°. The diffraction graph peak was confirmed using the JCPDS database. The composition of the LiZrF composite used the RIR (Reference Strength Ratio) method, a semi-quantitative phase analysis through the X-ray powder diffraction internal standard method, which was basically equivalent to the crystalline phase formation obtained from XRD analysis. The vacancy concentration and activation energy of ion migration used the Arrhenius equation and the Boltzmann-Einstein equation to explain the effects of other factors on the lithium-ion conductivity (luminance) of LiF, LiZrF, and Li-Rich LiZrF-based SE. Finally, element mapping and micro morphography of LiZrF composites were performed with FESEM (Field optical Scanning Electron Microscopy) in JSM 7610F machine (JEOL) equipped with EDX (Energy-Dispersed X-ray Spectroscopy).

3.2.4 Lithium-ion conduction performance evaluation.

Lithium-ion conductivity of the LiZrF (*P31m*) composite-based SE was measured using an EIS (Electrochemical Impedance Spectrometer) under small amplitude AC (Alternating Current) potential waves having different frequencies. 200 mg of the dried sample was cold compressed with a PEEK (Polyether Ether Ketone) mold having an inner diameter of 10 mm. The pellet was again inserted between a cylindrical stainless steel having a diameter of 10 mm and two steel current collectors, and a pressure of 20 MPa was applied. EIS measurements were made using Biotech's electrochemical workstation and measured in a frequency range of 1 Hz to 7 MHz. In addition, EIS measurements were performed on ion-blocking symmetric batteries to calculate the temperature dependence of LiZrF (*P31m*) composite material-based SE at temperature and frequency ranges 308 to 368 K and 1 MHz to 0.1 Hz.

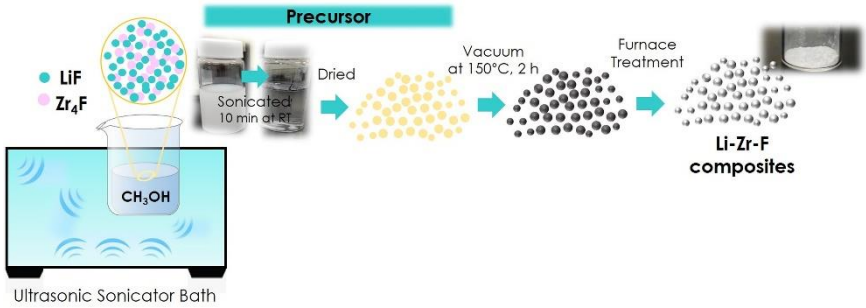

Figure 3.1. Schematic diagram of synthesize LiZrF composite via methanol-mediated synthesis.

3.3 Results and Discussion

3.3.1 Structure Analysis of LiZrF

Crystalline phase and component analysis of LiZrF products were analyzed by XRD. The considerations in the XRD database of the inorganic crystal structure database (ICSD) of the compound include a total of three phases. There are mainly three types of LiZrF products: Li_2ZrF_6 with a space group of *P31m* (PDF#72-1291) or *P21/c* (PDF#28-0611) and Li_4ZrF_8 with a space group of *Pnma* (PDF#50-1317) [19]. As illustrated in **Fig 3.2 (a)**, LiZrF synthesized based on methanol mainly forms a crystal phase of Li_2ZrF_6 (*P31m*). In addition, referring to ICSD No. PDF#72-1291, the crystallographic model of Li_2ZrF_6 (*P31m*) was shown (**Fig 3.2 (b)**).

Figure 3.2 (b) shows that the synthesized Li_2ZrF_6 is connected to the common vertex by LiF_6 and ZrF_4 octahedra with small anions and large cations [19]. And these unique vacancies and structures are expected to improve lithium-ion conductivity. In general, Li_2ZrF_6 (*P31m*) is preferred as a suitable crystal orientation for lithium-ion conductor [6, 13]. To determine the composition of LiZrF compared to LiF, the stoichiometric composition of the crystalline phase-based material was investigated from the XRD pattern, and the results using the RIR (reference intensity ratio) equation show in **Table 3.1** [20, 21]. From the results of **Table 3.1**, the synthesized LiZrF seems to be a successful synthesis because it has most of the intended Li_2ZrF_6 (*P31m*) structure as a lithium-ion conductor.

In addition, to find out more structural differences between LiZrF and Li-Rich LiZrF, the XRD

results of the two samples were shown in **Fig 3.3** and further refined by the Rietveld refinement method (**Table 3.2 and Table 3.3**), a simple method widely used to prove spatial groups, atomic coordinates, and cell size [22]. Since the site occupancy information may not be accurately obtained because of the low atomic scattering coefficients of Li and F atom, the occupancy rate of Li and F were not refined in this part. When comparing the site occupancy with the ratio of the initial reactant, the occupancy of the Zr site decreased by almost 20 % as the molar ratio of ZrF_4 decreased (Li-Rich LiZrF). Since the tetravalent replaces 4 lithium-ions around the part in which the tervalent Zr atom is introduced, lithium-ion accounts for 36.23 % of the octahedral vacancy. However, in the case of Li-Rich LiZrF, lithium-ion accounted for 39.68 %, an increase of about 10 %. Therefore, the structural characteristics, the number of vacancies in the material, and the concentration of lithium-ions could be adjusted by the molar ratio of the reactants.

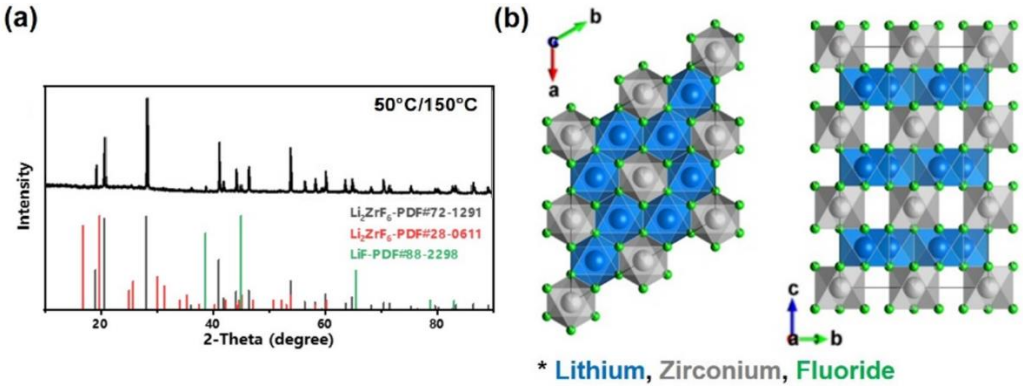

Fig 3.2 (a) XRD pattern of LiZrF composite synthesized in methanol mediated. (b) Crystallographic structure model of Li_2ZrF_6 (*P31m*).

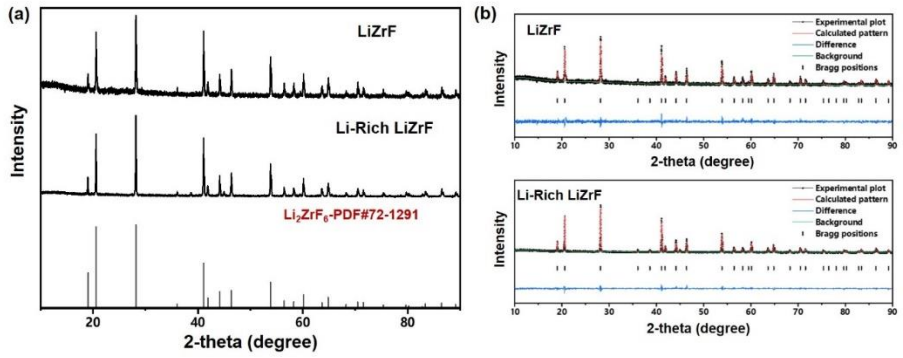

Figure 3.3 (a) XRD pattern of LiZrF and Li-Richi LiZrF, (b) the corresponding Rietveld refinements of LiZrF compared with Li-Rich LiZrF, respectively.

Table 3.1 Mass percentage of product phase composition of LiZrF composites.

Mediator	Temperature	Product Phase Composition (wt%)		
		Li_2ZrF_6 ($P\bar{3}1m$)	Li_2ZrF_6 ($P21/c$)	Li_4ZrF_8 ($Pnma$)
CH_3OH	50℃/150℃	92.6	4.1	3.3

Table 3.2 Refined parameters and crystallographic data of LiZF and Li-Rich LiZF

Sample	**LiZrF**	**Li-Rich LiZrF**
Radiation	Cu kα	
2θ interval (°)	10-90	
Rwp (%)	15.510	15.847
Space group	P-31m	
a=b (Å)	4.97418	4.97383
c (Å)	4.65695	4.65628
α=β (°)	90	
γ (°)	120	
V ($Å^3$)	99.787	99.759

Table 3.3 Rietveld refinement results of LiZrF and Li-Rich LiZrF

Sample	**Atom**	**x**	**y**	**z**	**Occ.**	**Sym.**
LiZrF	Li	0.33330	0.66670	0.50000	1.0000	m
	Zr	0.00000	0.00000	0.00000	0.8785	32
	F	0.34000	0.00000	0.26131	1.0000	-3m
Li-Rich LiZrF	Li	0.33330	0.66670	0.50000	1.0000	m
	Zr	0.00000	0.00000	0.00000	0.7550	32
	F	0.33797	0.00000	0.26089	1.0000	-3m

3.3.2 Morphology Analysis of LiZrF

FESEM analysis was performed as shown in **Fig 3.4** to investigate the difference of LiF and Li_2ZrF_6 on the macro scale. The shape of LiF showed the formation of a cube of a face-centered cubic (FCC) lattice stabilized by a strong bond of Li^+ and F^- ions (**Fig 3.4 (a) and (b)**). This shows that LiF

has the widest range of electrochemical windows [11]. However, this, in other words, the strong bond between Li^+ and F^- contributes to the high stability of LiF but limits the flow of lithium-ion [11, 13, 23]. On the contrary, the surface form of LiZrF, in which Zr ions are doped through synthesis through methanol as a medium, showed a rock-salt structure in which Zr^{4+} doping is disorderly, as illustrated in **Fig 3.4 (e) and (f)**. Empty space groups in crystal lattice, and defect chemistry are morphological changes, and this rich empty space acts as an important parameter in lithium-ion transport.

Figures 3.4 (c), (d) and (g), (h) show the shapes of the samples mixed with LiF and LiZrF, respectively, at different magnifications. LiZrF with atoms of different radii are arranged based on electrostatic forces, depending on the laminated structure of the metal halide in the ionic crystal. LiZrF showed relatively closer contact than LiF, and it is expected to provide a 3D conduction channel effective for lithium-ion diffusion because the pellet does not show a clear crack even at an ultra-high magnification. In addition, **Figure 3.5** shows SEM and energy-dispersed X-ray (EDX) mapping images of LiF (**Fig 3.5 (a) and (b)**) and LiZrF (LiF: ZrF4 2:1 (**Fig 3.5 (c-e)**) and 2:0.8 (**Fig 3.5 (f-h**)) synthesized at different stoichiometric molar ratios. As the mapping of the Zr element increased at the high concentration of ZrF_4, the mapping of the F element on the surface of the LiZrF rapidly changed. The increase in Zr element on the surface of LiZrF morphology can be seen that the synthesis of Li_2ZrF_6 was successfully carried out through methanol-mediated precursors in the state of mind.

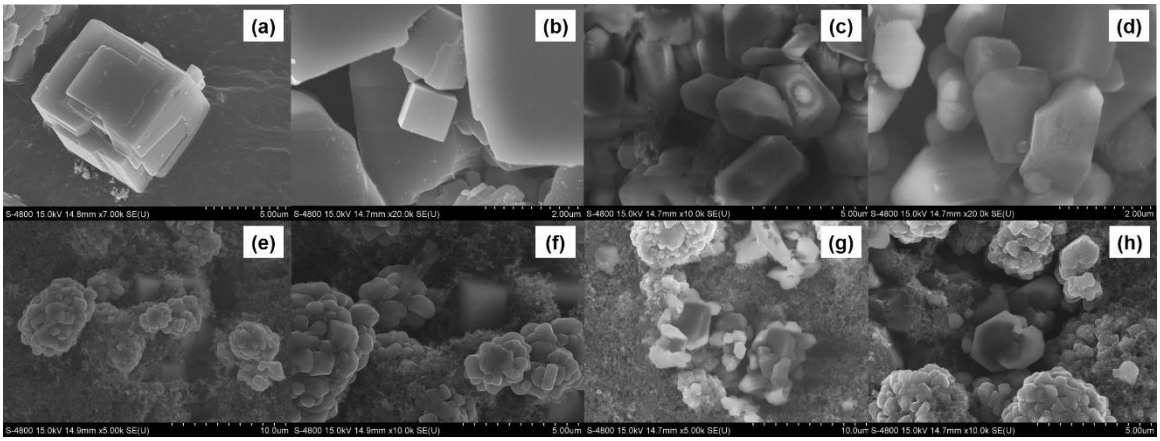

Figure 3.4 Surface morphology of (a,b) LiF particles, (c-d) Li_2ZrF_6 composite, composite cathode with (e-f) LiF, and (g-h) Li_2ZrF_6, respectively, at different magnifications.

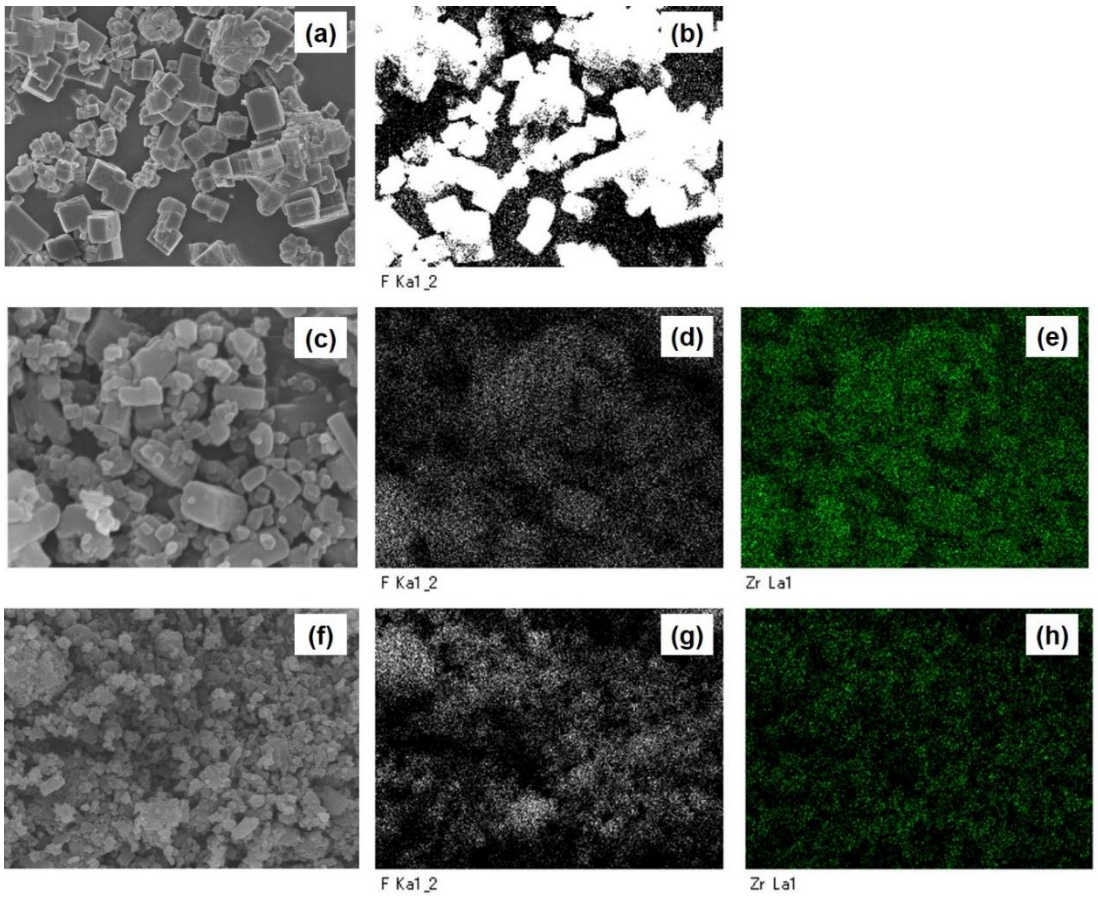

Figure 3.5 Micromorphology and EDX mapping of (a) LiF and LiZrF composite materials synthesized under different stoichiometric molar ratio of LiF: ZrF_4 (c-e) 2:1 and (f-h), 2:0.8, respectively.

3.3.3 Analysis of lithium-ion conductivity of LiZrF

EIS measurement was carried out to evaluate the conductivity of lithium-ions in the samples. It operates by applying AC potential waves of small amplitudes of different frequencies to the electrochemical system and then measuring the ratio curve of AC potential to the current signal as a sine wave frequency [9]. The real part of the impedance is equal to zero for a perfect capacitor, and the Nyquist plot is a straight recombination with the imaginary axis [9]. The lithium-ion conductivity was calculated according to **Equation (3.1)**: [9]

$$\sigma = \frac{L}{(R\ x\ S)} \qquad \text{Eq. (3.1)}$$

where σ is a lithium-ion conductivity (S/cm), R is the resistance determined from impedance spectra (Ω cm), L is sample thickness, and S is the contact area between two electrodes (cm^2).

The activation energy of ion migration in a material can be obtained by the Arrhenius equation in **Equation (3.2)**: [9]

$$\sigma = \frac{A}{T} e^{-E_a/k_B T} \quad \text{Eq. (3.2)}$$

where σ is ionic conductivity of material, A is the Arrhenius constant, E_a is the activation energy of ion migration, kB is the Boltzmann constant, and T is the Kelvin temperature. The lithium-ion conductivity of LiZrF was measured by EIS. Due to the properties of the solid structure, the effect of lithium-ion hopping in the lattice can be taken using Zr ion substitution by defeat chemistry. Due to the properties of the solid structure, the effect of lithium-ion hopping in the lattice can enhance lithium-ion conductivity using Zr ion substitution by defeat chemistry. The resistance generated by the movement of the lithium-ion within the material consists mainly of three parts: bulk resistance, grain boundary resistance, and electrode/electrolyte interface resistance. This can be seen as a parallel connection between a resistor and a capacitor in an equivalent circuit. The resistance of each part varies depending on the properties of the material, but the order of capacities is almost similar. The theoretical values for bulk capacitance, grain boundary capacitance, and electrode/electrolyte interface capacitance can be specified as 10^{-12} F, 10^{-9} F, and 10^{-6} F. In general, the lithium-ion conductivity of an SSE can be defined as the reciprocal of the sum of the bulk resistance and the grain boundary resistance [24, 25]. LiZrF, synthesized as the optimal condition as a methanol-mediated precursor, showed 0.15 eV of *Ea* and 2.40×10^{-8} S/cm of lithium-ion conductivity at RT (**Fig 3.6 (a) and (b)**).

In the crystal structure of LiZrF (*P31m*), Zr^{4+} ion substitution can introduce many empty spaces. On the other hand, the lattice structure in the halogenated metal electrolyte is affected by the radii of different metal cations. The substitution of metal ions by Zr^{4+} ions reduced *Ea* compared to *Ea* of LiF with activation energy of 0.73 eV [26], and the LiZrF composite showed a reduced Ea. It may be seen that the lithium-ion conductivity of LiZrF is significantly related to the preferred orientation and (131) plane/ (001) plane peak intensity ratio in the XRD pattern generated through the methanol-mediated precursor. The LiZrF composite material is the introduction of a tetravalent element of Zr ions, which shows excellent defect density compared to divalent and trivalent metal elements. The formation energy and lithium-ion conductivity of Li-Rich LiZrF at room temperature was 0.21 eV, 3.89×10^{-8} S/cm (**Fig 3.6 (c) and (d)**), almost double that of conventional LiZrF. And LiZrF was only 2.40×10^{-8} S/cm considered as the Boltzmann-Einstein equation [28, 29]. As shown in the relational

expression of these equations, we can see that the addition of empty space per unit volume leads to an improvement in lithium-ion migration.

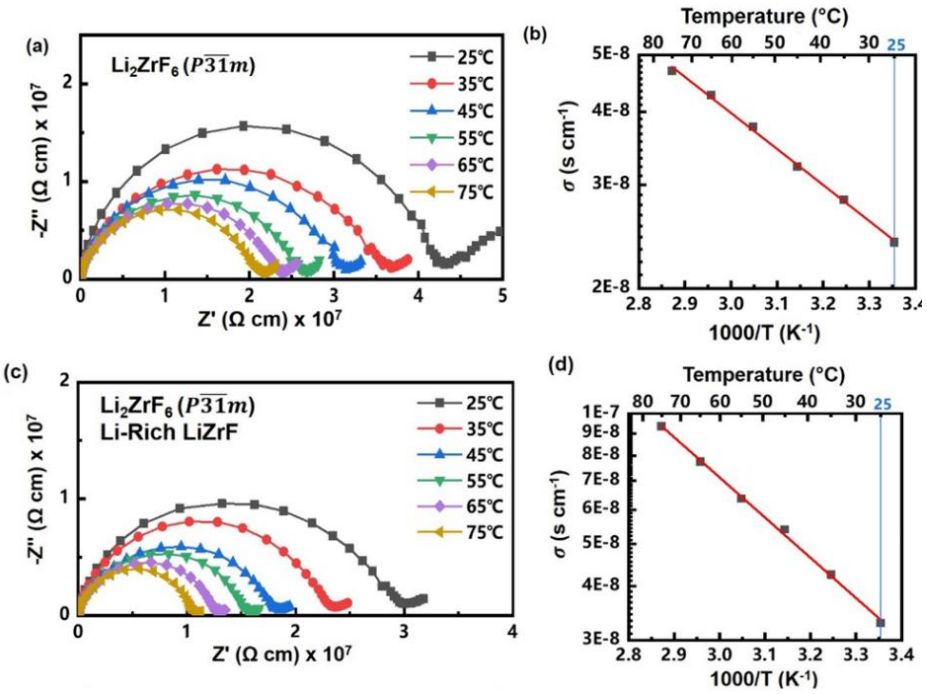

Figure 3.6 (a) Nyquist plots at different temperatures and (b) Arrhenius conductivity plot of LiZrF, (c) Nyquist plots at different temperatures and (d) Arrhenius conductivity plot of Li-Rich LiZrF, respectively.

3.4 Conclusion

In this study, a new method path with methanol precursors for simple and fast synthesis of LiZrF solid-state electrolyte and synthesized to investigate the difference in lithium-ion conductivity depending on the difference in stoichiometric molar ratio of LiF and ZrF_4. The lithium-ion conductivity of the synthesized LiZrF was increased to 2.40×10^{-8} S/cm, which is higher than 10^{-8} S/cm of LiF. It may be seen that ion transfer was reduced from 0.73 eV, which is *Ea* of LiF, to 0.15 eV. The replacement of Zr^{4+} caused LiZrF to have a lower *Ea* than LiF, and the structural framework of this metal halide LiZrF electrolyte was constructed as an anion stack sublattice, which showed excellent

electrochemical performance due to the volume and polarity of the cation species, leading to the improvement of lithium-ion conduction. Li-Rich LiZrF, which was synthesized by adjusting the ratio of the initial reactants, showed almost two times higher ion conductivity than LiZrF, but Ea slightly increased to 0.21 eV. The lithium-ion conductivity is increased due to the higher amount of Li ion regarding the amount of unit vacancy by Zr ion, but the *Ea* is increased due to the decrease in Zr ion doping. The experimental results showed the synthesis of LiZrF solid electrolyte with superionic halide simply and quickly using a methanol-mediated precursor. This study investigated the structural change of materials caused by defect and vacuum by introduced Zr and the flow of lithium-ion through the change.

3.5 Reference of chapter 3

[1] Thongwichit, N.; Li, O. L. H.; Yaowarat, W.; Saito, N.; Suriyapraphadilok, U., Adsorption of carbon dioxide by solution-plasma-synthesized heteroatom-doped carbon nanospheres. Japanese Journal of Applied Physics 2016, 55, 01AE10.

[2] Huo, H.; Gao, J.; Zhao, N.; Zhang, D.; Holmes, N. G.; Li, X.; Sun, Y.; Fu, J.; Li, R.; Guo, X., A flexible electron-blocking interfacial shield for dendrite-free solid lithium metal batteries. Nature communications 2021, 12 (1), 1-10.

[3] Zhang, Y.; Huang, J.; Saito, N.; Yang, X.; Zhang, Z.; Yang, L.; Hirano, S.-i., Layered Perovskite Lithium Yttrium Titanate as a Low-Potential and Ultrahigh-Rate Anode for Lithium-Ion Batteries. Advanced Energy Materials 2022, 12 (31), 2200922.

[4] Liao, F.; Molin, E.; van Wee, B., Consumer preferences for electric vehicles: a literature review. Transport Reviews 2017, 37 (3), 252-275.

[5] Luo, X.; Cai, D.; Wang, X.; Xia, X.; Gu, C.; Tu, J., A Novel Ethanol-Mediated Synthesis of Superionic Halide Electrolytes for High-Voltage All-Solid-State Lithium–Metal Batteries. ACS Applied Materials & Interfaces 2022, 14 (26), 29844-29855.

[6] Luo, X.; Wu, X.; Xiang, J.; Cai, D.; Li, M.; Wang, X.; Xia, X.; Gu, C.; Tu, J., Heterovalent Cation Substitution to Enhance the Ionic Conductivity of Halide Electrolytes. ACS Applied Materials &

Interfaces 2021, 13 (40), 47610-47618.

[7] Ren, Y.; Qi, Z.; Zhang, C.; Yang, S.; Ma, X.; Liu, X.; Tan, X.; Sun, S.; Cao, Y., The charge transfer of intercalated Li atoms around islands on Li-halide (F, Br, Cl) surface of SEIs: A first principles calculation. Computational Materials Science 2020, 176, 109535.

[8] Asano, T.; Sakai, A.; Ouchi, S.; Sakaida, M.; Miyazaki, A.; Hasegawa, S., Solid halide electrolytes with high lithium-ion conductivity for application in 4 V class bulk-type all-solid-state batteries. Advanced Materials 2018, 30 (44), 1803075.

[9] Xie, J.; Sendek, A. D.; Cubuk, E. D.; Zhang, X.; Lu, Z.; Gong, Y.; Wu, T.; Shi, F.; Liu, W.; Reed, E. J., Atomic layer deposition of stable LiAlF4 lithium ion conductive interfacial layer for stable cathode cycling. Acs Nano 2017, 11 (7), 7019-7027.

[10] Oi, T., Ionic conductivity of LiF thin films containing Di-or trivalent metal fluorides. Materials research bulletin 1984, 19 (4), 451-457.

[11] Zhang, B.; Zhong, J.; Zhang, Y.; Yang, L.; Yang, J.; Li, S.; Wang, L.-W.; Pan, F.; Lin, Z., Discovering a new class of fluoride solid-electrolyte materials via screening the structural property of Li-ion sublattice. Nano Energy 2021, 79, 105407.

[12] Bachman, J. C.; Muy, S.; Grimaud, A.; Chang, H.-H.; Pour, N.; Lux, S. F.; Paschos, O.; Maglia, F.; Lupart, S.; Lamp, P., Inorganic solid-state electrolytes for lithium batteries: mechanisms and properties governing ion conduction. Chemical reviews 2016, 116 (1), 140-162.

[13] Liang, J.; Li, X.; Adair, K. R.; Sun, X., Metal halide superionic conductors for all-solid-state batteries. Accounts of Chemical Research 2021, 54 (4), 1023-1033.

[14] Lieser, G.; Winkler, V.; Geßwein, H.; de Biasi, L.; Glatthaar, S.; Hoffmann, M.; Ehrenberg, H.; Binder, J. R., Electrochemical characterization of monoclinic and orthorhombic Li3CrF6 as positive electrodes in lithium-ion batteries synthesized by a sol–gel process with environmentally benign chemicals. Journal of Power Sources 2015, 294, 444-451.

[15] Van der Ven, A.; Bhattacharya, J.; Belak, A. A., Understanding Li diffusion in Li-intercalation compounds. Accounts of chemical research 2013, 46 (5), 1216-1225.

[16] Li, X.; Liang, J.; Chen, N.; Luo, J.; Adair, K. R.; Wang, C.; Banis, M. N.; Sham, T. K.; Zhang, L.; Zhao, S., Water-mediated synthesis of a superionic halide solid electrolyte. Angewandte Chemie 2019,

131 (46), 16579-16584.

[17] Feinauer, M.; Euchner, H.; Fichtner, M.; Reddy, M. A., Unlocking the potential of fluoride-based solid electrolytes for solid-state lithium batteries. ACS Applied Energy Materials 2019, 2 (10), 7196-7203.

[18] Huang, H.; Wu, H.-H.; Chi, C.; Yang, Y.; Zheng, J.; Huang, B.; Wang, S., Phase-structure-dependent Na ion transport in yttrium-iodide sodium superionic conductor Na 3 YI 6. Journal of Materials Chemistry A 2021, 9 (46), 26256-26265.

[19] Li, X.; Liang, J.; Yang, X.; Adair, K. R.; Wang, C.; Zhao, F.; Sun, X., Progress and perspectives on halide lithium conductors for all-solid-state lithium batteries. Energy & Environmental Science 2020, 13 (5), 1429-1461.

[20] Hubbard, C. R.; Snyder, R. L., RIR - Measurement and Use in Quantitative XRD. Powder Diffraction 1988, 3 (2), 74-77.

[21] Schreiner, W. N., A standard test method for the determination of RIR values by x-ray diffraction. Powder Diffraction 1995, 10 (1), 25-33.

[22] Tan, J.; Matz, J.; Dong, P.; Shen, J.; Ye, M., A growing appreciation for the role of LiF in the solid electrolyte interphase. Advanced Energy Materials 2021, 11 (16), 2100046.

[23] Sheng, O.; Jin, C.; Ding, X.; Liu, T.; Wan, Y.; Liu, Y.; Nai, J.; Wang, Y.; Liu, C.; Tao, X., A decade of progress on solid-state electrolytes for secondary batteries: Advances and contributions. Advanced Functional Materials 2021, 31 (27), 2100891.

[24] Li, X.; Liang, J.; Chen, N.; Luo, J.; Adair, K. R.; Wang, C.; Banis, M. N.; Sham, T. K.; Zhang, L.; Zhao, S.; Lu, S.; Huang, H.; Li, R.; Sun, X., Water-Mediated Synthesis of a Superionic Halide Solid Electrolyte. Angew Chem Int Ed Engl 2019, 58 (46), 16427-16432.

[25] Zhang, D.; Nakano, H.; Yamamoto, K.; Tanaka, K.; Yahara, T.; Imai, K.; Mori, T.; Miki, H.; Nakanishi, S.; Iba, H.; Watanabe, T.; Uchiyama, T.; Amezawa, K.; Uchimoto, Y., Rate-Determining Process at Electrode/Electrolyte Interfaces for All-Solid-State Fluoride-Ion Batteries. ACS Appl Mater Interfaces 2021, 13 (25), 30198-30204.

[26] Tan, J.; Matz, J.; Dong, P.; Shen, J.; Ye, M., A growing appreciation for the role of LiF in the solid electrolyte interphase. Advanced Energy Materials 2021, 11 (16), 2100046.

[27] Rietveld, H. M., A profile refinement method for nuclear and magnetic structures. Journal of Applied Crystallography 1969, 2 (2), 65-71.

[28] Tomita, Y.; Fuji-i, A.; Ohki, H.; Yamada, K.; Okuda, T., New Lithium Ion Conductor Li3InBr6 Studied by 7Li NMR. Chemistry Letters 1998, 27 (3), 223-224.

[29] Tomita, Y.; Yonekura, H.; Yamauchi, Y.; Yamada, K.; Kobayashi, K., Substitution Effect in the Ion Conductor Li3InBr6, Studied by Nuclear Magnetic Resonance. Zeitschrift für Naturforschung A 2002, 57 (6-7), 447-450.

Chapter 4

Flow of Lithium ion in Carbon materials by Multivariate analysis.

Chapter 4. Flow of Lithium ion in Carbon materials by Multivariate analysis.

Lithium-ion batteries have recently attracted attention as an energy source for transportation due to the demand for electric vehicles, but they need to improve their short mileage and slow charging speed compared to existing gasoline vehicles. To overcome this problem, it is required to understand the behavior of lithium-ion in carbon materials used as anode materials in batteries. Accordingly, in this study, a target variable was experimentally obtained to construct a dataset by extracting characteristic-related factors from a total of 21 carbon materials with various types from nano scale to micro-scale. As for variables sensitive to capacity, it was confirmed that the crystal sizes of the c-axis and the a-axis had a large influence. When analyzing the capacity with Hill equation, the intercalation of lithium ions determines the capacity through the edge of the base plane, and the intercalation of ions increases and decreases the interlayer distance of the graphene layer first and then returns to the original distance. Finally, an experimental prediction equation that can calculate capacity was proposed. Based on the results, a new structure as an anode material of a battery from the perspective of lithium-ion flow was proposed.

4.1 Introduction

Recently, as the commercialization and distribution of electric vehicles increase, the interest in lithium-ion batteries (LIBs) used as energy storage devise in various applications is also increasing [1-3]. This demand can greatly reduce the problem of environmental pollution caused by harmful gas emissions, so “carbon neutrality” can be realized. However, slower charging speed and shorter driving distance compared to conventional gasoline vehicles are becoming important problems in expanding electric vehicles [4]. To solve the problems, some research on electrodes to improve capacity related to charging rate are being conducted [1-8].

Carbon materials are mainly used as anode materials in lithium-ion batteries [6-8]. When the

energy of the battery is used, in other words, discharged, lithium-ions stored in the anode are released, and electrons move to the cathode through an external circuit. During charging, the opposite phenomenon occurs, and lithium-ions and electrons are stored in the anode. However, the fundamental question of how and where lithium-ions flow in carbon materials has been around since the beginning of development. This is because it is difficult to analyze the various types of carbon materials, various complicated and uncharacteristic structures, and both lithium and carbon are all light elements.

Usually, the capacity of LIB is known to be related to the crystallinity of carbon materials, but the relationship is not linear [9]. The previous research often explained that the increase in the interlayer distance between graphene layers in the structure of a carbon material facilitates the intercalation of lithium-ions. However, in real materials, the relationship is more complex, influenced by other structural variables. For this reason, the development of carbon materials to improve LIB performance currently relies on empirical guideline. This is in other words, a development that has complex carbon materials and relies heavily on experience and know-how.

Carbon elements usually exhibit two chemical bonding states. One example is a state in which carbon atoms are bonded in sp^2 hybrid orbit such as graphite, and other is bonded in sp^3 hybrid orbit such as diamond. And there is an amorphous structure in which sp^2 and sp^3 bonds are mixed. In this way, it is used as a single term “carbon material” as a single element according to the ratio of sp^2/sp^3 ratio but has various structures [10, 11].

It is difficult to find a combination or system of structural variables (descriptors in vector analysis) that can be explained in terms of these various structures as common variables. these variables lack a proper description of the capacity. Therefore, in practical cases, the correlation between capacity should be established in the analysis, and the physical meaning should also be linked.

The purpose of this chapter is to extract the descriptor, which is structural variable related to the capacity of LIB, and to interpret the behavior of lithium-ion.

Structural analysis of various carbon materials showed all variables that explained both the common and objective variables. In detail, a total of 21 carbon materials with various types were analyzed and characterized by X-ray diffraction (XRD), Raman spectroscopy, Brunauer-Emmett-Teller (BET) surface area analysis and scanning electron microscopy (SEM), and their numerical properties were extracted. Multivariate analysis was used to select descriptors that affect capacity. And the correlation between the behavior of lithium-ions and structural variables was discussed.

4.2 Experimental

4.2.1 Materials

Carbon nanotubes (CNT), carbon black (CB), including graphite (Gra) which is commonly used as an anode material of LIB, are largely classified into three types, and a total of 21 carbon samples are collected and presented in **Table 4.1**. Gra is assigned natural graphite, graphene nanoplatelet, expanded graphite, and graphite-based materials. The CNTs included single-walled carbon nanotubes (SWCNT) and multi-walled carbon nanotubes (MWCNT). Denka black, activated carbon, carbon black, mesoporous carbon, and needle coke powder were classified as CB.

4.2.2 Characterization of materials properties

The X-ray diffraction (XRD) of the carbon material sample was measured by Cu Kα radiation (diameter = 0.154 nm), 40 kV, and 200 mA, with measurement ranges of 5–40°, 20–100°, scan speed and scan steps of 10°/min and 0.01°, respectively, and an X-ray diffractometer (SmartLab, Rigaku Co., Japan) was used. Raman spectral microscopy (Raman, Leica DM 2500 M Ren (RL/TL), Renishaw Plc, England) obtained the surface structure formation of each carbon material in the wavelength range of 532.5 nm, 1000-3000 cm^{-1}. The field optical scanning electron microscope (FE-SEM, S-4800, Hitachi (Japan) observed the shape, size, and distribution at a 15 kV accelerated voltage with a probe current of 10 μA. The specific surface area was prepared using the Bru-nauer-Emmett-Teller (Belsorp-mini II; Belsorp, Japan) method and all samples were prepared by removing gas at 150 ℃ for 2 hours prior to BET measurement.

4.2.3 Cell fabrication and electrochemical testing

In the capacity battery test according to the C-rate, data were obtained with the battery charging/discharging unit 10V 5A System HJ Series (Hokuto Denko, Japan). A capacity test was

performed by assembling an NCM cathode containing a liquid electrolyte immersion polypropylene membrane and various carbon materials as an anode. The cathode was manufactured by mixing NCM532 powder: CB conductive material: PVDF binder, with a ratio of 90%, 5%, and 5%, respectively. The mixed solution was coated on the surface of the aluminum foil. As an anode material, the carbon material powder was mixed with a conductive material and a PVDF binder as ratio of 8:1:1 and coated on a copper foil. All electrodes were dried in a vacuum oven at 80 °C for 12 hours, and then 2032-coin cells were assembled inside an Argon-filled glove box with water and oxygen content at a dew point of -40 °C or less. The capacity measurements were performed at 25 ℃ with a potential range of 3 - 4.2 V at a 0.1 C current density. For each LIB coin cell, the experiment was repeated three times and the average data was used to obtain the capacity.

Table 4.1 Nomenclature and sample information of commercial carbon materials.

Sample #	Carbon type	Supplier	Product name
Gra1	Natural graphite	Meijo nanocarbon	SRP-7
Gra2	Natural graphite	Meijo nanocarbon	CP-2
Gra3	Graphene nanoplatelet	Sigma Aldrich	900409-250g
Gra4	Graphite	Alfa Aesar	T23E020
Gra5	Graphene nanoplatelet	Sigma Aldrich	900411-250g
Gra6	Natural graphite	Nanografi	NG08BE305
Gra7	Expanded graphite	Nanografi	NG04EO0723
CNT1	MWCNT	Meijo nanocarbon	Flotube 9000
CNT2	SWCNT	Meijo nanocarbon	eDIPs EC2.0
CNT3	SWCNT	Meijo nanocarbon	eDIPs EC2.0P
CNT4	SWCNT	Meijo nanocarbon	eDIPs EC1.5
CNT5	MWCNT	Meijo nanocarbon	NC7000
CNT6	MWCNT	Cnano	FT9100
CNT7	MWCNT	JEIO	Jenotube 6A
CB1	Denka black	Meijo nanocarbon	Li-100

CB2	Activated carbon	Meijo nanocarbon	AP11-0010
CB3	Carbon black	MTI	EQ-Lib-SuperP
CB4	Carbon black	MTI	EQ-Lib-SuperC45
CB5	Mesoporous carbon	Sigma Aldrich	699624-5g
CB6	Charcoal activated powder	Kanto chemical	01085-02
CB7	Needle cokes powder	SEC carbon	SCN-5

4.3 Results and Discussion

4.3.1 Data Extraction on Multiscale

Data such as XRD, Raman, SEM, BET, resistivity (electrical conductivity), and cycle tests for capacity through coin cells at 0.1 C-rate are attached to **Fig A 4.1 (a) to (g)**. All acquired XRD raw data were smoothed with an FFT filter method without background. Reflective wave separation was performed using a vogit function, where 002 reflection was separated using reflection by graphite (2θ = 26.2–26.8°) and reflection by amorphous carbon and CNT (2θ = 22–26°). The deconvolution data was defined as less developed crystalline carbon (LDCC) and more developed crystalline carbon (MDCC) regions [22, 23]. For SWCNTs, the facing surfaces between the bundles can contribute to the peak of the 22–26° position, which may refer to 002 reflection [24]. In general, Li+ is known to be stored in the space between different surfaces of graphite (0.335 nm), a distance corresponding to the (002) interplanar distance [25]. In the case of MWCNT, it can refer to graphene laminated in a multilayer structure on the SWCNT surface. The distance between multilayer structures was confirmed to be approximately 0.36 nm, as mentioned in [26], which is relatively close to the distance of graphite. From reflections according to **eq (4.1)** (Bragg equation) and **eq (4.2)** (Scherrer equation) [22, 23], the crystalline size along the c-axis, Lc was evaluated. The crystal size along the a-axis, called La, was evaluated as a 100 or 10I reflection that appeared between 30-50° according to **eq (2)**. The widened 10I peak appeared as a single peak because the separation of various structures in the carbon material was unclear. This may mean that each layer of carbon atoms in the structure is incompletely well laminated. Results obtained confirm that amorphous carbon is mainly composed of turbostratic structures [22, 23].

$$2d\sin\theta=n\lambda \quad \text{eq (4.1)}$$

$$L=K\lambda/\beta\cos\theta \quad \text{eq (4.2)}$$

In **eq (4.1)**, n is a positive integer, λ is a wavelength, K is a constant of 0.89 and 1.84 for Lc and La, respectively, λ is the wavelength of the X-ray target source (1.5406 Å, Cuα1) used, β is FWHM in radians, and Lc is calculated based on 002 peak, La is calculated on 10I peak [22, 23].

For Raman analysis, three representative bands of carbon materials, D, G, and 2D, were extracted and used. Raman raw data also smoothed and fitted using the vogit function to obtain peak position, intensity, and full width at half maximum (FWHM). The D band of carbon was attributed to the breathing mode of the six-membered ring near the edge of the planar structure, such as graphene, at about 1350 cm^{-1} [27-32]. The edges refer not only to the edges of the graphene structure, but also to the edges of the defects in the plane. The D band also reflects the graphene sheet size and the defects associated with these edges [27-32]. The G band of carbon has been shown to be about 1580 cm^{-1}, which is due to the vibration of carbon-carbon bonds connected by sp^2 bonds in the six-membered ring structure, which typically appears in all carbon materials [27-32]. The Raman 2D band, an overtone of the D band, was identified at 2660 to 2720 cm^{-1}, the breathing mode of the six-membered ring of carbon [27-32]. For symmetrical six-circle rings, the vibration is further increased due to increased external constraints, so the strength of the 2D band increases as the six-circle rings spread. On the other hand, as the number of graphene layers increases, charge screening occurs, resulting in a decrease in strength, while FWHM increases [27-32].

For micro scale analysis, the particle size was confirmed by SEM. A minimum of 20 lengths were measured for each sample. The aspect ratio was measured as a ratio of width (short) to height (long). After assigning aspect ratio percentiles at 10%, 50%, and 90% to D10, D50, and D90, D90/D10 was obtained as shown in **Fig A 4.1 (d)**.

The specific surface area was calculated by the BET method in the linear range of P/P0 = 0.05–0.35 on the isotherm curve as the following **eq (4.3)** [33, 34].

$$(P/P0)/(V\times(1-P/P0)) = 1/(Vm\times C)+(C-1)/C\times(P/P0)/Vm \quad \text{eq. (4.3)}$$

where V refers to the amount of gas adsorbed, P is the pressure, are both measured, P0 is the vapor pressure of the adsorbate, Vm is the monolayer coverage, and Cs are fitting parameters [33, 34]. From plotting the adsorption data based on the linear BET equation (**Fig A 4.1 (e)**), Vm and C could

be determined by simultaneously solving the expression for the slope of the line [33, 34].

4.3.2 Descriptor Vector for Multivariate Analysis

As a result of the analysis, descriptors were got and construct to a dataset, which is shown in Table 4.2. To find descriptors what primarily affect battery characteristics, the priorities of all extracted factors must be defined. However, it was difficult to proceed because several descriptors interacted with each other. For example, descriptors associated with crystallinity have been shown to be inversely proportional to those associated with defects. On the other hand, for three-dimensional materials, lateral growth is reported to affect vertical growth [12, 13].

Table 4.2 Analysis results of the samples**.**

Aspect ratio	D10 (µm)	D50 (µm)	D90 (µm)	D90/D10
2.06	7.00	11.50	16.00	2.29
1.92	1.44	3.50	11.00	7.62
1.67	2.50	9.62	20.00	8.00
1.75	8.33	15.00	22.50	2.70
2.20	2.50	12.50	50.00	20.00
2.04	3.33	15.00	45.00	13.50
1.75	4.00	20.00	36.00	9.00
1.39	10.00	35.00	53.33	5.33
153.82	0.56	5.00	16.50	29.70
153.02	0.84	4.18	21.15	25.31
231.82	1.80	9.00	15.30	8.50
1.79	10.63	53.12	157.50	14.82
1.69	0.63	4.50	20.00	32.00
11.97	3.33	22.50	60.00	18.00
1.74	1.67	4.50	9.67	5.80
1.46	7.50	11.00	15.00	2.00
1.78	0.25	1.67	7.00	28.00
1.71	0.45	2.27	12.50	27.50
1.50	1.17	3.30	6.17	5.29
1.83	1.82	9.09	45.00	24.75
1.86	3.00	5.00	9.67	3.22

d002 (nm)	Lc (nm)	La (nm)	ID/IG	FWHMG (cm^{-1})	FWHM2D (cm^{-1})	I2D/IG
0.3361	28.74	53.17	0.0928	22.63	79.93	0.3872
0.3361	17.53	47.63	0.3745	35.90	72.74	0.6890
0.3357	22.27	13.62	0.0139	21.28	68.88	0.2592
0.3362	32.35	55.28	0.1389	22.35	75.61	0.4637
0.3362	16.31	13.05	0.1747	23.12	77.38	0.3220
0.3354	20.75	11.06	0.0435	23.17	75.91	0.3742
0.3357	23.66	14.82	0.1401	24.60	78.19	0.4398
0.3433	4.21	6.50	0.9657	81.88	114.71	0.5295
0.3954	4.83	4.48	0.0190	32.75	50.38	0.2313
0.3556	4.20	5.08	0.0140	27.35	47.78	0.2139
0.3870	2.53	4.33	0.0104	26.30	73.22	0.1555
0.3454	2.67	6.52	1.3358	82.12	114.73	0.3886
0.3440	3.39	7.23	0.0592	21.61	71.14	0.5179
0.3481	1.78	4.92	1.3932	93.53	172.42	0.1629
0.3492	3.42	7.49	0.9281	101.46	127.69	0.5282
0.3723	3.16	3.68	0.9800	80.61	290.65	0.0887
0.3531	2.47	4.78	1.1733	115.17	221.14	0.1397
0.3529	2.55	4.49	1.1699	113.60	326.58	0.1228
0.3447	5.41	7.67	0.5453	50.70	82.41	0.8849
0.3559	4.12	4.29	1.2506	74.01	310.59	0.1150
0.3444	3.94	6.43	0.9204	94.57	207.03	0.1510

Electrical resistivity (ohm·cm)	Electrical conductivity (S/cm)	Specific surface area (m^2/g)
0.1668	5.9959	11.959
0.6152	1.6254	23.083
0.1858	5.3827	34.912
2.9920	0.3342	7.155
0.2951	3.3891	64.586
0.3524	2.8374	158.020
0.1434	6.9754	22.965
0.2648	3.7767	236.610
0.1580	6.3299	446.950
0.0181	55.2486	1556.300
0.0636	15.7356	366.720
0.2444	4.0922	234.730
1.4492	0.6901	210.340
3.5410	0.2824	496.730
1.3073	0.7650	66.195
16.5964	0.0603	1702.300
0.6727	1.4865	63.916
0.7834	1.2765	27.990
1.8729	0.5339	82.932
6.0841	0.1644	1352.500
22.2864	0.0449	16.193

Sample #	Capacity at 0.1 C-rate (mAh/g)
GRA1	263.01
GRA2	335.51
GRA3	284.93
GRA4	294.69
GRA5	330.35
GRA6	258.72
GRA7	312.53
CNT1	124.61
CNT2	37.02
CNT3	32.58
CNT4	42.51
CNT5	107.03
CNT6	173.57
CNT7	50.12
CB1	116.05
CB2	18.45
CB3	191.00
CB4	198.92
CB5	184.73
CB6	59.47
CB7	200.60

4.3.3 Select Descriptor and verified by statistical method.

A total of 12 correlations were analyzed for capacity, and **Fig 4.1** show the relationship with the descriptor candidate group, each with a high correlation coefficient (adj-R^2). It may be seen that Lc and La showed high correlation within capacity (**Fig 4.1 (a) and (b)**).

The selected descriptor has been validated by the statistical method, p-value (**Table 4.3**) [14, 15]. The p-value is usually assumed to be an unrelated null hypothesis. For the current significance level, p-value 0.05 is commonly used, which means that it is associated with a 5% probability [14, 15]. If the p-value is less than or equal to 0.05, the null hypothesis may be incorrect, indicating that it is correlated [14, 15]. This means that the lower the p-value, the greater the correlation between each other [14, 15]. In this study, when identifying capacities, and analyzed descriptors, the capacities were found to have the lowest p-value of Lc among technicians at 0.1 C-rate discussed earlier.

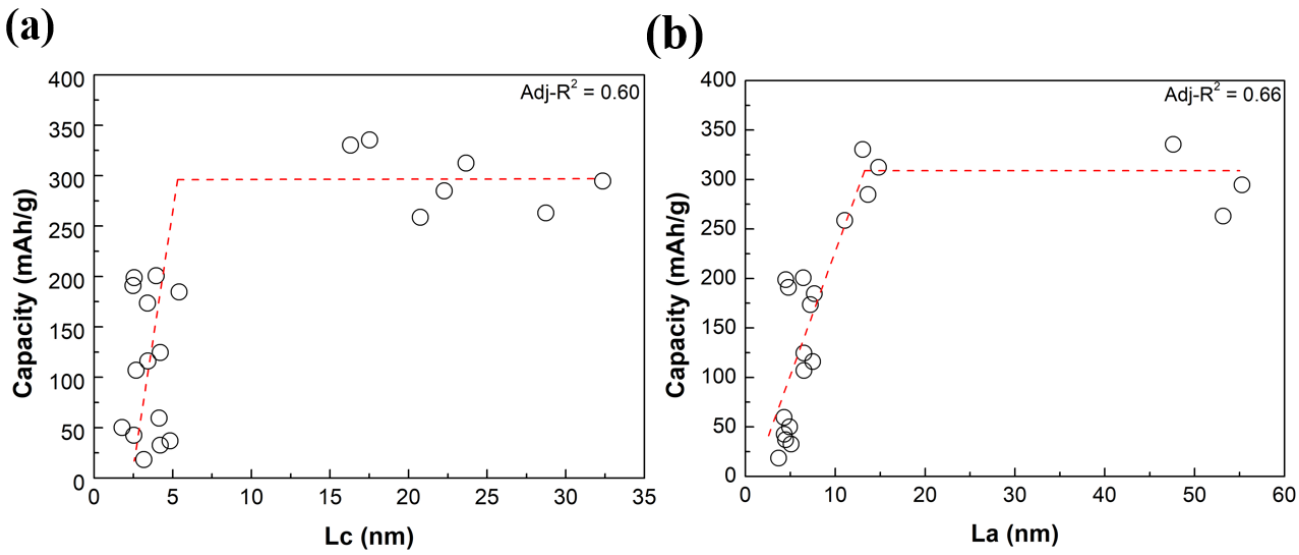

Fig 4.1 Selected descriptors, (a) L_c and (b) L_a, having good correlations with capacity.

Table 4.3 P-value table of all parameters

P-value	A	B	C	D	E	F	G	H	I	J	K	L	M	N	O	P
A	<0.0001	0.3807	0.1782	0.0004	0.0003	<0.0001	0.0029	0.0941	0.0971	0.1799	0.0555	0.0165	0.9602	0.7013	0.5783	0.2566
B	0.3807	<0.0001	0.3222	0.1650	0.7565	0.3723	0.4791	0.1257	0.1049	0.0147	0.1166	0.3929	0.5858	0.5462	0.4540	0.1599
C	0.1782	0.3222	<0.0001	0.0331	0.3250	0.5313	0.6047	0.0947	0.1673	0.1328	0.4535	0.0019	0.4520	0.6600	0.8273	0.3576
D	0.0004	0.1650	0.0331	<0.0001	0.3151	0.0603	0.1197	0.4884	0.7709	0.1216	0.0395	0.1826	0.9455	0.8174	0.9178	0.4133
E	0.0003	0.7565	0.3250	0.3151	<0.0001	0.0002	0.0151	0.5147	0.2286	0.4668	0.0699	<0.0001	0.0788	0.3876	0.6144	0.0455
F	<0.0001	0.3723	0.5313	0.0603	0.0002	<0.0001	<0.0001	0.0110	0.0039	0.0605	0.1844	0.1461	0.1857	0.8602	0.7004	0.0333
G	0.0029	0.4791	0.6047	0.1197	0.0151	<0.0001	<0.0001	0.0926	0.0455	0.1249	0.0840	0.3186	0.1843	0.8675	0.5017	0.0456
H	0.0941	0.1257	0.0947	0.4884	0.5147	0.0110	0.0926	<0.0001	<0.0001	<0.0001	0.2691	0.0645	0.3875	0.1735	0.1182	0.7833
I	0.0971	0.1049	0.1673	0.7709	0.2286	0.0039	0.0455	<0.0001	<0.0001	<0.0001	0.1813	0.1706	0.8925	0.6945	0.6480	0.6985
J	0.1799	0.0147	0.1328	0.1216	0.4668	0.0605	0.1249	<0.0001	<0.0001	<0.0001	0.0098	0.1505	0.8807	0.6243	0.8382	0.5040
K	0.0555	0.1166	0.4535	0.0395	0.0699	0.1844	0.0840	0.2691	0.1813	0.0098	<0.0001	0.1970	0.6537	0.7296	0.9506	0.1269
L	0.0165	0.3929	0.0019	0.1826	<0.0001	0.1461	0.3186	0.0645	0.1706	0.1505	0.1970	<0.0001	0.2018	0.4236	0.4892	0.3474
M	0.9602	0.5858	0.4520	0.9455	0.0788	0.1857	0.1843	0.3875	0.8925	0.8807	0.6537	0.2018	<0.0001	<0.0001	0.0054	0.0098
N	0.7013	0.5462	0.6600	0.8174	0.3876	0.8602	0.8674	0.1735	0.6945	0.6243	0.7296	0.4236	<0.0001	<0.0001	<0.0001	0.3736
O	0.5783	0.4540	0.8273	0.9178	0.6144	0.7004	0.5017	0.1182	0.6480	0.8382	0.9506	0.4892	0.0054	<0.0001	<0.0001	0.7539
P	0.2566	0.1599	0.3576	0.4133	0.0455	0.0333	0.0456	0.7833	0.6985	0.5040	0.1269	0.3474	0.0098	0.3736	0.7539	<0.0001

A: Discharge capacity at 0.1C-rate (mAh/g)

B: Electrical resistivity (ohm·cm)

C: Electrical conductivity (S/cm)

D: Specific Surface Area (m^2/g)

E: d002 (nm)

F: Lc (nm)

G: La (nm)

H: ID/IG

I: FWHMG (cm^{-1})

J: FWHM2D (cm^{-1})

K: I2D/IG

L: Aspect ratio

M: D10 (μm)

N: D50 (μm)

O: D90 (μm)

P: D90/D10

4.3.4 Results of applying Hill equation

The candidate groups showing high correlation showed similar values and trends in capacity. As mentioned above, since it is affected by the interaction of factors, it needs a method of distinguishing effective factors and has statistical and physical meaning. In **Fig 4.2 (a) and (b)**, as Lc and La increase, the capacity increases and then shows a similar tendency to saturate. This is like the appearance of the Hill equation (**eq (4.4)**) used in pharmacology, which shows the binding of ligands to macromolecules. The Hill equation is a quantitative receptor model between reactants (A) and receptors (B) first presented in 1910 [16, 17].

$$Y=V\times Xn/(Kn+Xn) \qquad \text{eq (4.4)}$$

V is defined as the maximum adsorption of receptor B, K is the dissociation constant, X is the concentration of free (non-bonding) ligands, and n is the Hill coefficient [16, 17]. The ratio between the adsorption rate coefficient and the desorption rate coefficient may be expressed as a dissociation constant K when equilibrium is reached at a certain temperature [16, 17]. In the case of $n>1$, adsorption of adsorbent B is further promoted even when adsorbent B is adsorbed. Conversely, when the adsorbent B is adsorbed at $n<1$, the adsorption of the additional adsorbent B decreases [16, 17]. When explain lithium-ion intercalation in structure of carbon material applied by this model, the variables from eq (4) were considered based on the same physical meaning related to LIB. The number of lithium-ions intercalated is V, the percentage of regions in which lithium-ions are not intercalated is X, and the reaction order is n. However, here, it was used as the plane area (assumed as a rectangle) of the crystallite parallel to the a-axis and c-axis, not the surface area fraction. The graph that applied this as the correlation between Lc^2 and La^2 to the capacity of LIB is shown in **Fig 4.2 (a) and (b)**, and **Table 4.4** shows the results of each suitable variables.

Looking at the results of the capacity applied with Hill equation, the crystallinity of c-axis determines the capacity determines the capacity. Lc, which is perpendicular to the basic plane, has a small intercalation of lithium-ion, but La, which is parallel to the basic plane, has a strong correlation. This is very close to the theoretical capacity of carbon materials in the LIB [8, 18]. In this study, it is assumed that the intercalation of lithium-ion from the basic plane is small enough from the edge of the basic plane compared to the intercalation, as shown in (100) plane. In other words, we can see that intercalation of lithium-ion occurs only on edge facets. The physical means obtained from Hill equation are described in **Fig 4.3**.

In the case of Lc^2, the amount of lithium-ion intercalation was higher than that of La^2, but the difference was not relatively large. Originally, the amount lithium-ion intercalation, whether Lc^2 or La^2, should be the same. For K values, Lc^2 was about 1.5 times larger than La^2, indicating that the effective factor for capacity is Lc^2 and that lithium-ion intercalation is a rate limiting step in terms of the dynamics of intercalation in the edge facet by Lc. The movement of lithium-ion between graphene layers is faster than that of the edge facet. For La^2, n is greater than 1, indicating that the intercalated lithium-ion first between layers influenced the movement of the intercalated lithium-ion next. This is more like Rudorff theory among the phenomena presented as a storage method of lithium-ion [19, 20]. Lc^2 shows that n is less than 1, but the first intercalated lithium-ion inhibits the next intercalation. However, if the constant n is metastable, we can see that the surface spacing at the edge decreases again if the lithium-ion penetrates far enough from the edge or interface. For more information, it is necessary to measure the intercalation of lithium-ion near the carbon edge, but it is an important phenomenon related to the active energy required for intercalation in the carbon material.

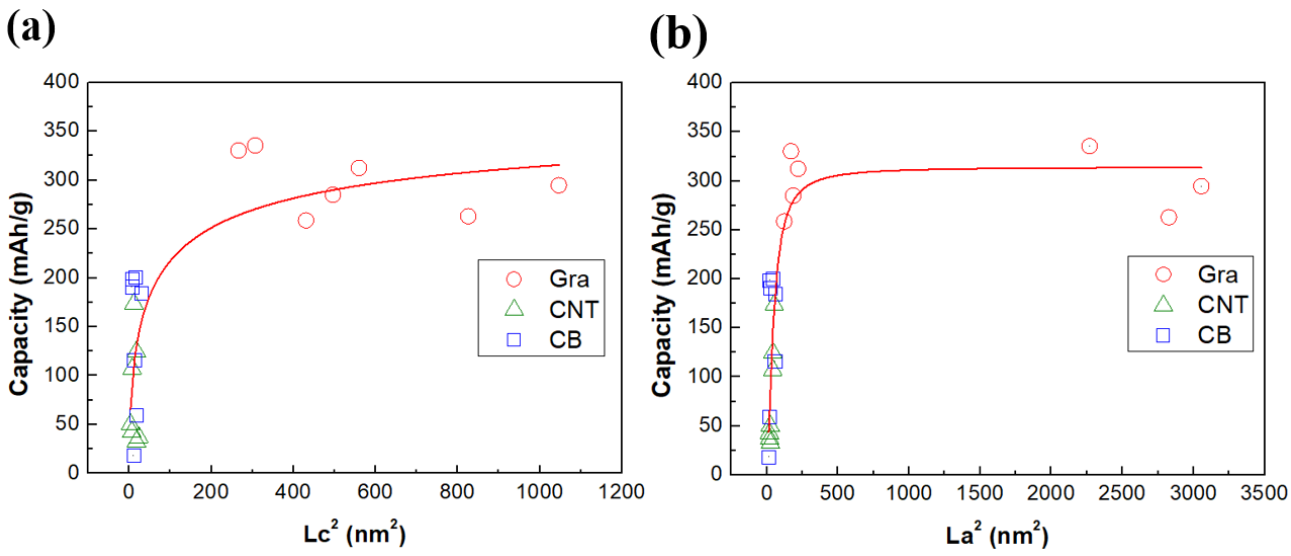

Fig 4.2 Correlations of (a) L_c and (b) L_a to the capacity applied Hill's equation.

Table 4.4 Comparison of variables in Hill's equation for the capacity of LIB calculated by using L_c^2 and L_a^2

Variables	L_c^2	L_a^2
V	385	314
K	61.4	45.8
n	0.53	1.50

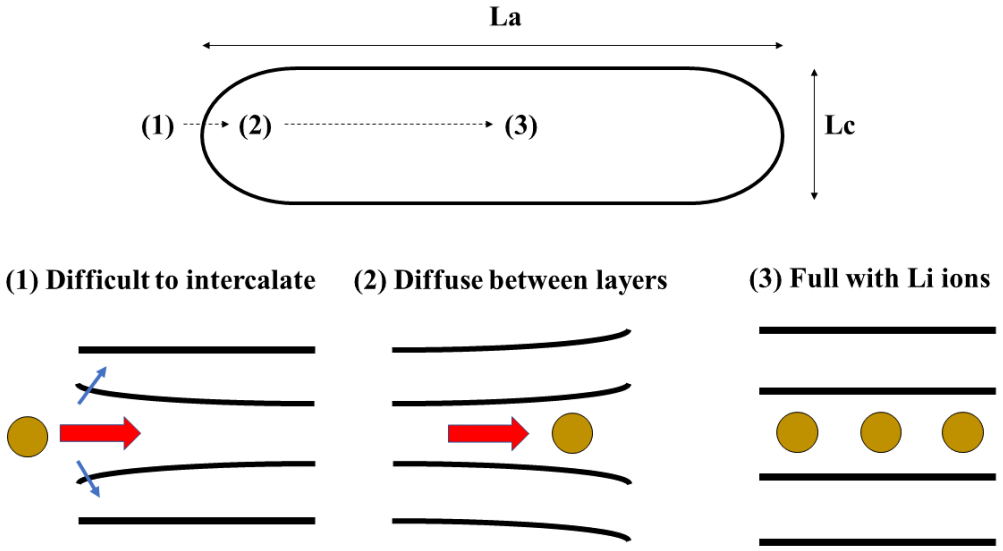

Fig 4.3 Intercalation and diffusion of lithium-ion according to stacking and planar direction areas by Hill's equation analysis.

4.3.5 Predict equation of capacity.

The most significant impact on capacity was Lc. We propose a prediction equation for capacity in guaranteed range together with two ideal assumptions. First, it was a single-layer graphene. It has Lc with a interlayer distance of 0.335 nm [21, 22], FWHM2D of 20 cm-1 [23-26], specific capacity of 1 mAh/g. Second, the other was ideal graphite. It was assumed to has a large Lc with a interlayer distance of 1000 nm [27, 28], FWHM2D of 20 cm-1, specific capacity of 372 mAh/g (theoretical value) [8, 18]. The prediction model of capacity using Lc is presented in **Fig 4.4 (a)** and the equation is presented in **Eq (4.5)** with the guaranteed range.

Specific capacity = $374 \times (Lc2)^{0.55} / (53.9^{0.55} + (Lc\ ^{2})^{0.55})$ Eq. (4.5)

To verify that the suggested equation is valid, data were extracted from 15 reference samples from previous studies and compared [9, 29-33]. The correlation between Lc and capacity of the suggested function was 0.72 for adj-R^2, and 0.69 for the addition of reference samples, which slightly decreased, but it can be confirmed that it is valid by showing similar values (**Fig 4.4 (b)**).

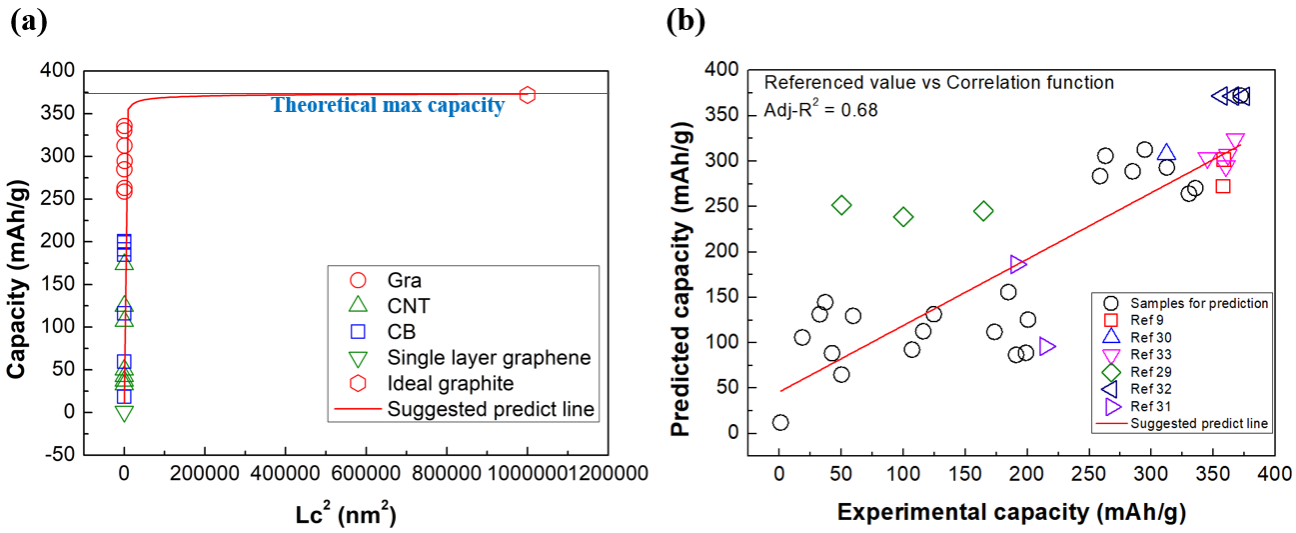

Fig 4.4 (a) Correlations of L_c to the specific capacity within the guaranteed values (b) the validation of the prediction results by using data of reference samples obtained from other previous works.

4.3.6 Candidate structure of carbon materials

Summarizing the contents so far, the phenomenon of lithium-ion paths in carbon materials is presented (**Fig 4.5 (a)**). Lithium-ion conduction is mainly related to insertion at the edge of graphene. lithium-ion intercalation from the edge to the surface was expected to have the greatest active energy. Therefore, two possible improvements could be proposed from a structural perspective to secure the lithium-ion transfer path. One is to expose more surfaces consisting of graphene edges on the surface of carbon material particles. Finally, it was to provide a junction between edges inside the particle. **Fig 4.5 (b)** shows the relationship with Lc, La, and capacity to understand and propose the structure of suitable carbon based on lithium-ion and electron transport pathways. Lc/La = 1/3, Lc/La = 1, and

Lc/La = 2. For Lc/La = 1/3, the structure represents a thermodynamically stable part in the form of a macro scale. As the ratio increases to 2, the structure becomes more unstable, and from a historical experimental data and empirical point of view, the structure becomes unstable, making it difficult to use it practically. According to the above discussion, crystals with Lc around 40 nm and La around 30 nm should meet two possible improvements. Moreover, by creating crystals of not too large size, we can partially free ourselves from the spell of shape domination by free energy.

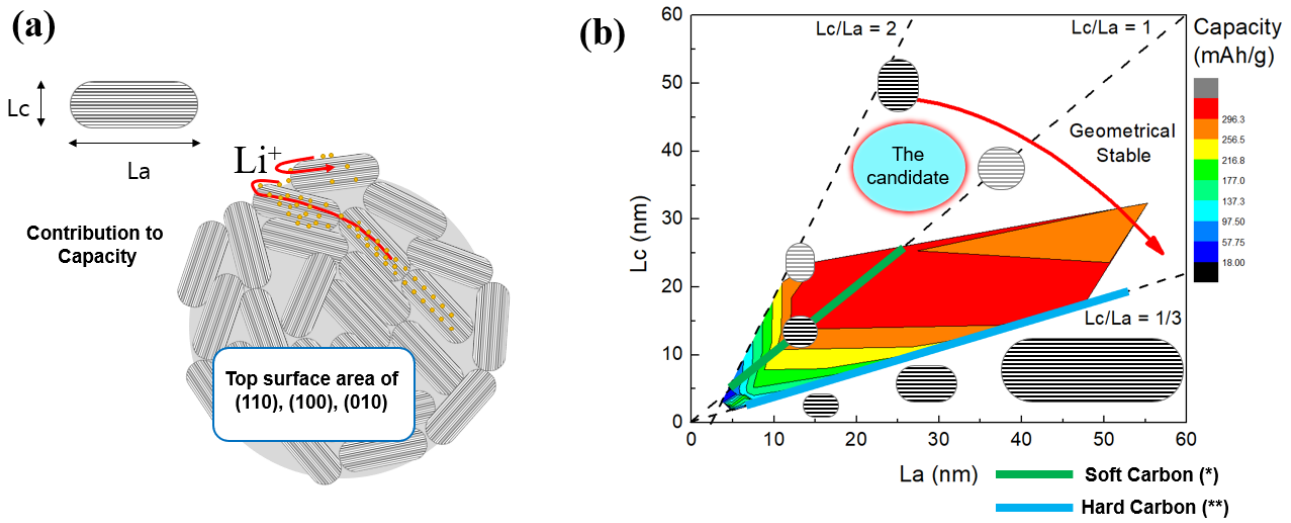

Fig 4.5 (a) Effective descriptors and their phenomenon on capacity and electrical conductivity; (b) capacity and structural factors changes as function of L_c and L_a. (*[1] , **[2, 3])

4.4 Conclusion

This research analyzed a total of 21 carbon materials, including graphite, graphene, SWCNT, MWCNT, and carbon black, from nano to microscale and extracted 15 structural factors from each sample. The correlation coefficients of all descriptions were investigated to find variables that greatly affect capacity, and two variables with high correlation coefficients, Lc and La, were selected. And the selected descriptors could also be seen as a reasonable result by statistical method. In addition, Lc and La have a similar relationship with capacity, and the Hill equation was applied to examine the flux effect of lithium ions depending on the area of crystal direction of the carbon material. The Hill

equation shows that lithium-ions are preferentially intercalated from the edge of the basal plane, allowing the total amount of lithium ions to be determined. We also show that the intercalation of lithium ions extends the interlayer distance of the edge face once, and that the interlayer distance of the edge face returns to its original interval after the lithium-ion moves inwards enough from the edge. Also, using the selected descriptor, Lc, an equation that can predict the capacity of lithium-ion battery with the guaranteed range is presented. Based on the results from the perspective of lithium-ion flow, we would like to propose a new carbon material structure as a battery anode. It may be seen that the next generation carbon material for LIB must have Lc/La of 1 or more to smoothly intercalate lithium-ions, and crystals having Lc of 40 nm and La of 30 nm are the structures that the next generation battery should have.

4.5 References of chapter 4

[1] Liu, W., T. Placke, and K. Chau, Overview of batteries and battery management for electric vehicles. Energy Reports, 2022. 8: p. 4058-4084.

[2] S. Rangarajan, S., et al., Lithium-ion batteries—The crux of electric vehicles with opportunities and challenges. Clean Technologies, 2022. 4(4): p. 908-930.

[3] Asef, P., et al., Future Trends and Aging Analysis of Battery Energy Storage Systems for Electric Vehicles. Sustainability, 2021. 13(24): p. 13779.

[4] Marom, R., et al., A review of advanced and practical lithium battery materials. Journal of Materials Chemistry, 2011. 21(27): p. 9938-9954.

[5] Tian, R., et al., Quantifying the effect of electronic conductivity on the rate performance of nanocomposite battery electrodes. ACS Applied Energy Materials, 2020. 3(3): p. 2966-2974.

[6] Ogihara, N. and Y. Itou, Impedance Analysis Using Symmetric Cells for Understanding Electrochemical Behaviour of Porous Electrodes for Lithium-ion Batteries. R&D Rev. Toyota CRDL, 2017. 48: p. 17-24.

[7] Han, H., et al., Microstructure control of the graphite anode with a high density for Li ion batteries with high energy density. Electrochimica acta, 2015. 166: p. 367-371.

[8] Agubra, V. and J. Fergus, Lithium ion battery anode aging mechanisms. Materials, 2013. 6(4): p. 1310-1325.

[9] Hoshi, K., et al., Production and advantages of carbon-coated graphite for the anode of lithium ion rechargeable batteries. Tanso, 2009. 2009(240): p. 213-220.

[10] Robertson, J., Diamond-like amorphous carbon. Materials science and engineering: R: Reports, 2002. 37(4-6): p. 129-281.

[11] Robertson, J., π-bonded clusters in amorphous carbon materials. Philosophical magazine B, 1992. 66(2): p. 199-209.

[12] González, D., et al., Structural characterization of graphite materials prepared from anthracites of different characteristics: a comparative analysis. Energy & fuels, 2004. 18(2): p. 365-370.

[13] Kubota, K., et al., Structural analysis of sucrose-derived hard carbon and correlation with the electrochemical properties for lithium, sodium, and potassium insertion. Chemistry of Materials, 2020. 32(7): p. 2961-2977.

[14] Hung, H.J., et al., The behavior of the p-value when the alternative hypothesis is true. Biometrics, 1997: p. 11-22.

[15] Panagiotakos, D.B., The value of p-value in biomedical research. The open cardiovascular medicine journal, 2008. 2: p. 97.

[16] Gesztelyi, R., et al., The Hill equation and the origin of quantitative pharmacology. Archive for history of exact sciences, 2012. 66(4): p. 427-438.

[17] Goutelle, S., et al., The Hill equation: a review of its capabilities in pharmacological modelling. Fundamental & clinical pharmacology, 2008. 22(6): p. 633-648.

[18] Igarashi, D., et al., Effect of Crystallinity of Synthetic Graphite on Electrochemical Potassium Intercalation into Graphite. Electrochemistry, 2021: p. 21-00062.

[19] Asenbauer, J., et al., The success story of graphite as a lithium-ion anode material–fundamentals, remaining challenges, and recent developments including silicon (oxide) composites. Sustainable Energy & Fuels, 2020. 4(11): p. 5387-5416.

[20] Wang, G., M. Yu, and X. Feng, Carbon materials for ion-intercalation involved rechargeable

battery technologies. Chemical Society Reviews, 2021. 50(4): p. 2388-2443.

[21] Cellini, F., et al., Layer dependence of graphene-diamene phase transition in epitaxial and exfoliated few-layer graphene using machine learning. 2D Materials, 2019. 6(3): p. 035043.

[22] Li, Q., et al., Substrate effect on thickness-dependent friction on graphene. physica status solidi (b), 2010. 247(11-12): p. 2909-2914.

[23] Pezzini, S., et al., High-quality electrical transport using scalable CVD graphene. 2D Materials, 2020. 7(4): p. 041003.

[24] Tao, L., et al., Uniform wafer-scale chemical vapor deposition of graphene on evaporated Cu (111) film with quality comparable to exfoliated monolayer. The Journal of Physical Chemistry C, 2012. 116(45): p. 24068-24074.

[25] De Fazio, D., et al., High-mobility, wet-transferred graphene grown by chemical vapor deposition. ACS nano, 2019. 13(8): p. 8926-8935.

[26] Moldt, T., et al., High-yield production and transfer of graphene flakes obtained by anodic bonding. Acs Nano, 2011. 5(10): p. 7700-7706.

[27] SATO, H., et al., Raman spectra and rate capability of graphite anode for lithium ion battery. Denki Kagaku oyobi Kogyo Butsuri Kagaku, 1998. 66(12): p. 1253-1259.

[28] Bar-Tow, D., E. Peled, and L. Burstein, A study of highly oriented pyrolytic graphite as a model for the graphite anode in Li-Ion batteries. Journal of the Electrochemical Society, 1999. 146(3): p. 824.

[29] Canal-Rodríguez, M., et al., Graphitized carbon xerogels for lithium-ion batteries. Materials, 2019. 13(1): p. 119.

[30] Hwang, J.U., et al., Characteristics of an artificial graphite anode material for rapid charging: manufactured with different coke particle sizes. Journal of Materials Science: Materials in Electronics, 2022. 33(25): p. 20095-20105.

[31] Im, U.-S., et al., The effect of mild activation on the electrochemical performance of pitch-coated graphite for the lithium-ion battery anode material. Materials Letters, 2020. 278: p. 128421.

[32] Ge, C., et al., Novel hard carbon/graphite composites synthesized by a facile in situ anchoring method as high-performance anodes for lithium-ion batteries. RSC advances, 2018. 8(60): p. 34682-

34689.

[33] Lee, S.E., et al., Effect of crystallinity and particle size on coke-based anode for lithium ion batteries. Carbon letters, 2021. 31(5): p. 911-920.

[34] Ou, M., et al., Local structures of soft carbon and electrochemical performance of potassium-ion batteries. ACS Applied Materials & Interfaces, 2021. 13(24): p. 28261-28269.

[35] Yamamoto, T., et al., Structural and Electrochemical Properties of Hard Carbon Negative Electrodes for Sodium Secondary Batteries Using the Na [FSA]–[C3C1pyrr][FSA] Ionic Liquid Electrolyte. Electrochemistry, 2017. 85(7): p. 391-396.

[36] Larbi, L., et al., Impact of Hard Carbon Properties on Their Performance in Potassium-Ion Batteries. ACS Applied Energy Materials, 2023. 6(10): p. 5274-5289.

4.6 Appendix of Chapter 4

Figure A 4.1 Fitting results of each analysis method

(a) XRD 5-40

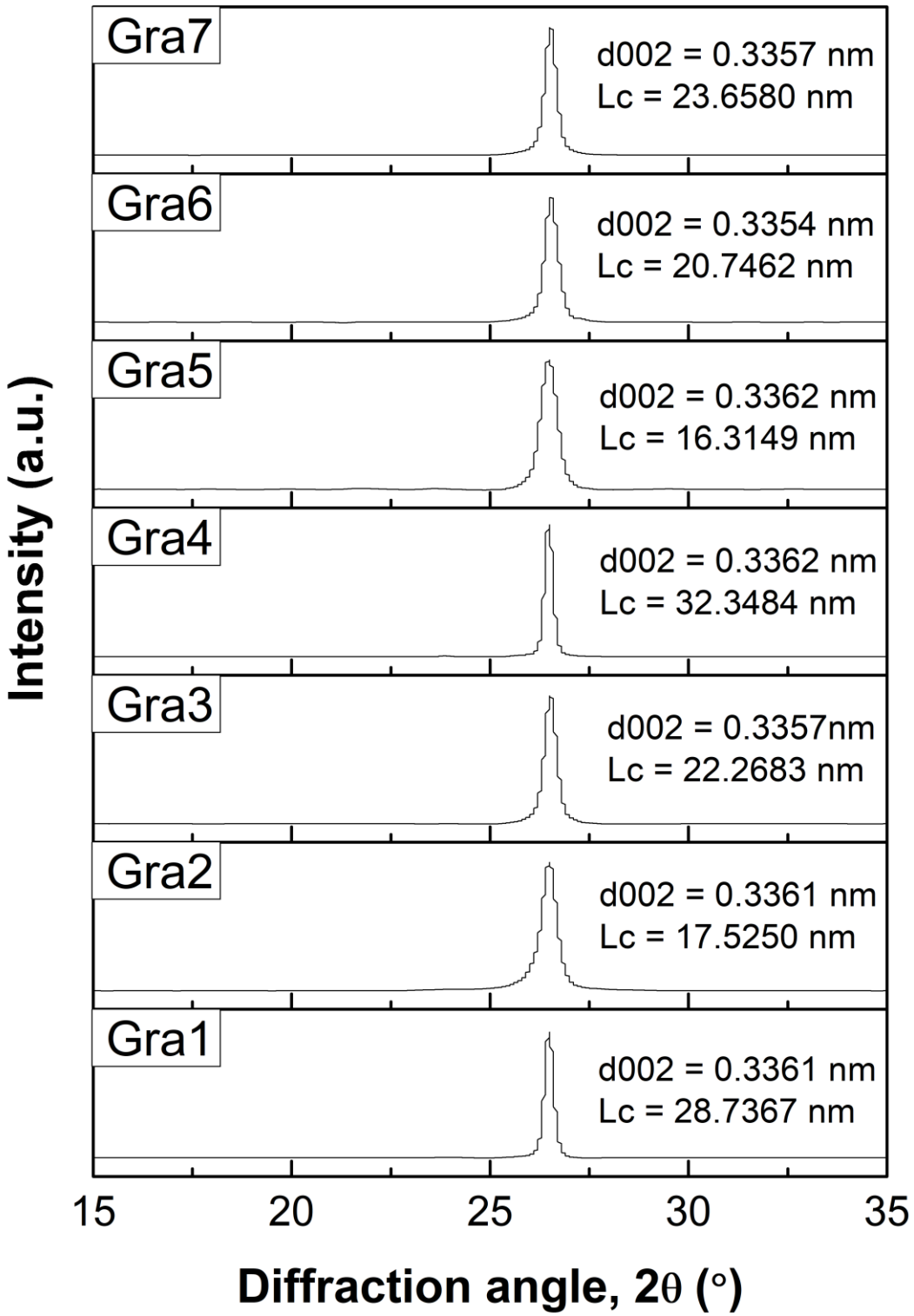
Gra7
d002 = 0.3357 nm
Lc = 23.6580 nm
Gra6
d002 = 0.3354 nm
Lc = 20.7462 nm
Gra5
d002 = 0.3362 nm
Lc = 16.3149 nm
Gra4
d002 = 0.3362 nm
Lc = 32.3484 nm
Gra3
d002 = 0.3357nm
Lc = 22.2683 nm
Gra2
d002 = 0.3361 nm
Lc = 17.5250 nm
Gra1
d002 = 0.3361 nm
Lc = 28.7367 nm
Intensity (a.u.)
15
20
25
30
35
Diffraction angle, 2θ (°)

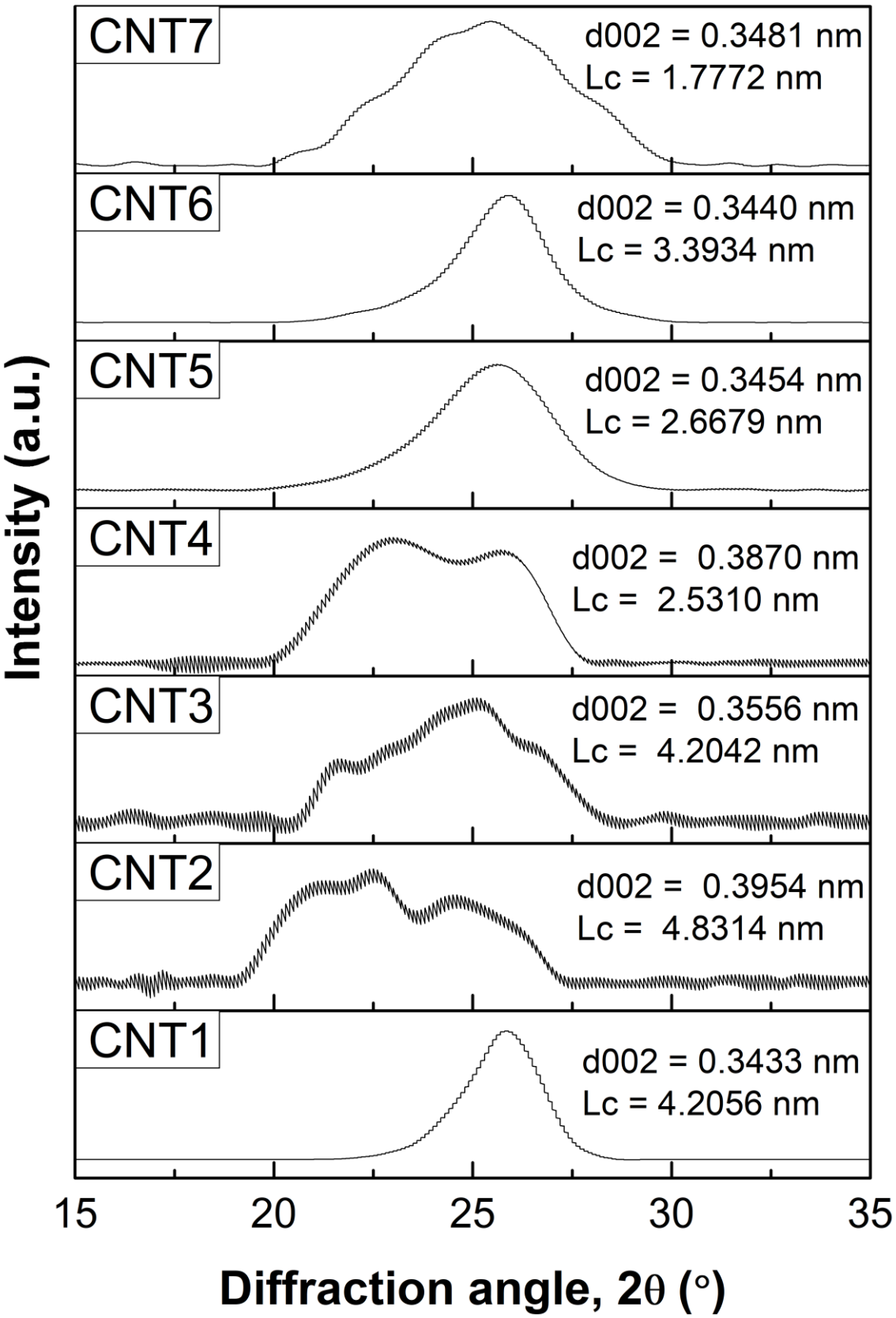
CNT7
d002 = 0.3481 nm
Lc = 1.7772 nm
CNT6
d002 = 0.3440 nm
Lc = 3.3934 nm
CNT5
d002 = 0.3454 nm
Lc = 2.6679 nm
CNT4
d002 = 0.3870 nm
Lc = 2.5310 nm
CNT3
d002 = 0.3556 nm
Lc = 4.2042 nm
CNT2
d002 = 0.3954 nm
Lc = 4.8314 nm
CNT1
d002 = 0.3433 nm
Lc = 4.2056 nm
Intensity (a.u.)
15
20
25
30
35
Diffraction angle, 2θ (°)

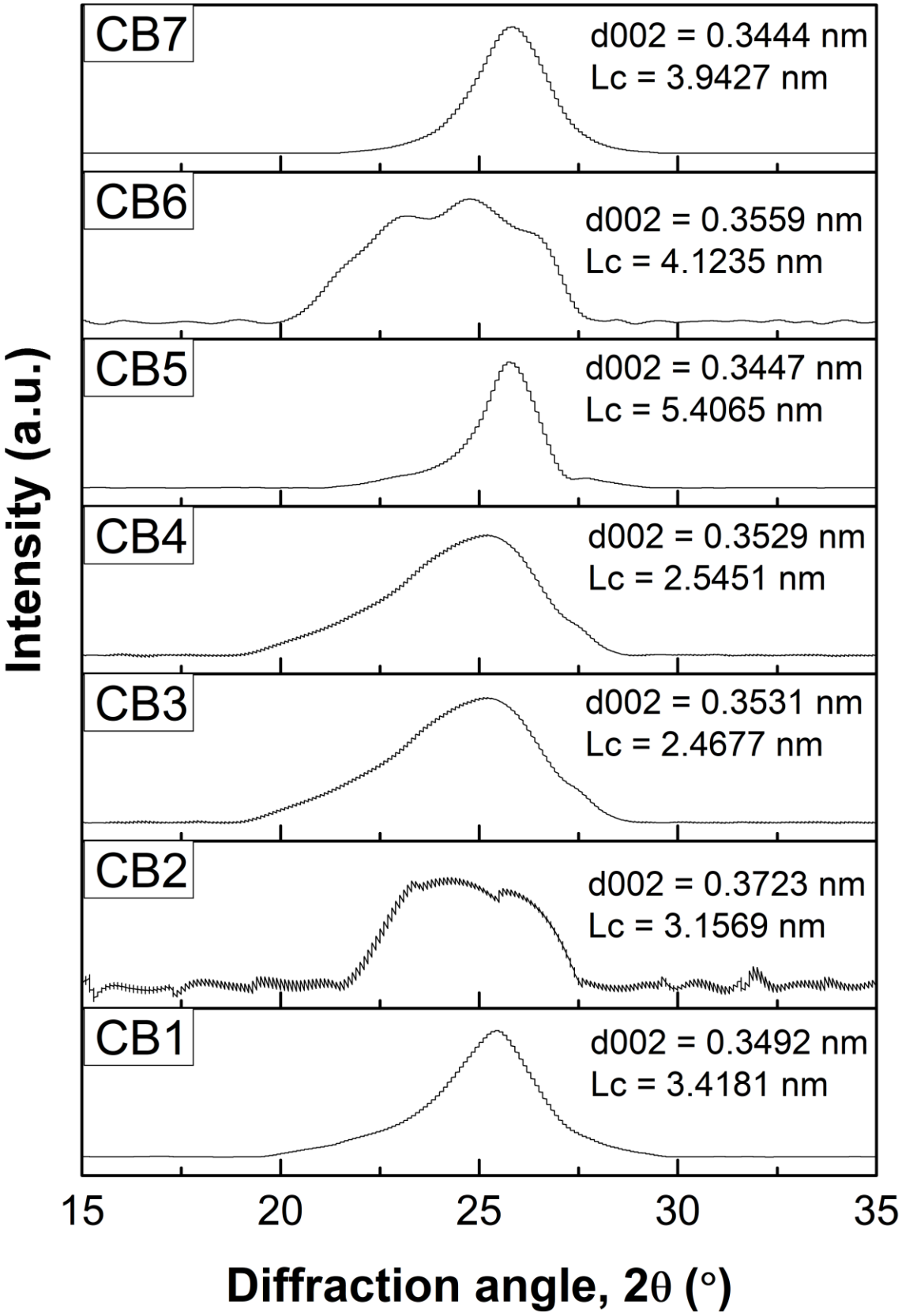
CB7
d002 = 0.3444 nm
Lc = 3.9427 nm
CB6
d002 = 0.3559 nm
Lc = 4.1235 nm
CB5
d002 = 0.3447 nm
Lc = 5.4065 nm
CB4
d002 = 0.3529 nm
Lc = 2.5451 nm
CB3
d002 = 0.3531 nm
Lc = 2.4677 nm
CB2
d002 = 0.3723 nm
Lc = 3.1569 nm
CB1
d002 = 0.3492 nm
Lc = 3.4181 nm
Intensity (a.u.)
15
20
25
30
35
Diffraction angle, 2θ (°)

(b) XRD 30-50

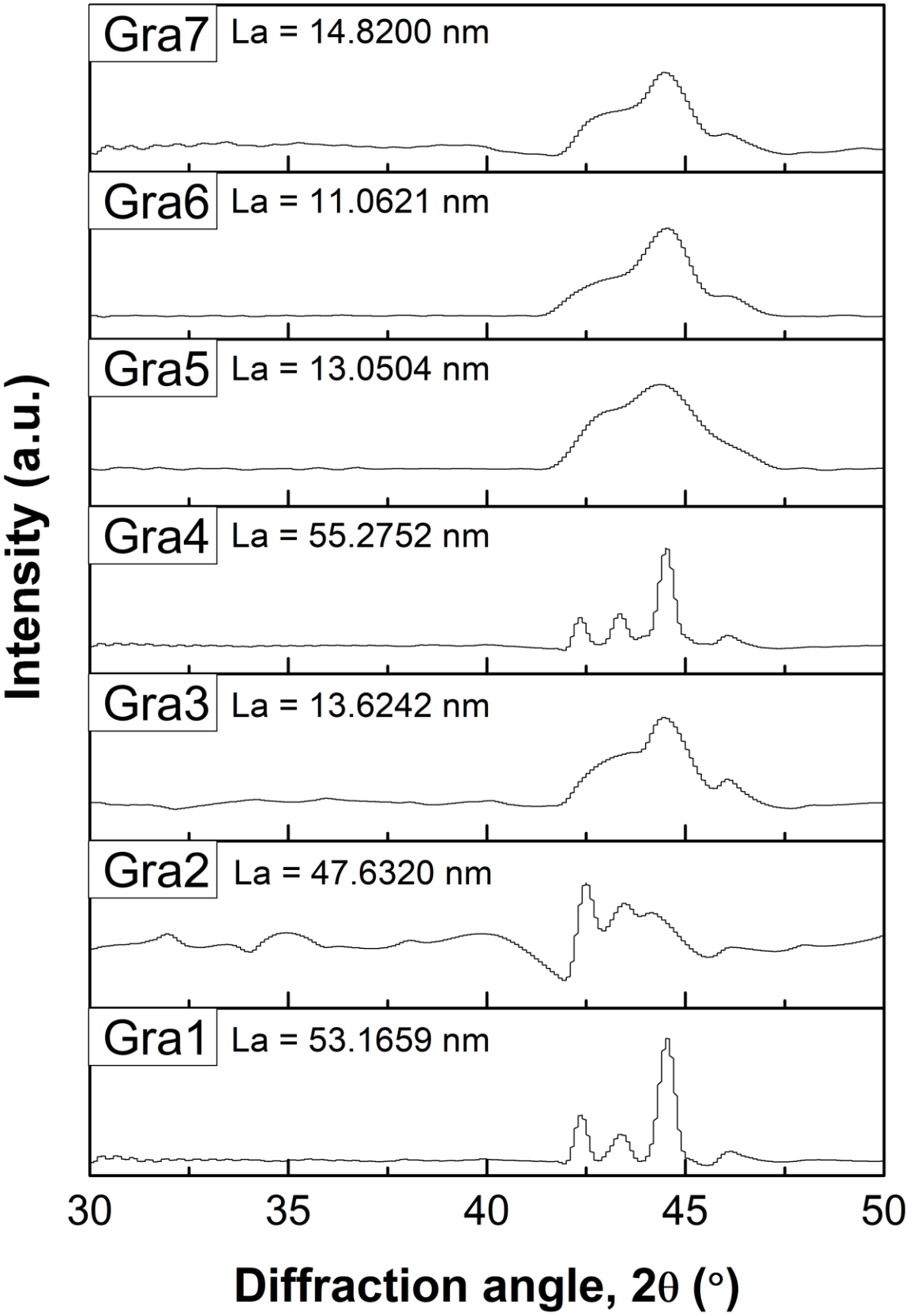
Gra7
La = 14.8200 nm
Gra6
La = 11.0621 nm
Gra5
La = 13.0504 nm
Gra4
La = 55.2752 nm
Gra3
La = 13.6242 nm
Gra2
La = 47.6320 nm
Gra1
La = 53.1659 nm
Intensity (a.u.)
30
35
40
45
50
Diffraction angle, 2θ (°)

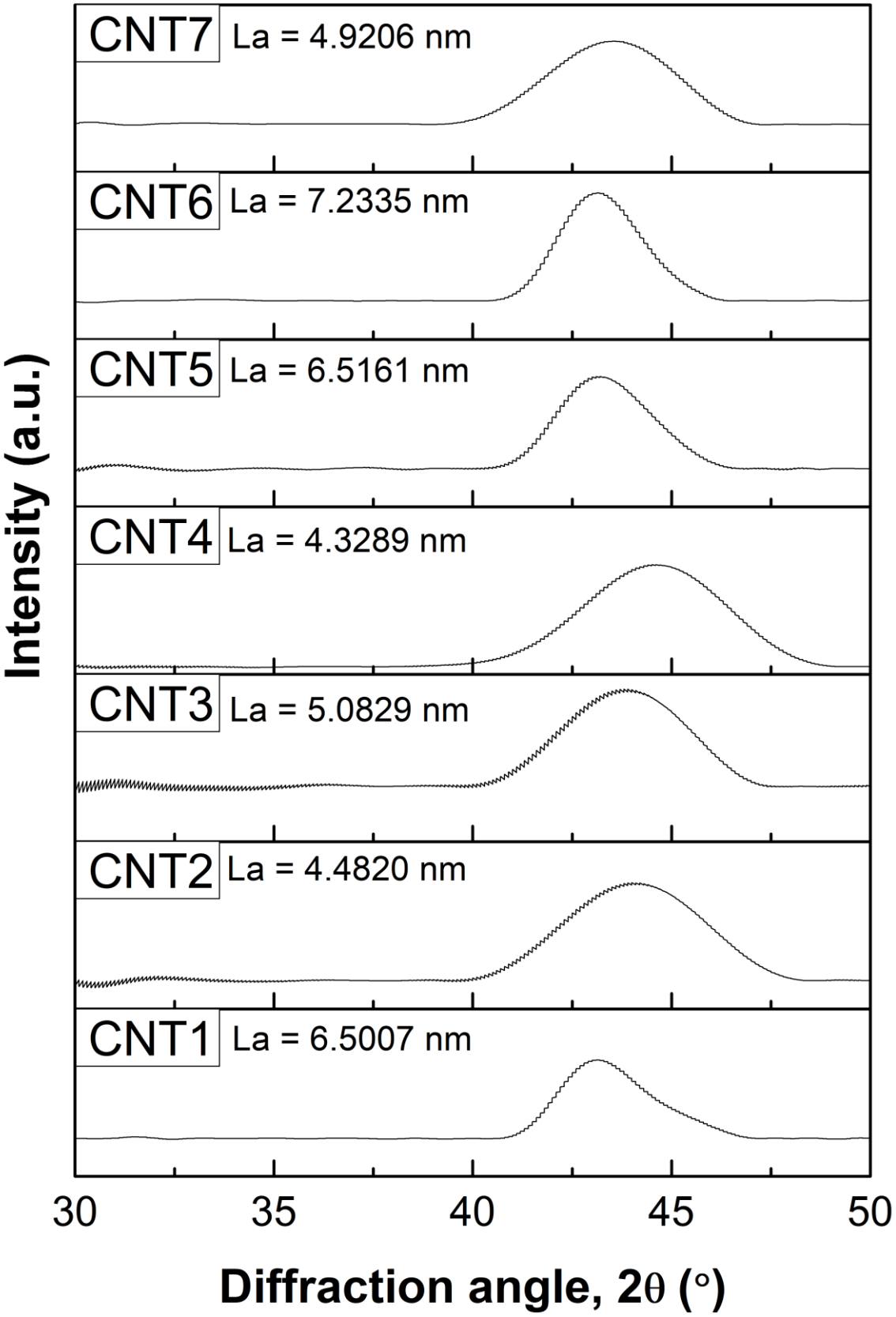
CNT7
La = 4.9206 nm
CNT6
La = 7.2335 nm
CNT5
La = 6.5161 nm
CNT4
La = 4.3289 nm
CNT3
La = 5.0829 nm
CNT2
La = 4.4820 nm
CNT1
La = 6.5007 nm
Intensity (a.u.)
30
35
40
45
50
Diffraction angle, 2θ (°)

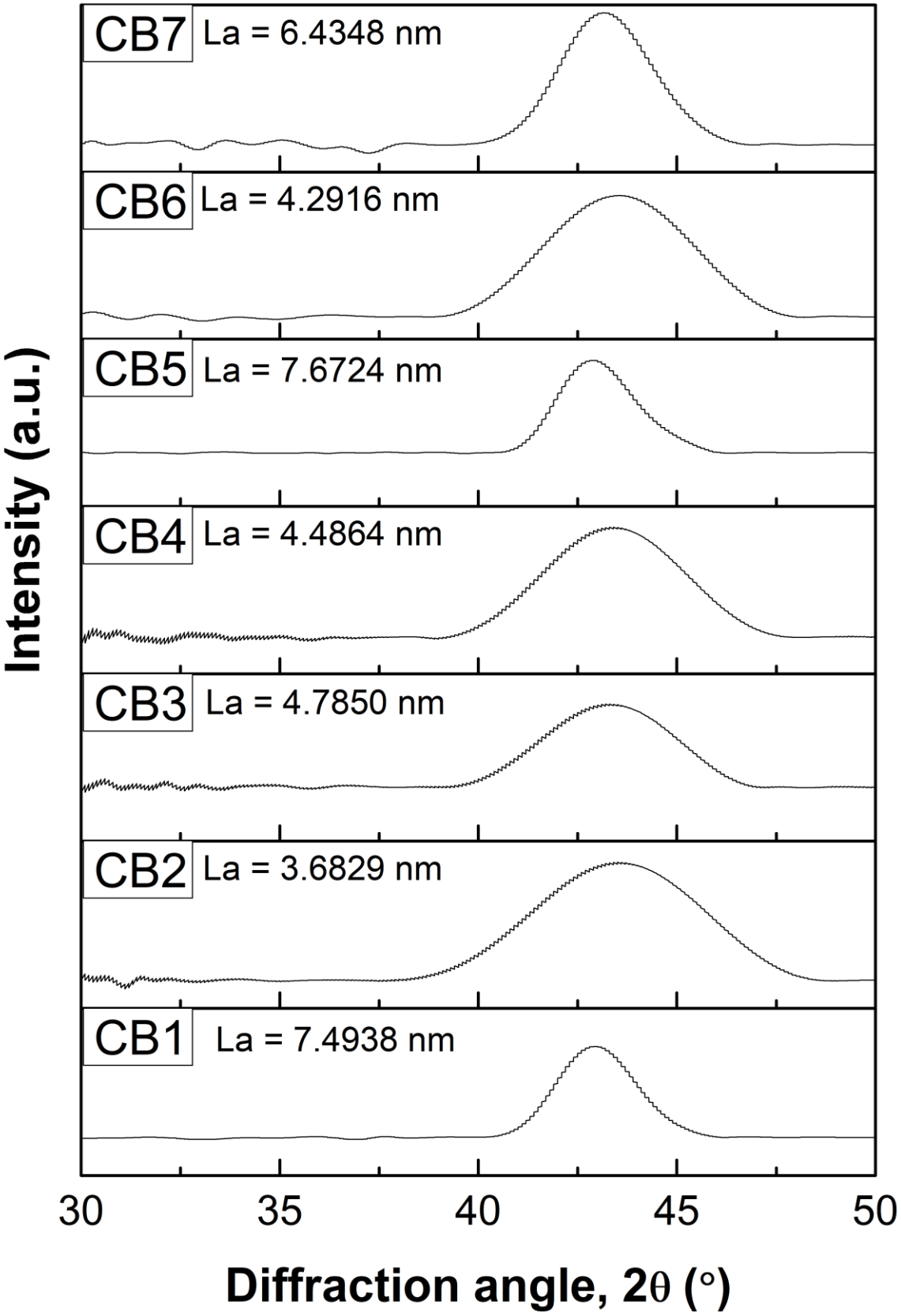
CB7
La = 6.4348 nm
CB6
La = 4.2916 nm
CB5
La = 7.6724 nm
CB4
La = 4.4864 nm
CB3
La = 4.7850 nm
CB2
La = 3.6829 nm
CB1
La = 7.4938 nm
Intensity (a.u.)
30
35
40
45
50
Diffraction angle, 2θ (°)

(c) Raman

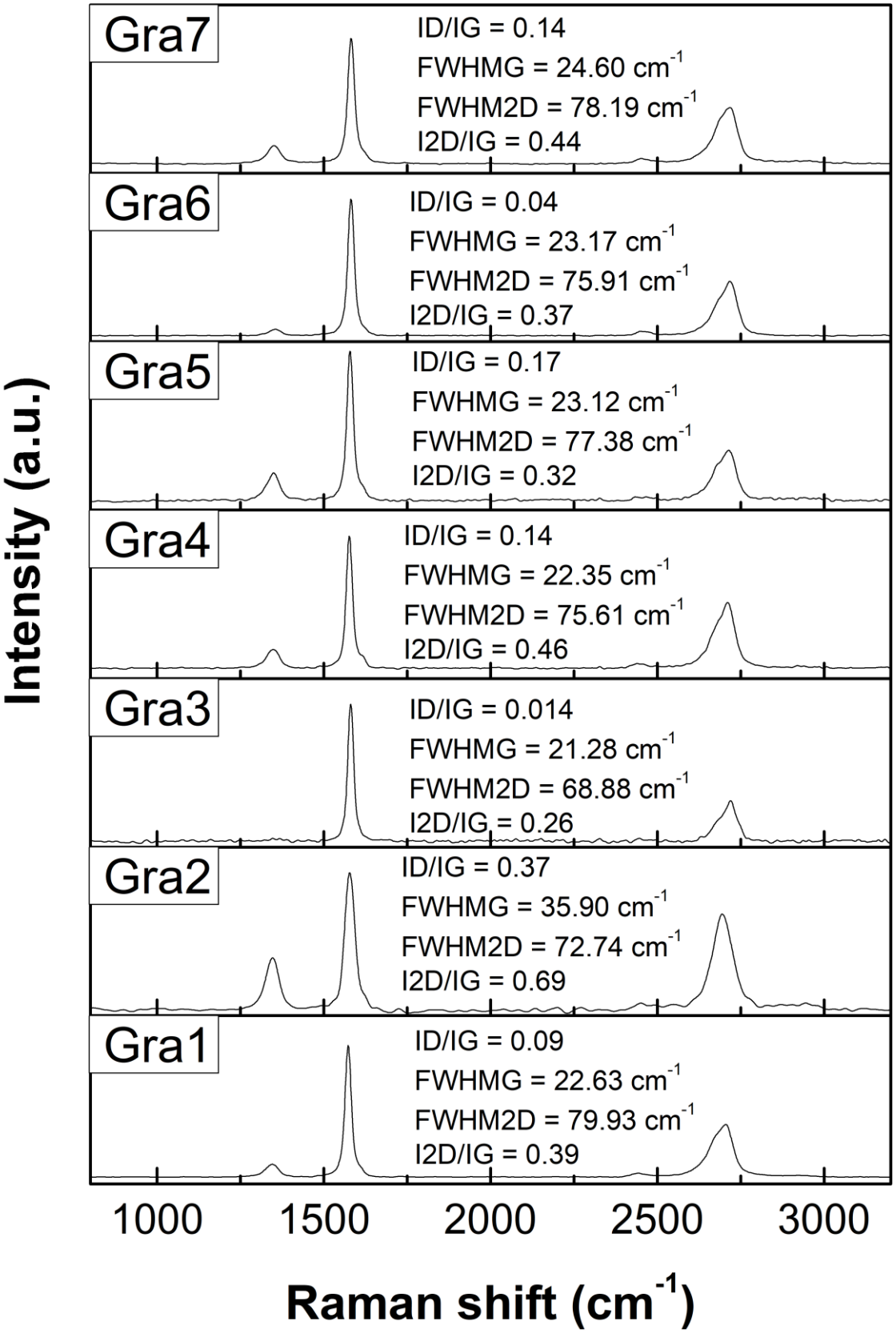
Gra7
ID/IG = 0.14
FWHMG = 24.60 cm-1
FWHM2D = 78.19 cm-1
I2D/IG = 0.44
Gra6
ID/IG = 0.04
FWHMG = 23.17 cm-1
FWHM2D = 75.91 cm-1
I2D/IG = 0.37
Gra5
ID/IG = 0.17
FWHMG = 23.12 cm-1
FWHM2D = 77.38 cm-1
I2D/IG = 0.32
Gra4
ID/IG = 0.14
FWHMG = 22.35 cm-1
FWHM2D = 75.61 cm-1
I2D/IG = 0.46
Gra3
ID/IG = 0.014
FWHMG = 21.28 cm-1
FWHM2D = 68.88 cm-1
I2D/IG = 0.26
Gra2
ID/IG = 0.37
FWHMG = 35.90 cm-1
FWHM2D = 72.74 cm-1
I2D/IG = 0.69
Gra1
ID/IG = 0.09
FWHMG = 22.63 cm-1
FWHM2D = 79.93 cm-1
I2D/IG = 0.39
Intensity (a.u.)
1000
1500
2000
2500
3000
Raman shift (cm-1)

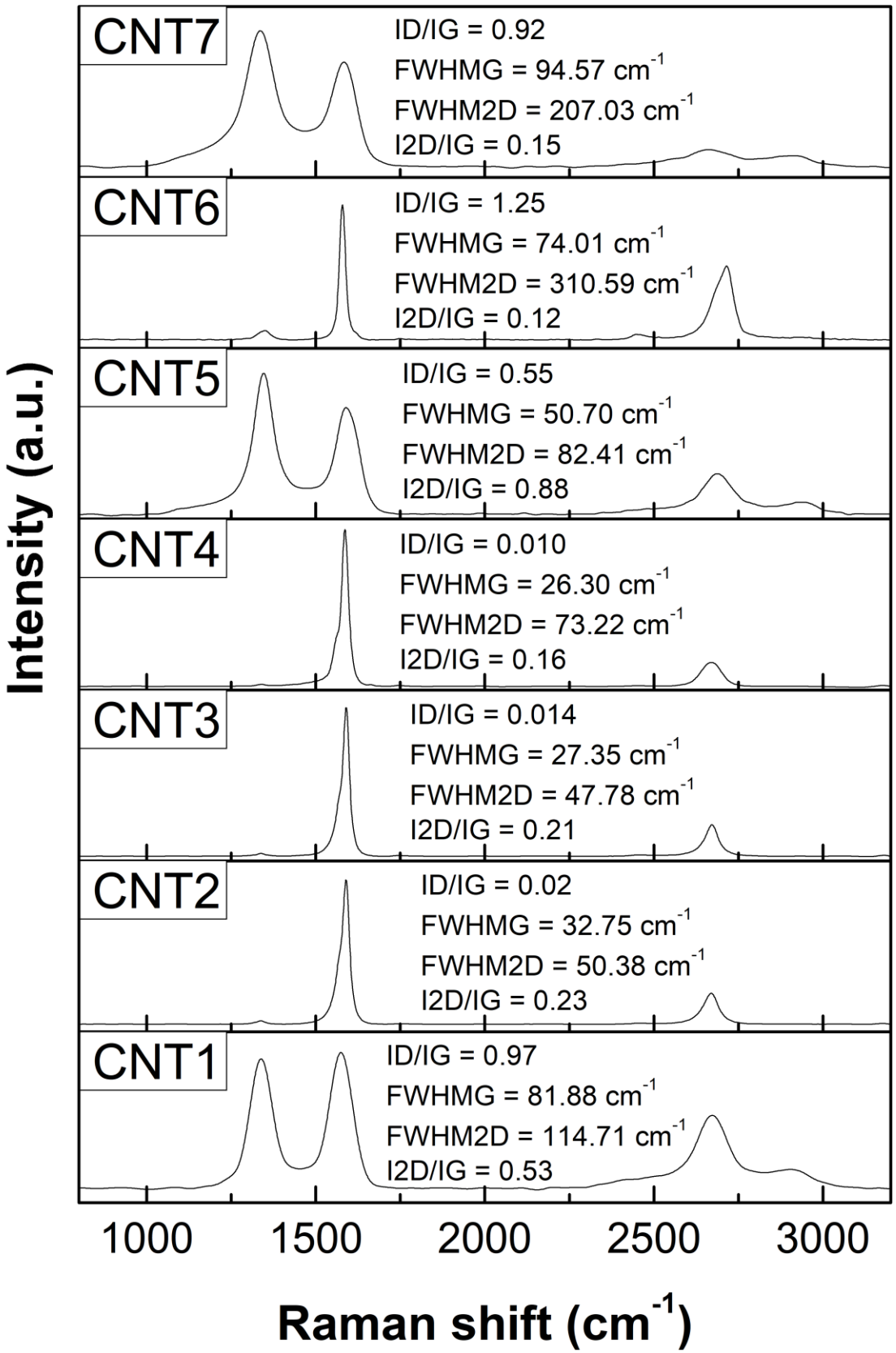
CNT7
ID/IG = 0.92
FWHMG = 94.57 cm-1
FWHM2D = 207.03 cm-1
I2D/IG = 0.15
CNT6
ID/IG = 1.25
FWHMG = 74.01 cm-1
FWHM2D = 310.59 cm-1
I2D/IG = 0.12
CNT5
ID/IG = 0.55
FWHMG = 50.70 cm-1
FWHM2D = 82.41 cm-1
I2D/IG = 0.88
CNT4
ID/IG = 0.010
FWHMG = 26.30 cm-1
FWHM2D = 73.22 cm-1
I2D/IG = 0.16
CNT3
ID/IG = 0.014
FWHMG = 27.35 cm-1
FWHM2D = 47.78 cm-1
I2D/IG = 0.21
CNT2
ID/IG = 0.02
FWHMG = 32.75 cm-1
FWHM2D = 50.38 cm-1
I2D/IG = 0.23
CNT1
ID/IG = 0.97
FWHMG = 81.88 cm-1
FWHM2D = 114.71 cm-1
I2D/IG = 0.53
Intensity (a.u.)
1000
1500
2000
2500
3000
Raman shift (cm-1)

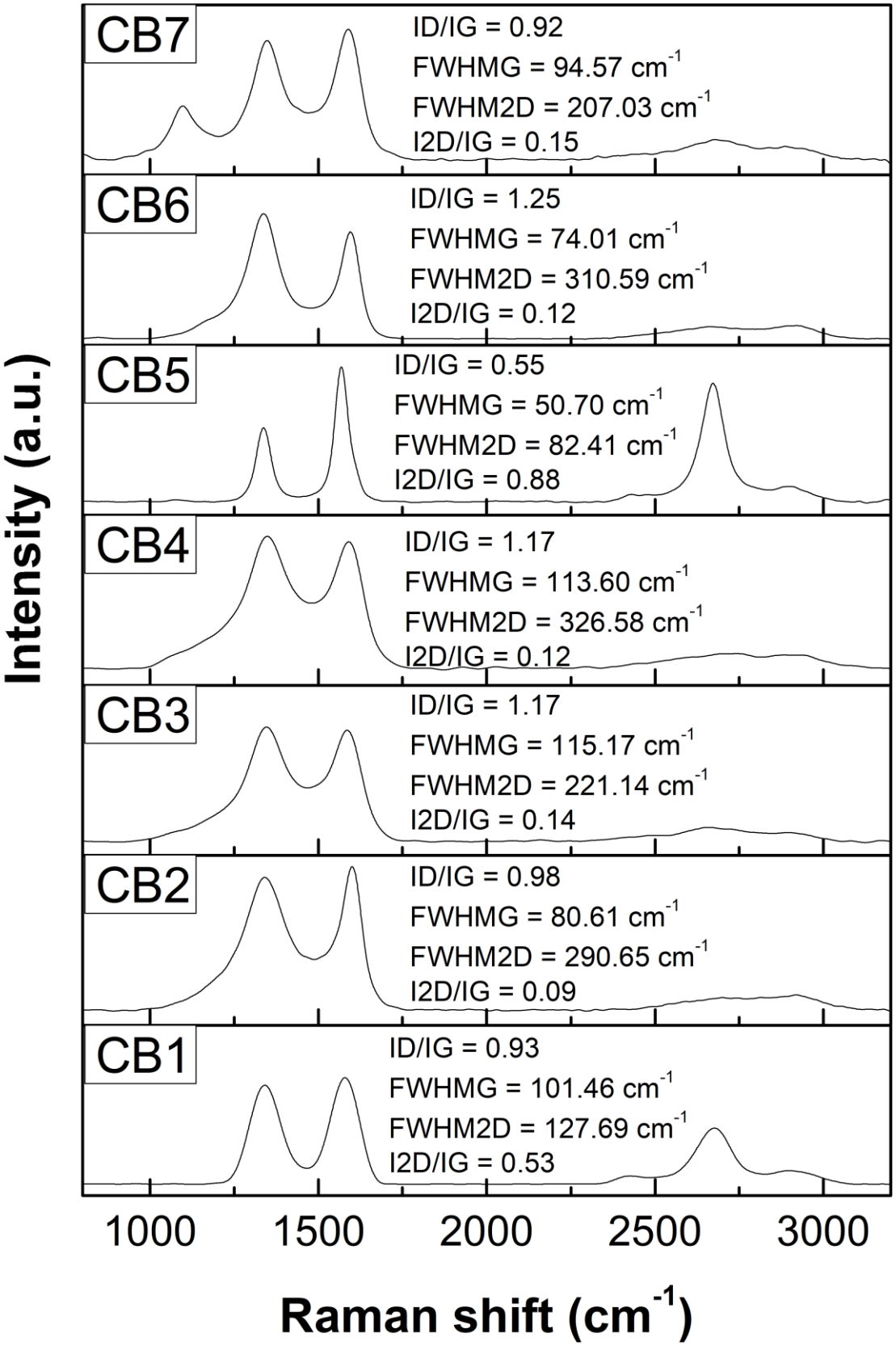
CB7
ID/IG = 0.92
FWHMG = 94.57 cm-1
FWHM2D = 207.03 cm-1
I2D/IG = 0.15
CB6
ID/IG = 1.25
FWHMG = 74.01 cm-1
FWHM2D = 310.59 cm-1
I2D/IG = 0.12
CB5
ID/IG = 0.55
FWHMG = 50.70 cm-1
FWHM2D = 82.41 cm-1
I2D/IG = 0.88
CB4
ID/IG = 1.17
FWHMG = 113.60 cm-1
FWHM2D = 326.58 cm-1
I2D/IG = 0.12
CB3
ID/IG = 1.17
FWHMG = 115.17 cm-1
FWHM2D = 221.14 cm-1
I2D/IG = 0.14
CB2
ID/IG = 0.98
FWHMG = 80.61 cm-1
FWHM2D = 290.65 cm-1
I2D/IG = 0.09
CB1
ID/IG = 0.93
FWHMG = 101.46 cm-1
FWHM2D = 127.69 cm-1
I2D/IG = 0.53
Intensity (a.u.)
1000
1500
2000
2500
3000
Raman shift (cm-1)

(d) SEM

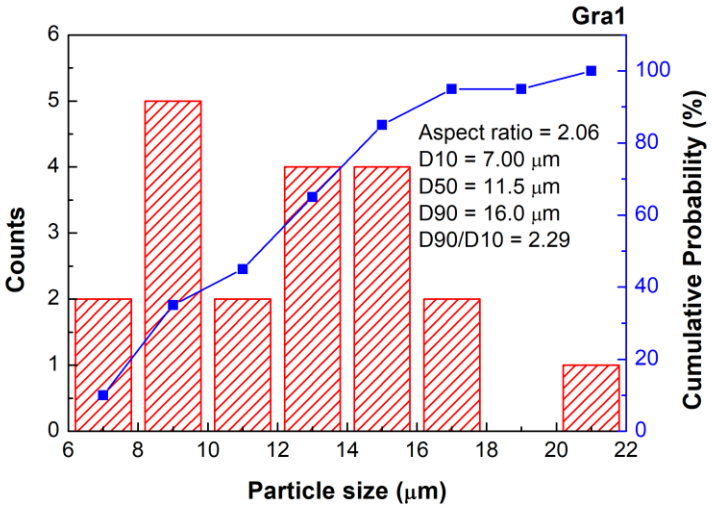
Gra1
Counts
Cumulative Probability (%)
Particle size (μm)
Aspect ratio = 2.06
D10 = 7.00 μm
D50 = 11.5 μm
D90 = 16.0 μm
D90/D10 = 2.29

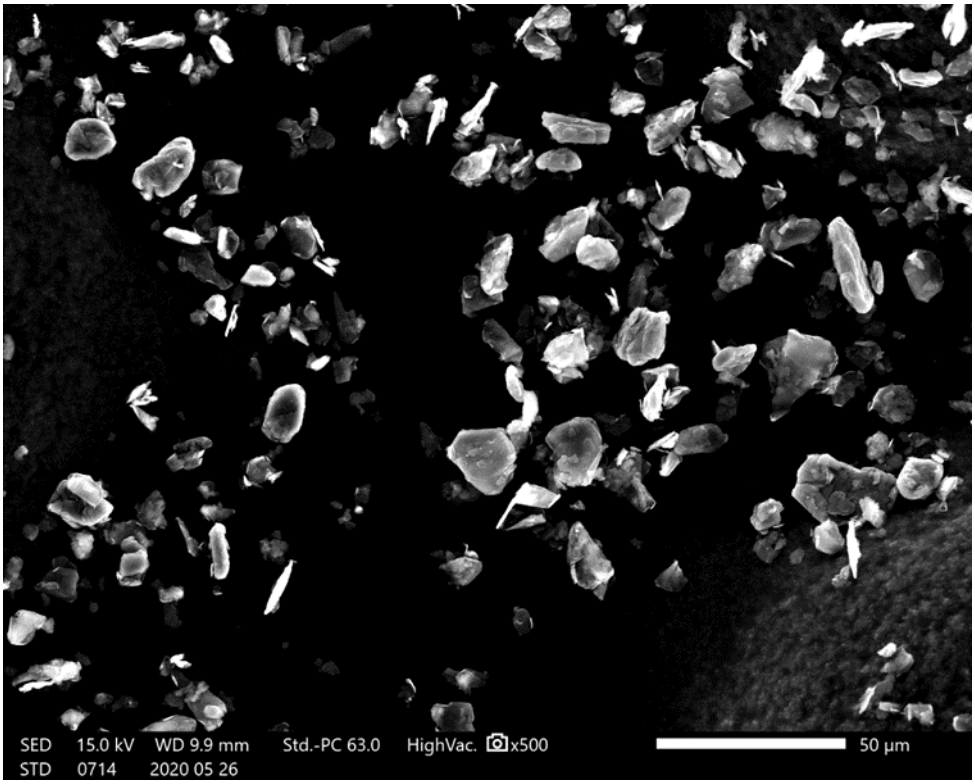
SED 15.0 kV WD 9.9 mm Std.-PC 63.0 HighVac. x500 50 μm
STD 0714 2020 05 26

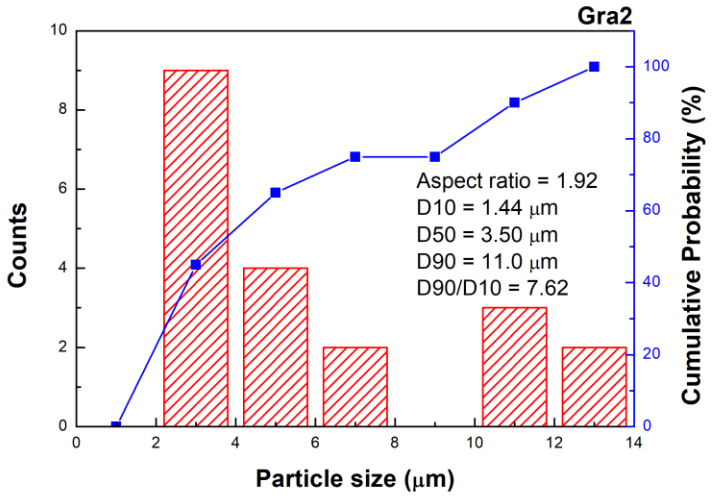
Gra2
Counts
Cumulative Probability (%)
Particle size (μm)
Aspect ratio = 1.92
D10 = 1.44 μm
D50 = 3.50 μm
D90 = 11.0 μm
D90/D10 = 7.62

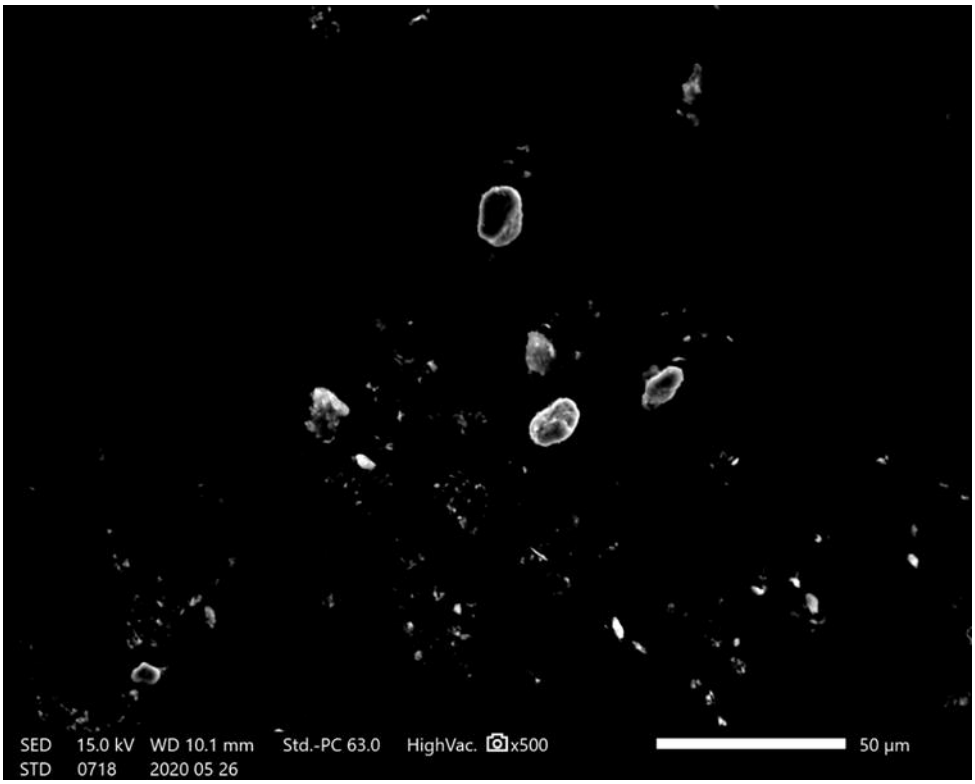
SED 15.0 kV WD 10.1 mm Std.-PC 63.0 HighVac. x500 50 μm
STD 0718 2020 05 26

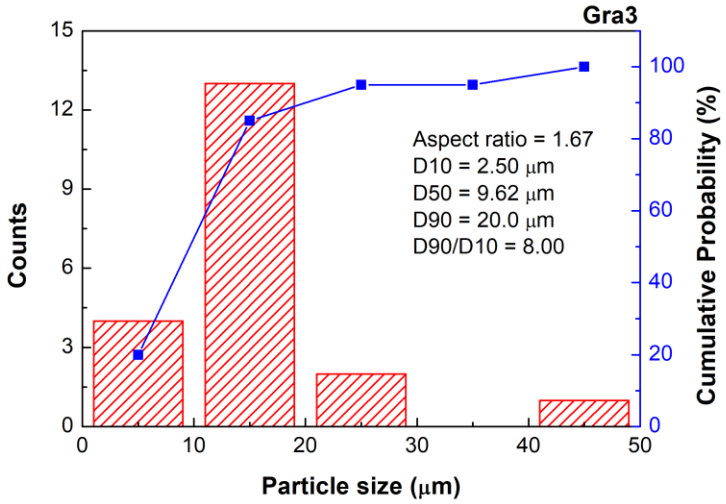
Gra3
Counts
Cumulative Probability (%)
Particle size (μm)
Aspect ratio = 1.67
D10 = 2.50 μm
D50 = 9.62 μm
D90 = 20.0 μm
D90/D10 = 8.00
0
3
6
9
12
15
0
20
40
60
80
100
0
10
20
30
40
50

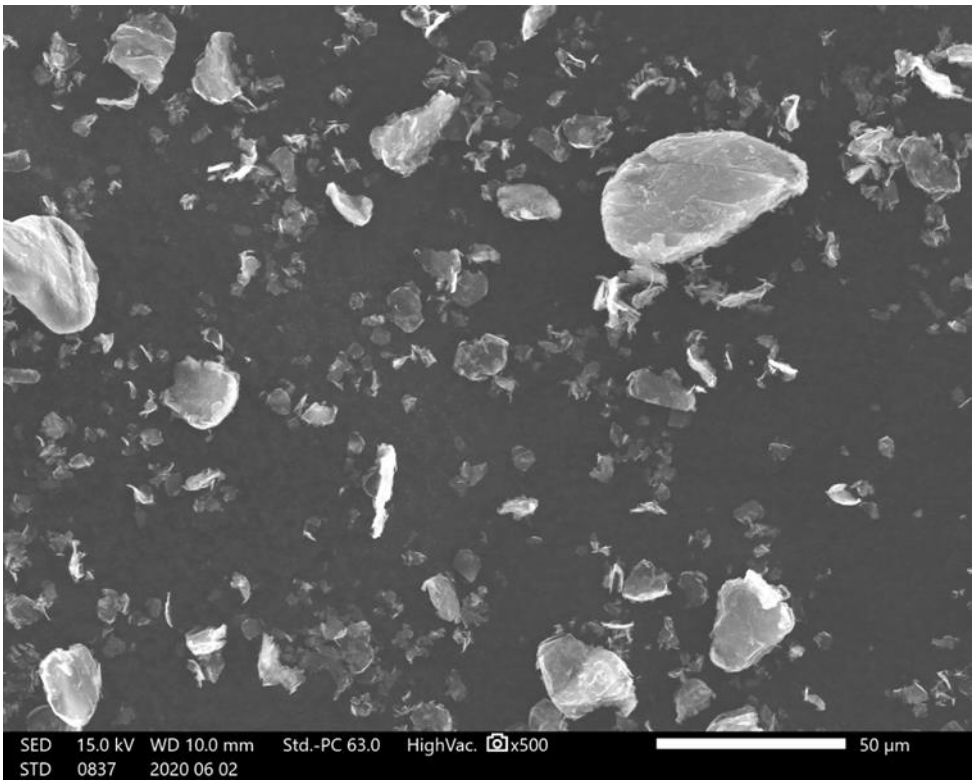
SED 15.0 kV WD 10.0 mm Std.-PC 63.0 HighVac. x500 50 μm
STD 0837 2020 06 02

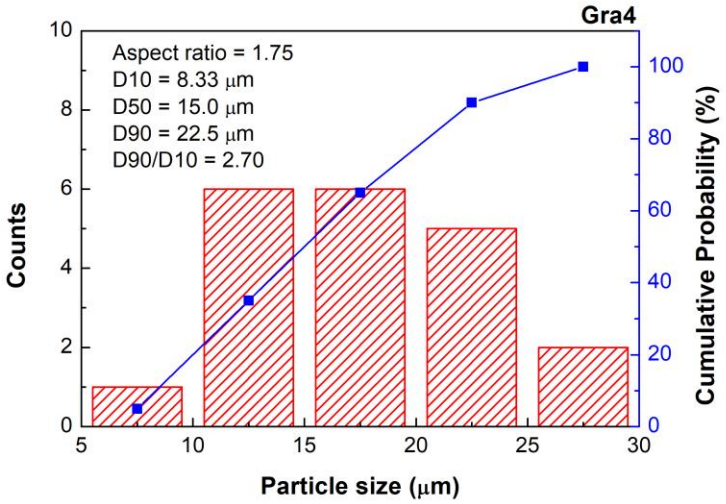
Gra4
Aspect ratio = 1.75
D10 = 8.33 μm
D50 = 15.0 μm
D90 = 22.5 μm
D90/D10 = 2.70
Counts
Cumulative Probability (%)
Particle size (μm)
0
2
4
6
8
10
0
20
40
60
80
100
5
10
15
20
25
30

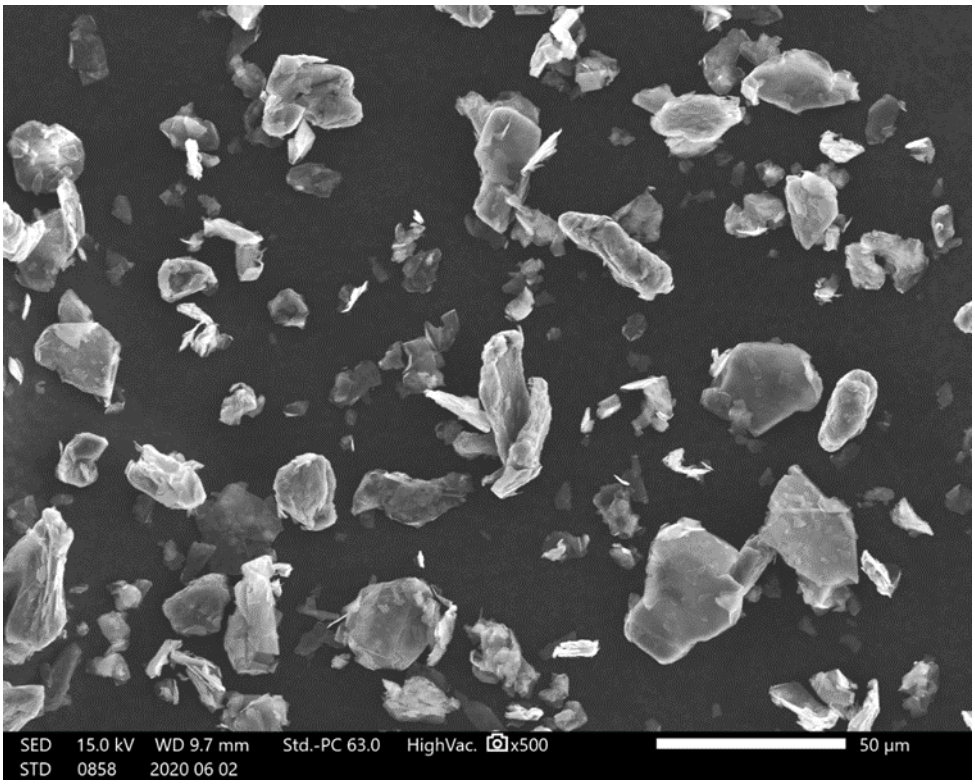
SED 15.0 kV WD 9.7 mm Std.-PC 63.0 HighVac. x500 50 μm
STD 0858 2020 06 02

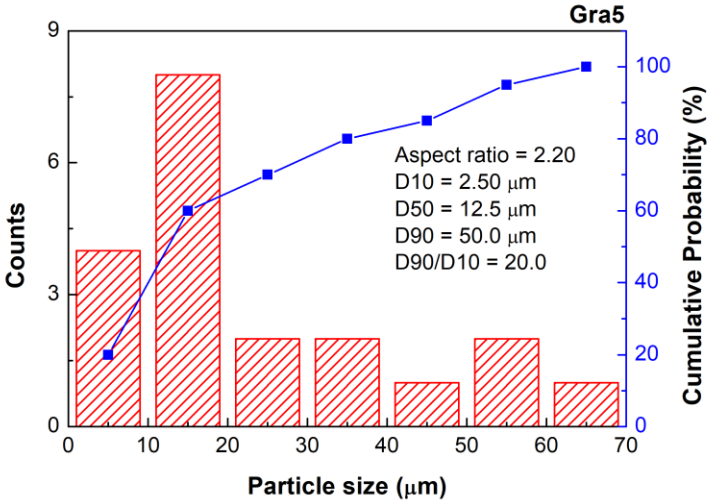
Gra5
Counts
Cumulative Probability (%)
Particle size (μm)
Aspect ratio = 2.20
D10 = 2.50 μm
D50 = 12.5 μm
D90 = 50.0 μm
D90/D10 = 20.0
0
3
6
9
0
20
40
60
80
100
0
10
20
30
40
50
60
70

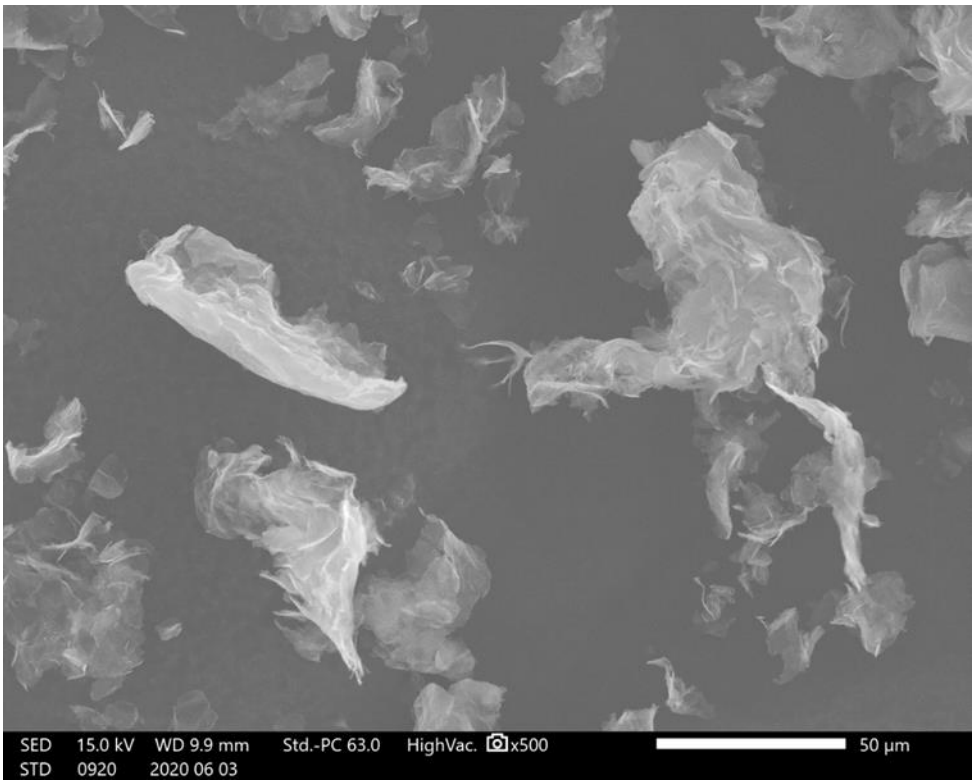
SED 15.0 kV WD 9.9 mm Std.-PC 63.0 HighVac. x500 50 μm
STD 0920 2020 06 03

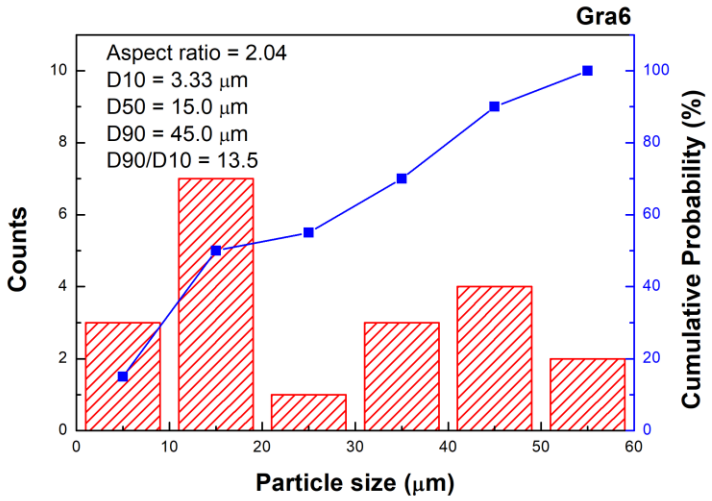
Gra6
Aspect ratio = 2.04
D10 = 3.33 μm
D50 = 15.0 μm
D90 = 45.0 μm
D90/D10 = 13.5
Counts
Cumulative Probability (%)
Particle size (μm)
0
2
4
6
8
10
0
20
40
60
80
100
0
10
20
30
40
50
60

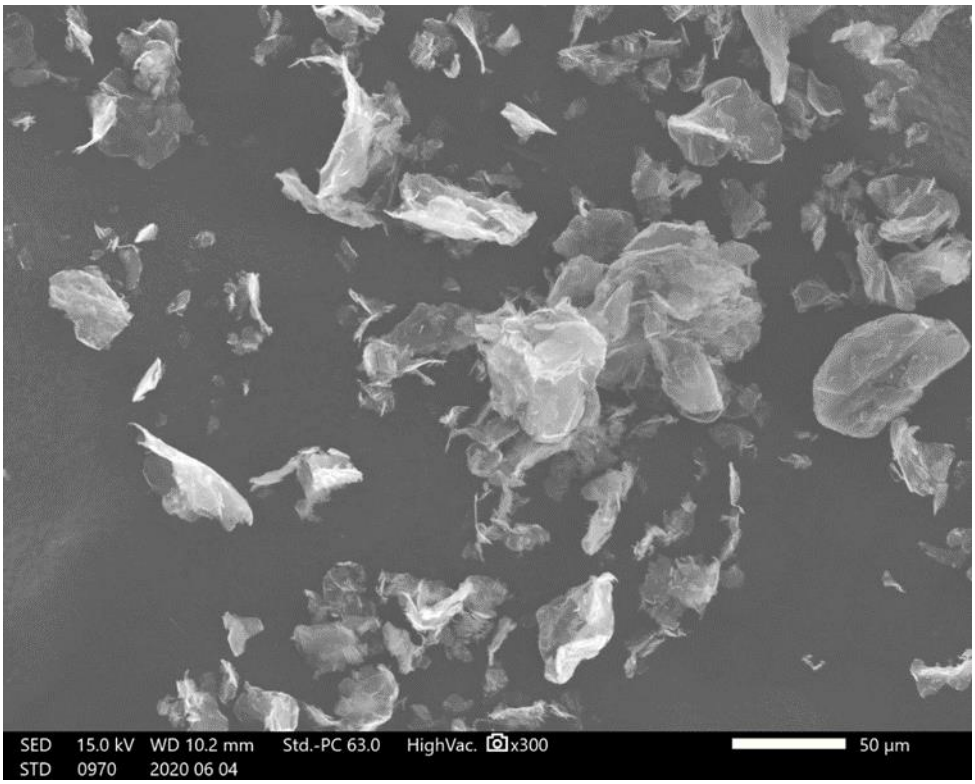
SED 15.0 kV WD 10.2 mm Std.-PC 63.0 HighVac. x300 50 μm
STD 0970 2020 06 04

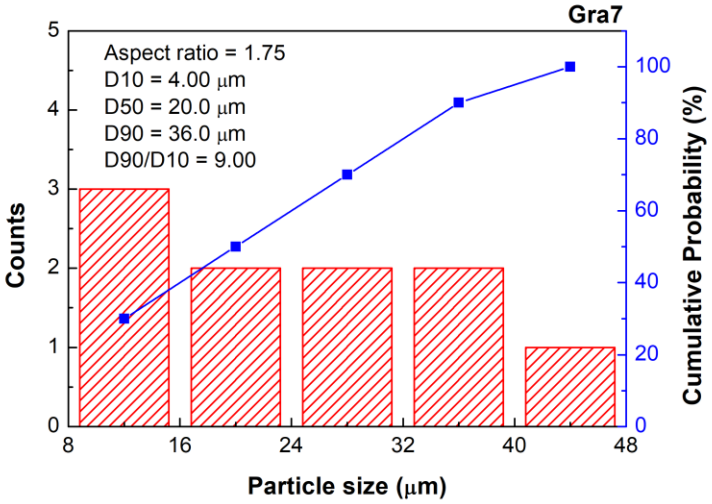
Gra7
Aspect ratio = 1.75
D10 = 4.00 μm
D50 = 20.0 μm
D90 = 36.0 μm
D90/D10 = 9.00
Counts
Cumulative Probability (%)
Particle size (μm)
0
1
2
3
4
5
0
20
40
60
80
100
8
16
24
32
40
48

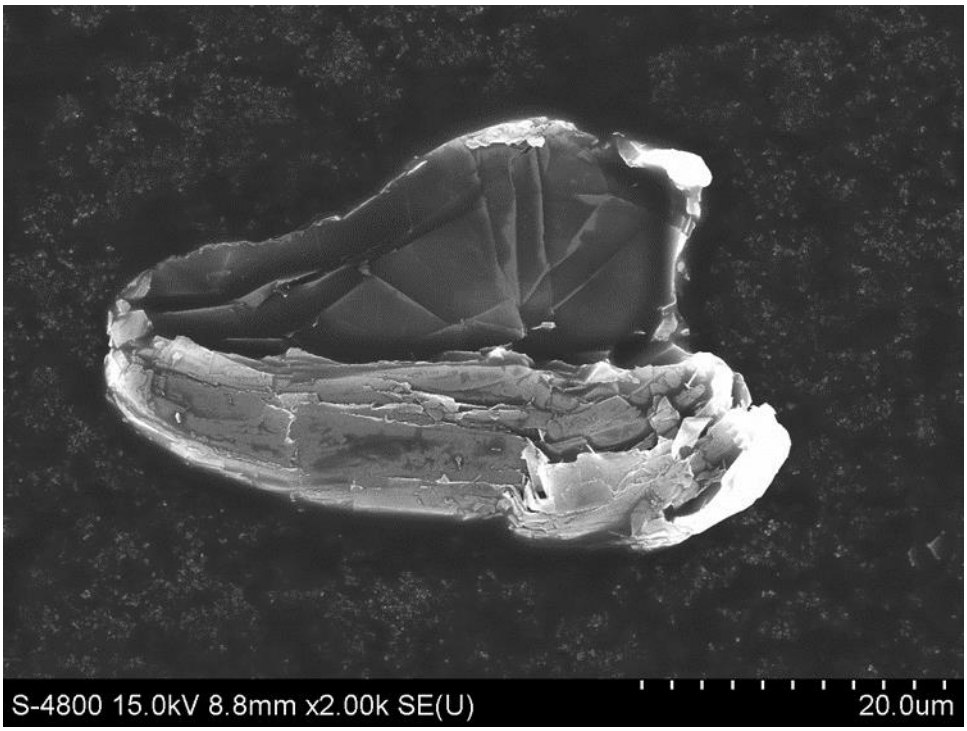
S-4800 15.0kV 8.8mm x2.00k SE(U)
20.0um

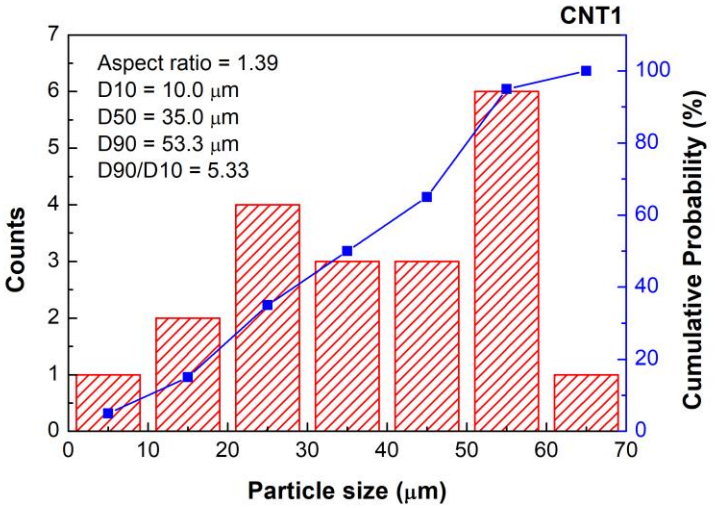
CNT1
Aspect ratio = 1.39
D10 = 10.0 μm
D50 = 35.0 μm
D90 = 53.3 μm
D90/D10 = 5.33
Counts
Cumulative Probability (%)
Particle size (μm)
0
10
20
30
40
50
60
70
0
1
2
3
4
5
6
7
0
20
40
60
80
100

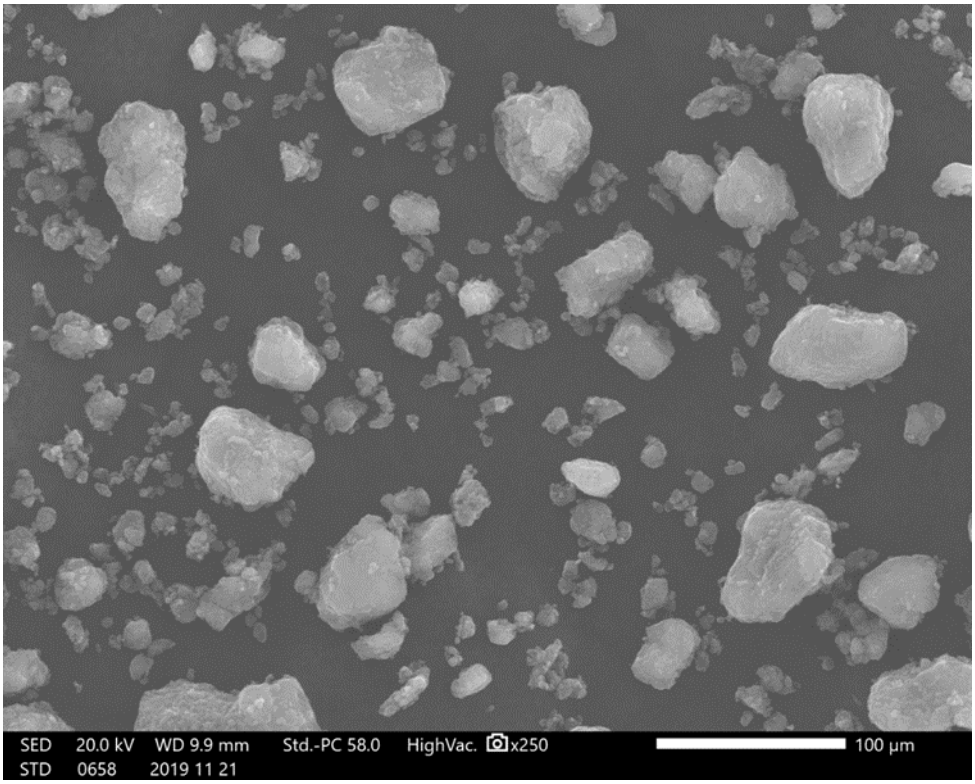
SED 20.0 kV WD 9.9 mm Std.-PC 58.0 HighVac. x250 100 μm
STD 0658 2019 11 21

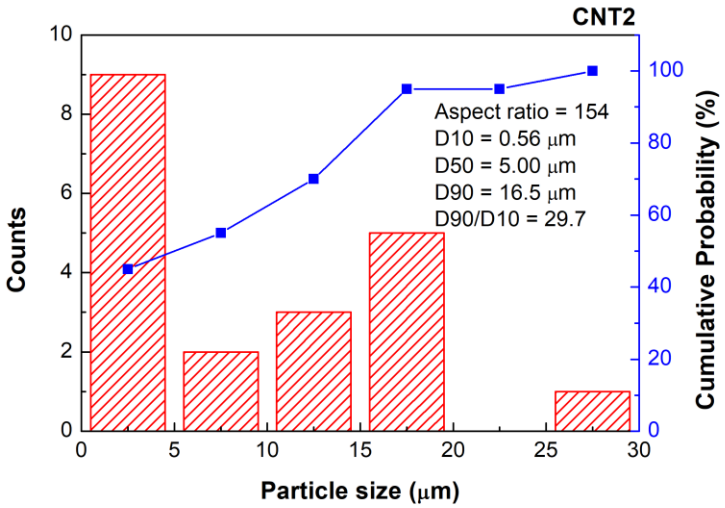
CNT2
Aspect ratio = 154
D10 = 0.56 μm
D50 = 5.00 μm
D90 = 16.5 μm
D90/D10 = 29.7
Counts
Cumulative Probability (%)
Particle size (μm)
0
2
4
6
8
10
0
20
40
60
80
100
0
5
10
15
20
25
30

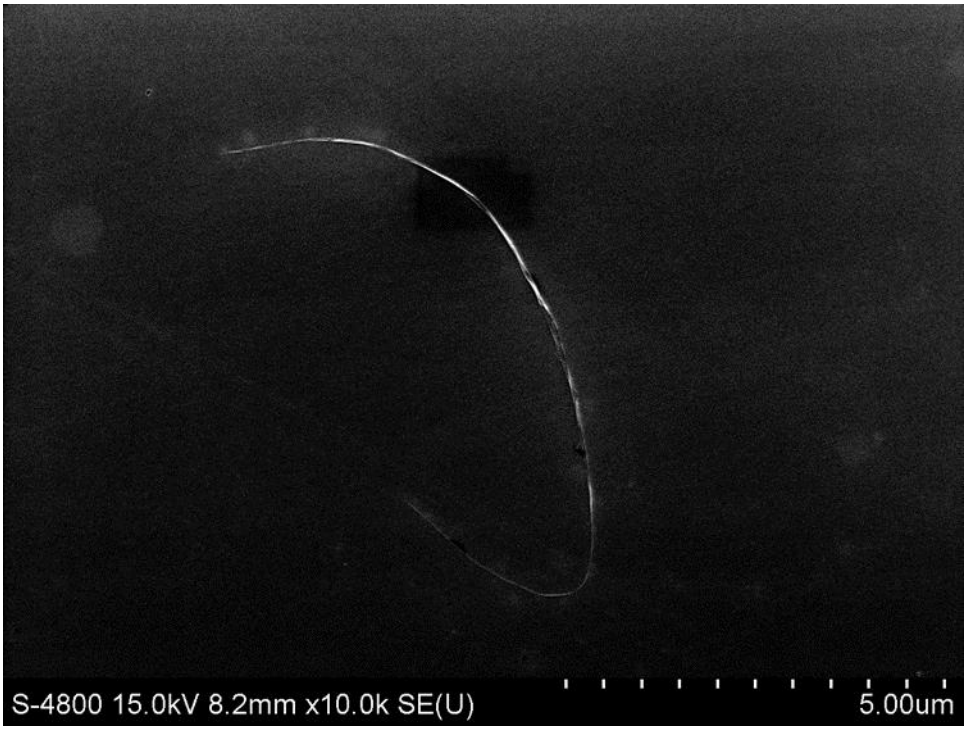
S-4800 15.0kV 8.2mm x10.0k SE(U)
5.00um

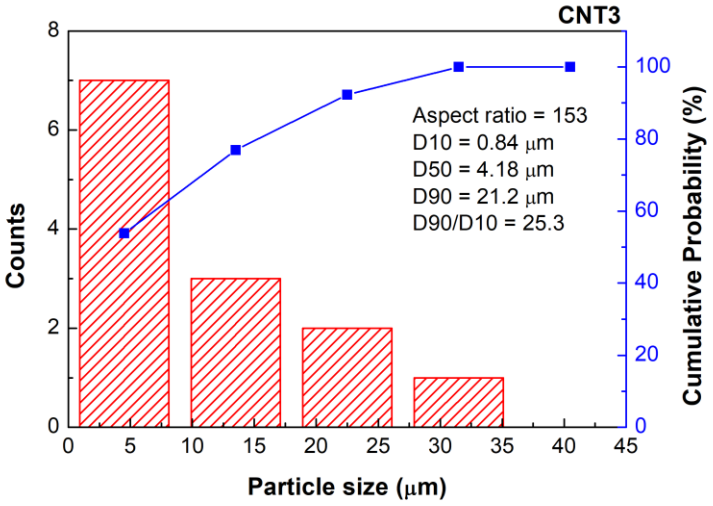
CNT3
Aspect ratio = 153
D10 = 0.84 μm
D50 = 4.18 μm
D90 = 21.2 μm
D90/D10 = 25.3
Counts
Cumulative Probability (%)
Particle size (μm)
0
2
4
6
8
0
20
40
60
80
100
0
5
10
15
20
25
30
35
40
45

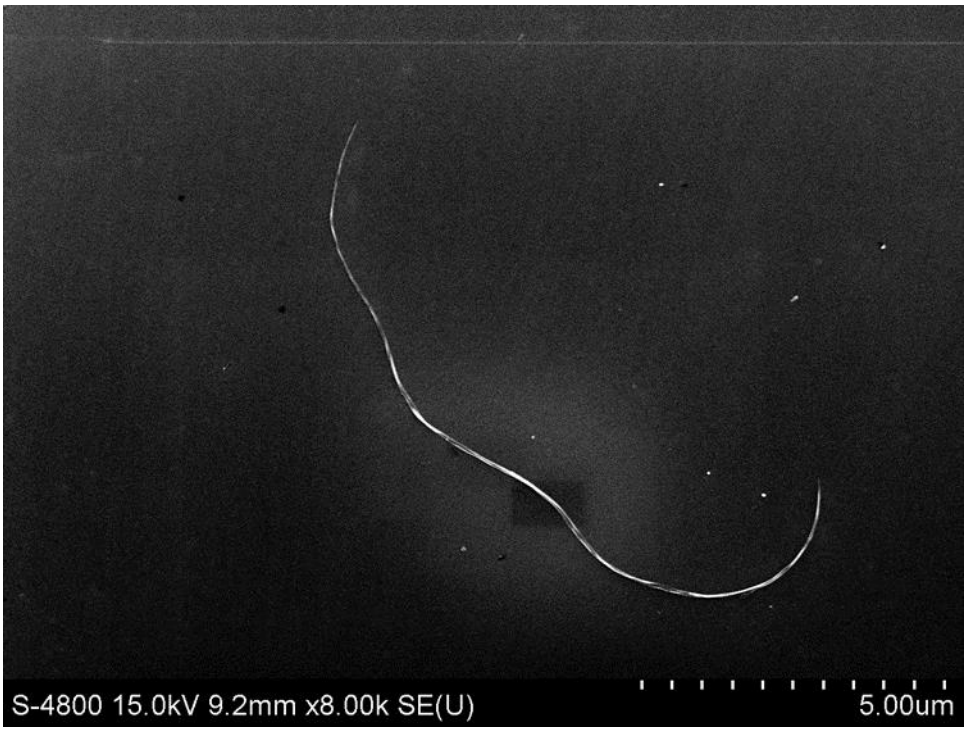
S-4800 15.0kV 9.2mm x8.00k SE(U)
5.00um

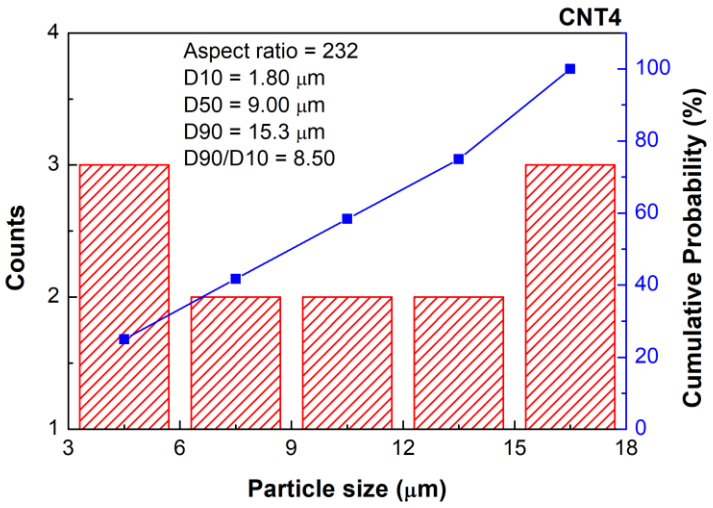
CNT4
Aspect ratio = 232
D10 = 1.80 μm
D50 = 9.00 μm
D90 = 15.3 μm
D90/D10 = 8.50
Counts
Cumulative Probability (%)
Particle size (μm)
1
2
3
4
0
20
40
60
80
100
3
6
9
12
15
18

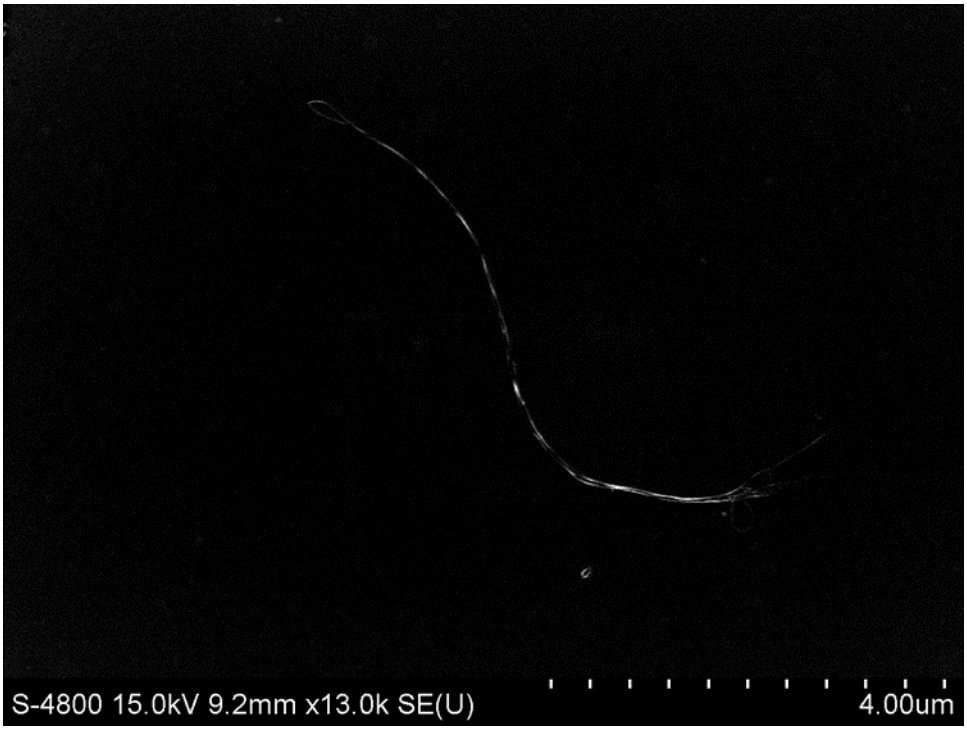
S-4800 15.0kV 9.2mm x13.0k SE(U)
4.00um

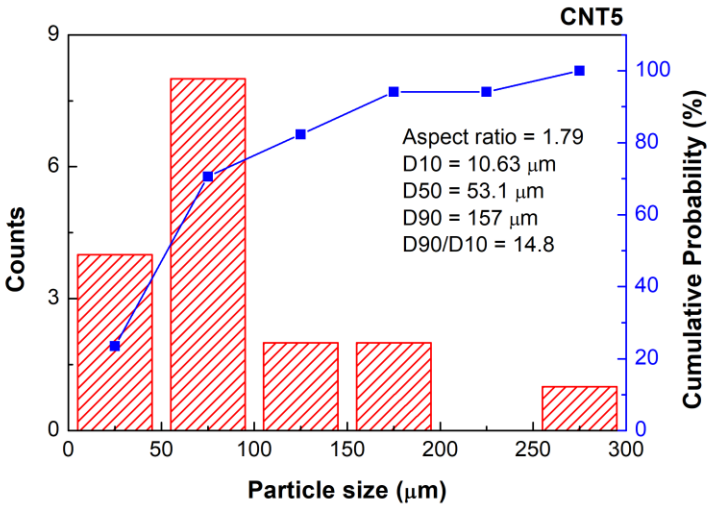
CNT5
Counts
Cumulative Probability (%)
Particle size (μm)
Aspect ratio = 1.79
D10 = 10.63 μm
D50 = 53.1 μm
D90 = 157 μm
D90/D10 = 14.8
0
3
6
9
0
20
40
60
80
100
0
50
100
150
200
250
300

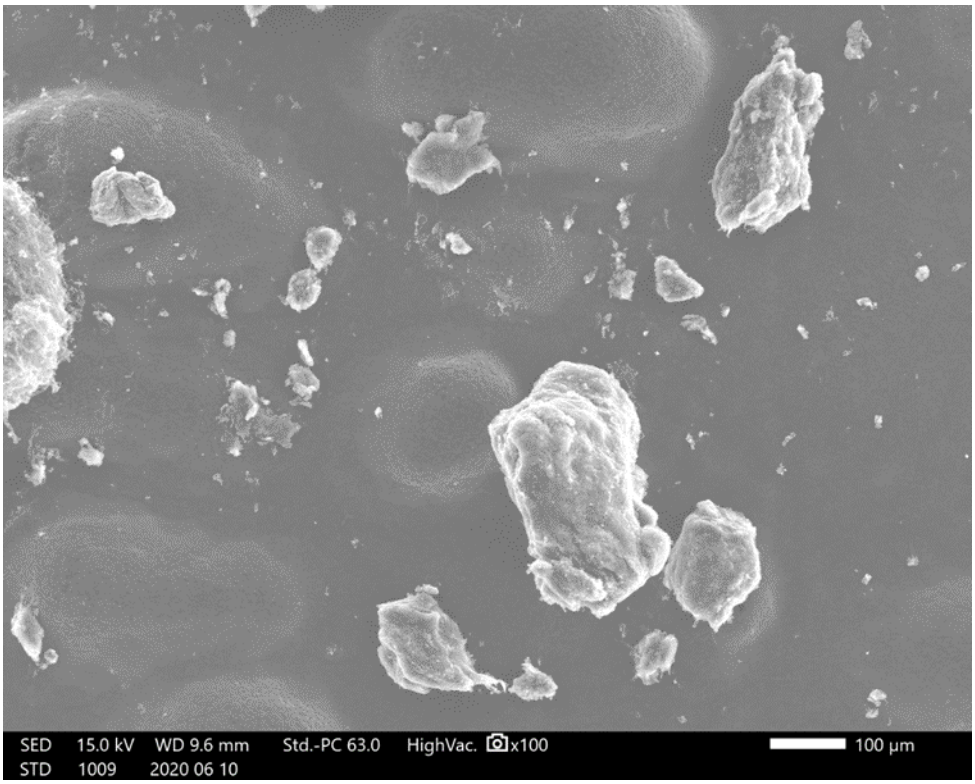
SED 15.0 kV WD 9.6 mm Std.-PC 63.0 HighVac. x100
STD 1009 2020 06 10
100 μm

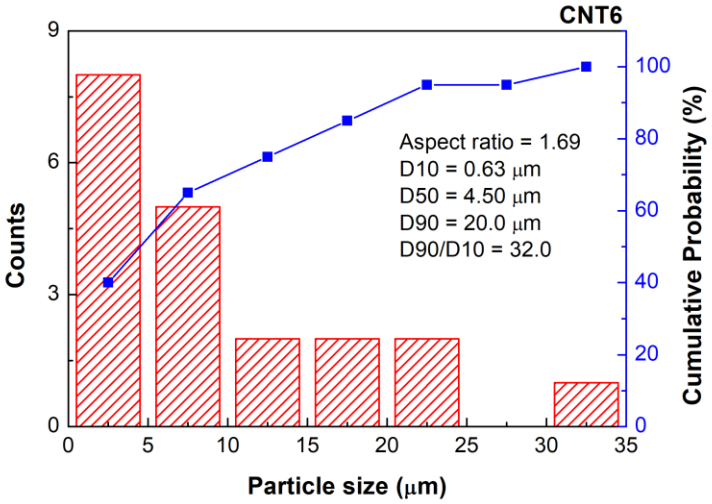
CNT6
Counts
Cumulative Probability (%)
Particle size (μm)
Aspect ratio = 1.69
D10 = 0.63 μm
D50 = 4.50 μm
D90 = 20.0 μm
D90/D10 = 32.0
0
3
6
9
0
20
40
60
80
100
0
5
10
15
20
25
30
35

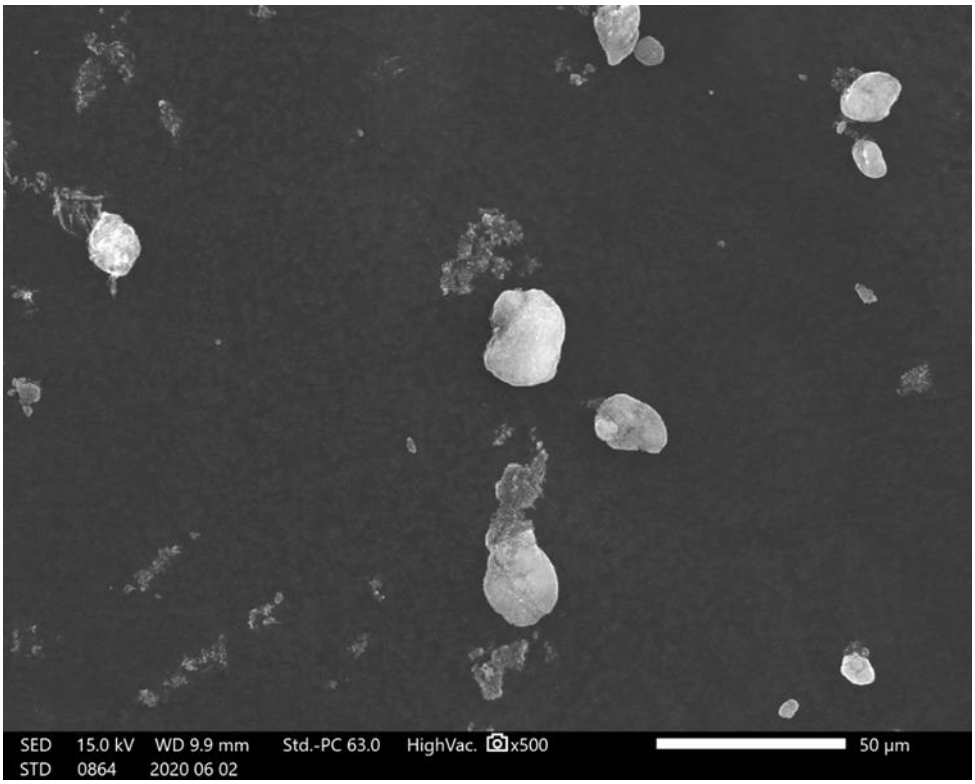
SED 15.0 kV WD 9.9 mm Std.-PC 63.0 HighVac. x500 50 μm
STD 0864 2020 06 02

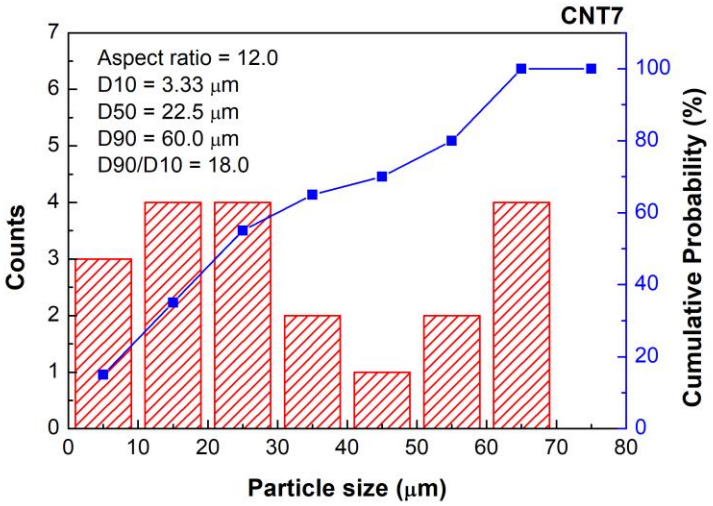
CNT7
Aspect ratio = 12.0
D10 = 3.33 μm
D50 = 22.5 μm
D90 = 60.0 μm
D90/D10 = 18.0
Counts
Cumulative Probability (%)
Particle size (μm)
0
1
2
3
4
5
6
7
0
20
40
60
80
100
0
10
20
30
40
50
60
70
80

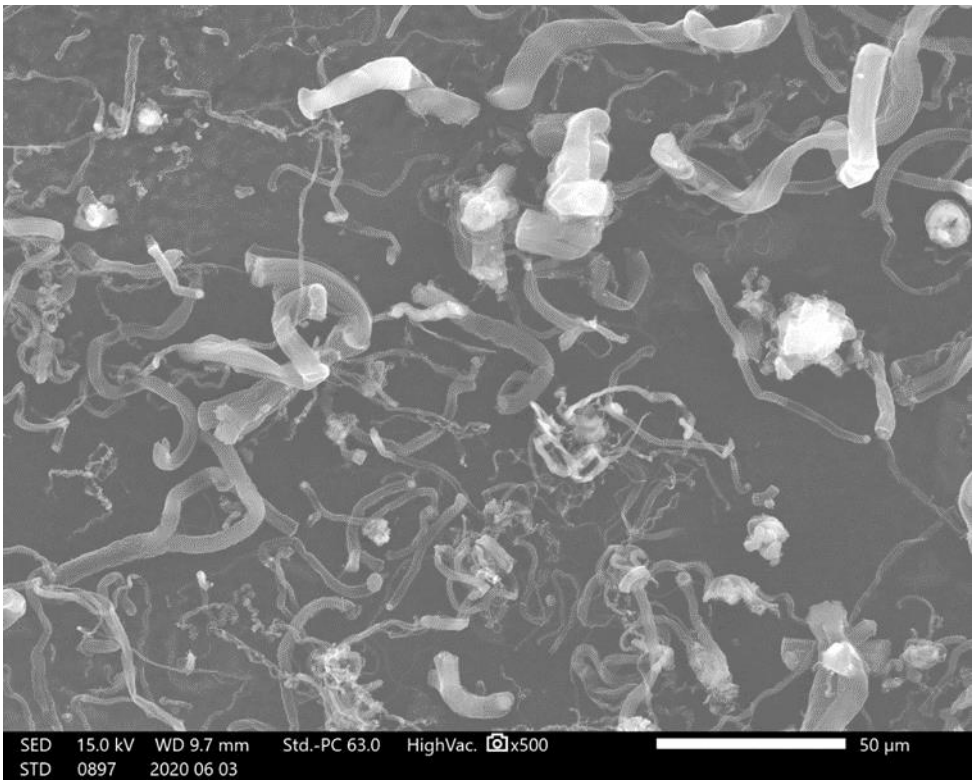
SED 15.0 kV WD 9.7 mm Std.-PC 63.0 HighVac. x500 50 μm
STD 0897 2020 06 03

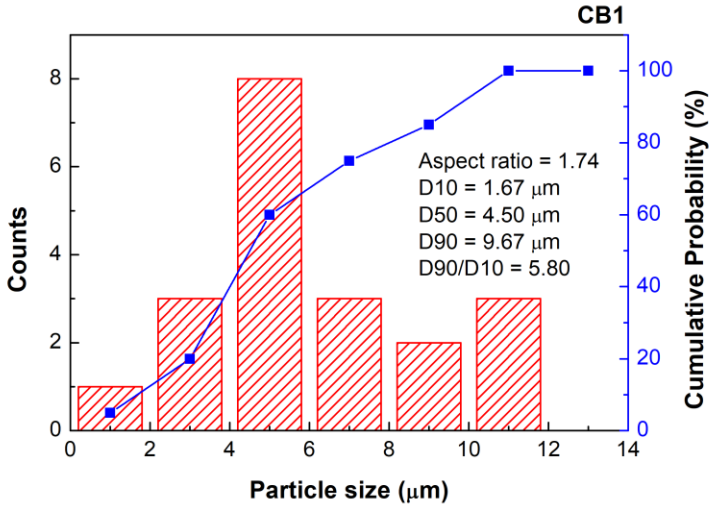
CB1
Counts
Cumulative Probability (%)
Particle size (μm)
Aspect ratio = 1.74
D10 = 1.67 μm
D50 = 4.50 μm
D90 = 9.67 μm
D90/D10 = 5.80
0
2
4
6
8
10
12
14
0
20
40
60
80
100

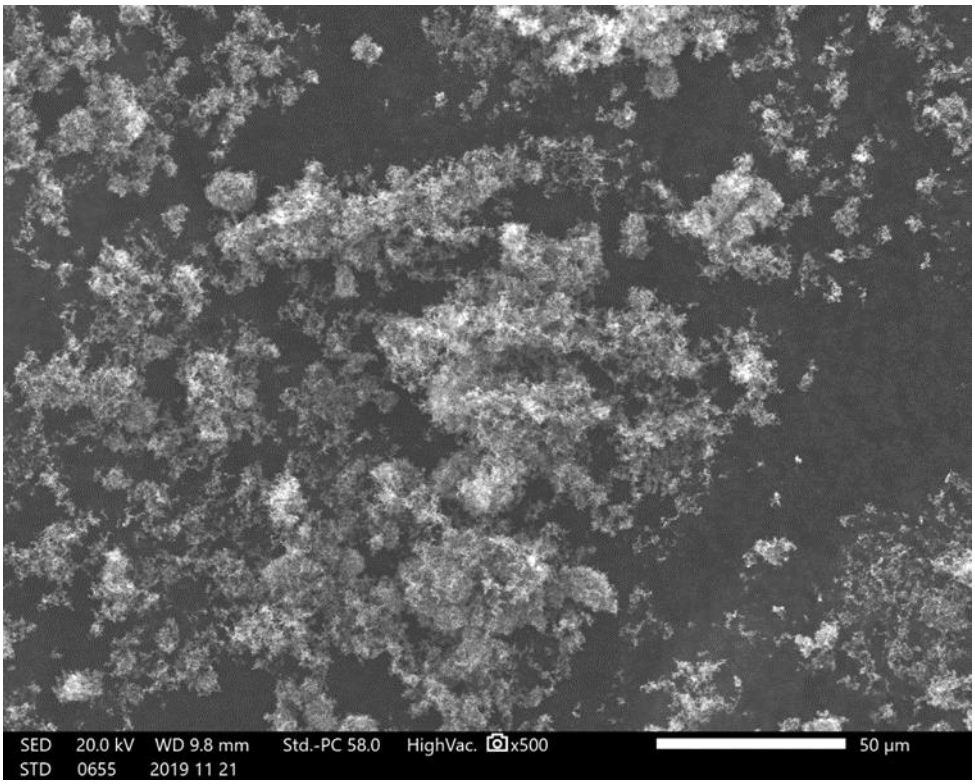
SED 20.0 kV WD 9.8 mm Std.-PC 58.0 HighVac. x500 50 μm
STD 0655 2019 11 21

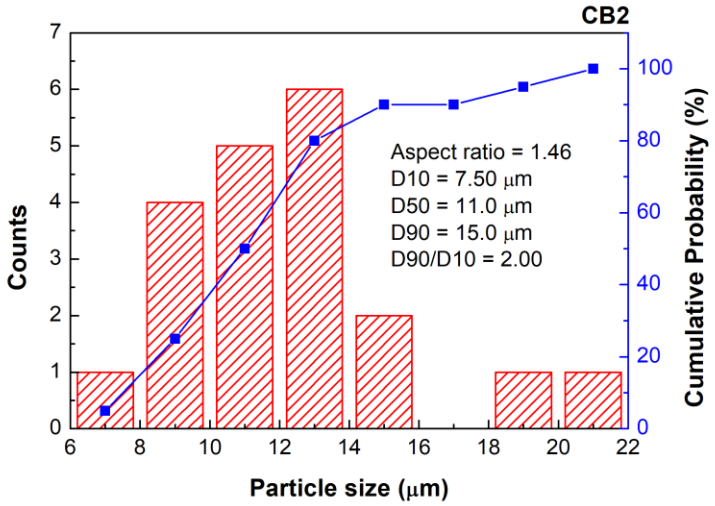
CB2
Counts
Cumulative Probability (%)
Particle size (μm)
Aspect ratio = 1.46
D10 = 7.50 μm
D50 = 11.0 μm
D90 = 15.0 μm
D90/D10 = 2.00

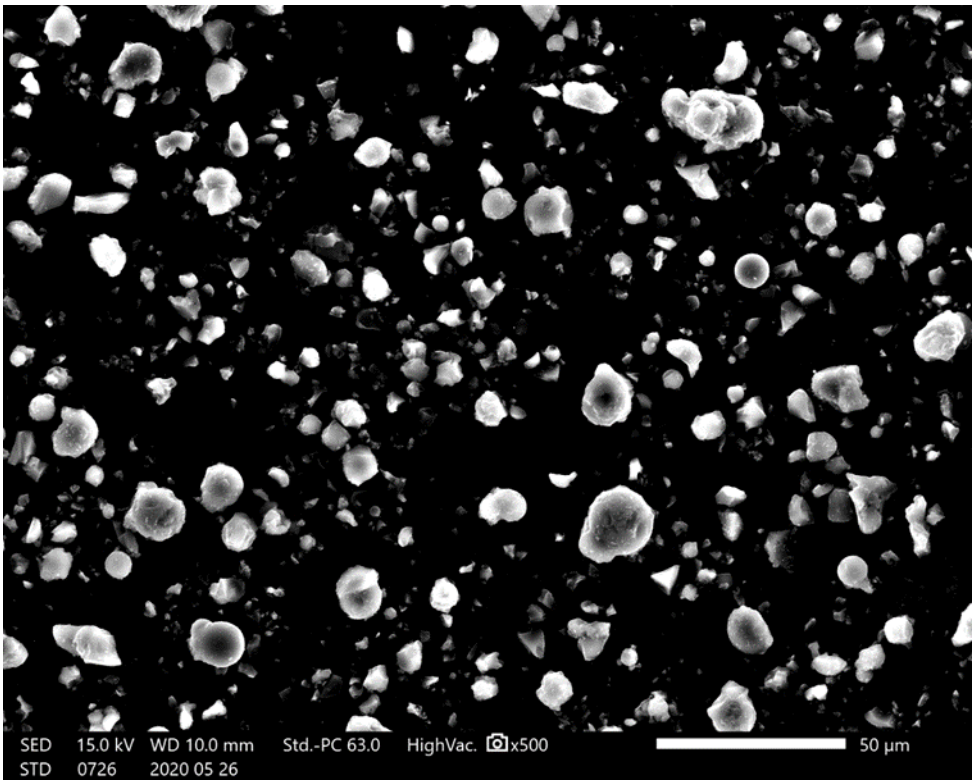
SED 15.0 kV WD 10.0 mm Std.-PC 63.0 HighVac. x500 50 μm
STD 0726 2020 05 26

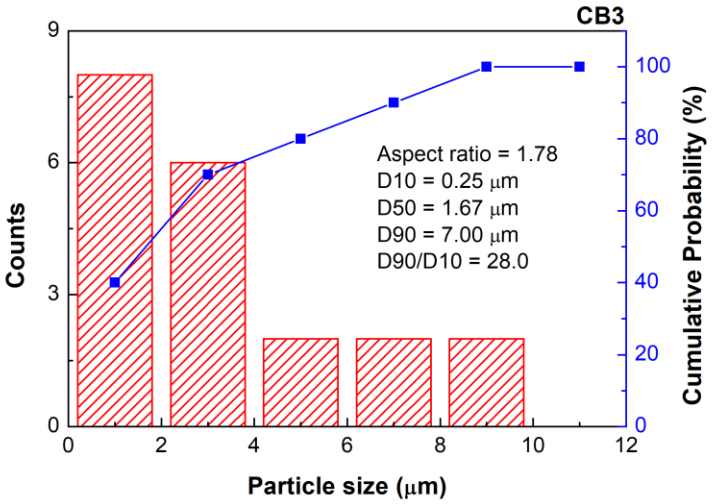
CB3
Counts
Cumulative Probability (%)
Particle size (μm)
Aspect ratio = 1.78
D10 = 0.25 μm
D50 = 1.67 μm
D90 = 7.00 μm
D90/D10 = 28.0
0
3
6
9
0
20
40
60
80
100
0
2
4
6
8
10
12

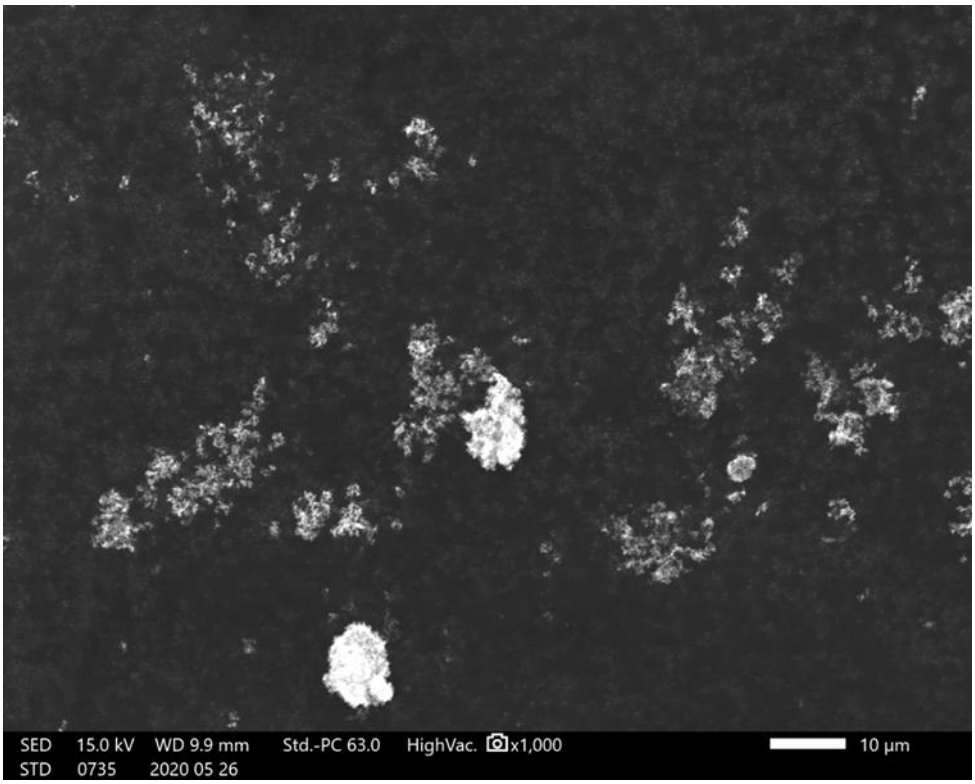
SED 15.0 kV WD 9.9 mm Std.-PC 63.0 HighVac. x1,000 10 μm
STD 0735 2020 05 26

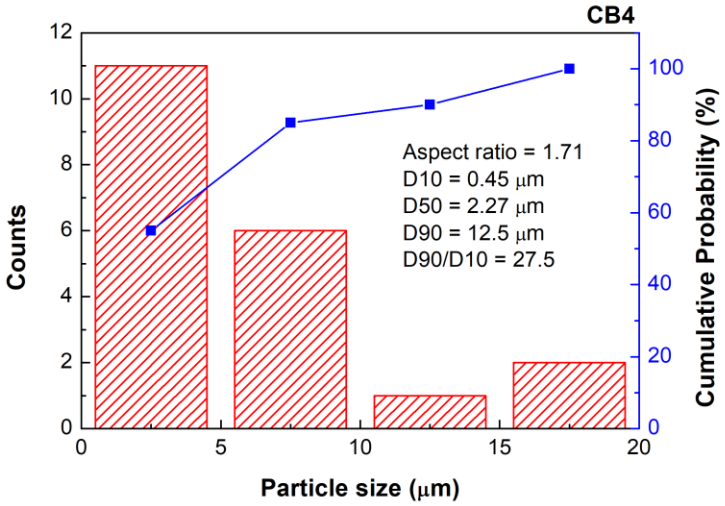
CB4
Counts
Cumulative Probability (%)
Particle size (μm)
Aspect ratio = 1.71
D10 = 0.45 μm
D50 = 2.27 μm
D90 = 12.5 μm
D90/D10 = 27.5
0
2
4
6
8
10
12
0
20
40
60
80
100
0
5
10
15
20

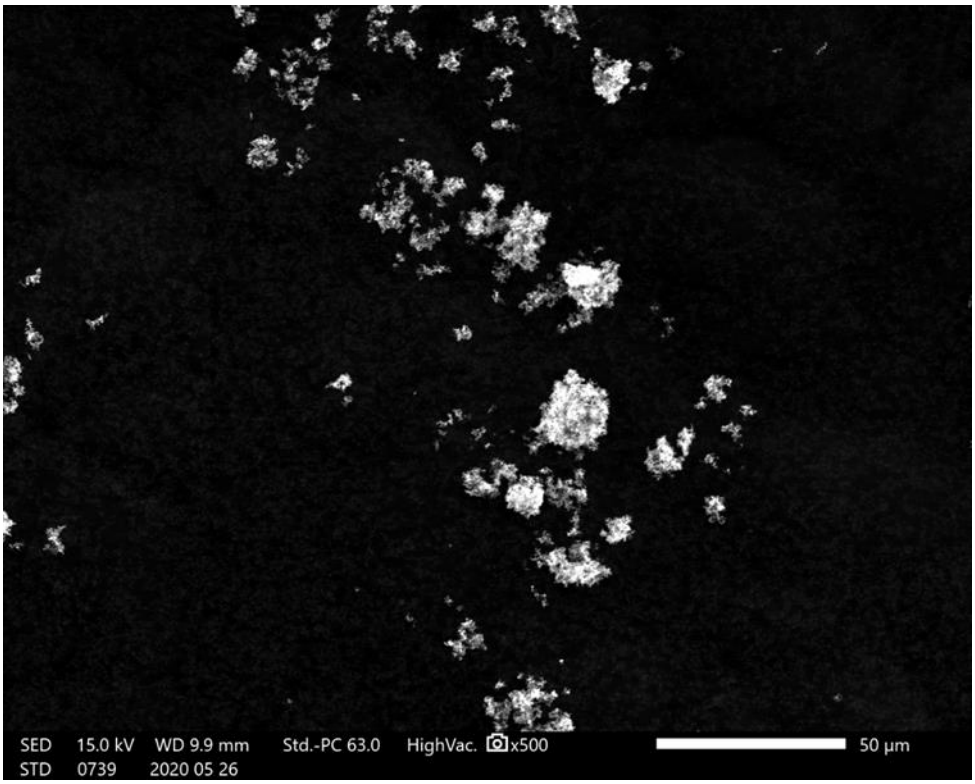
SED 15.0 kV WD 9.9 mm Std.-PC 63.0 HighVac. x500 50 μm
STD 0739 2020 05 26

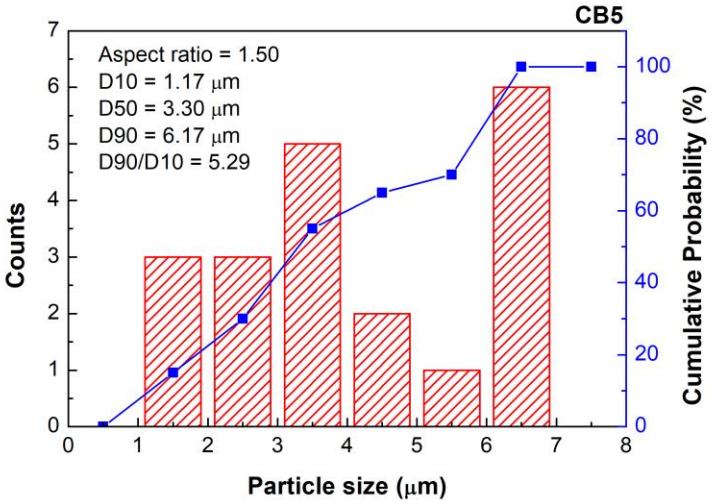
CB5
Aspect ratio = 1.50
D10 = 1.17 μm
D50 = 3.30 μm
D90 = 6.17 μm
D90/D10 = 5.29
Counts
Cumulative Probability (%)
Particle size (μm)

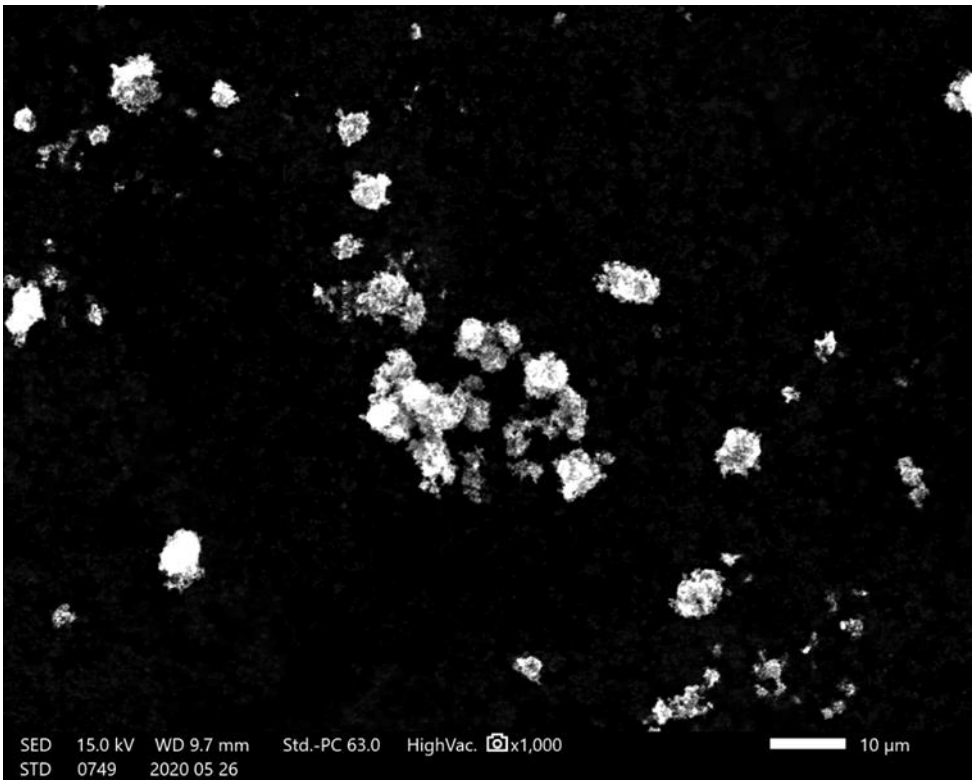
SED 15.0 kV WD 9.7 mm Std.-PC 63.0 HighVac. x1,000
STD 0749 2020 05 26
10 μm

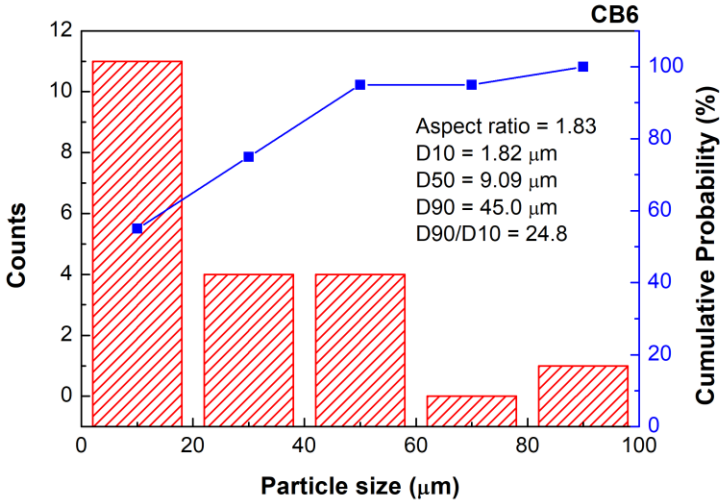
CB6
Aspect ratio = 1.83
D10 = 1.82 μm
D50 = 9.09 μm
D90 = 45.0 μm
D90/D10 = 24.8
Counts
Cumulative Probability (%)
Particle size (μm)
0
2
4
6
8
10
12
0
20
40
60
80
100
0
20
40
60
80
100

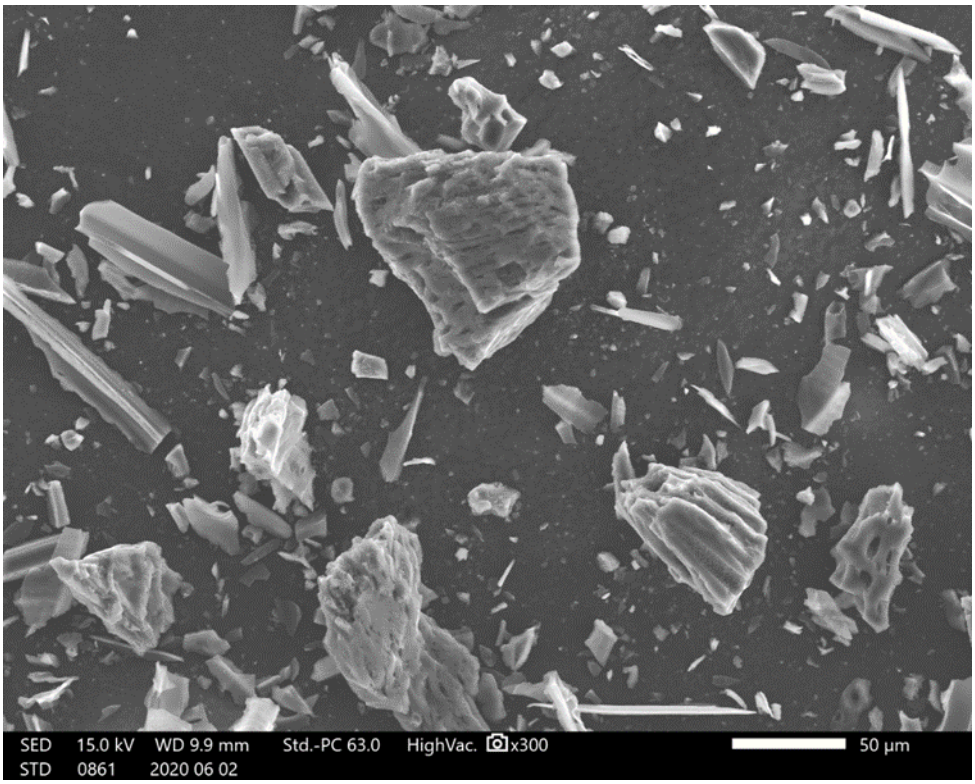
SED 15.0 kV WD 9.9 mm Std.-PC 63.0 HighVac. x300 50 μm
STD 0861 2020 06 02

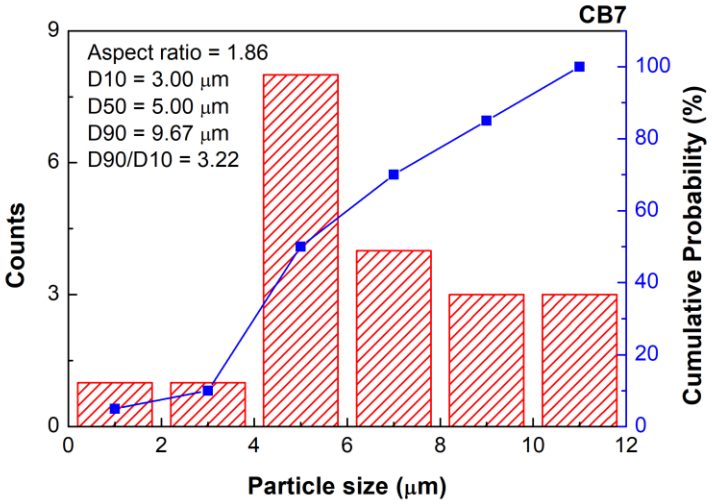
CB7
Aspect ratio = 1.86
D10 = 3.00 μm
D50 = 5.00 μm
D90 = 9.67 μm
D90/D10 = 3.22
Counts
Cumulative Probability (%)
Particle size (μm)
0
3
6
9
0
20
40
60
80
100
0
2
4
6
8
10
12

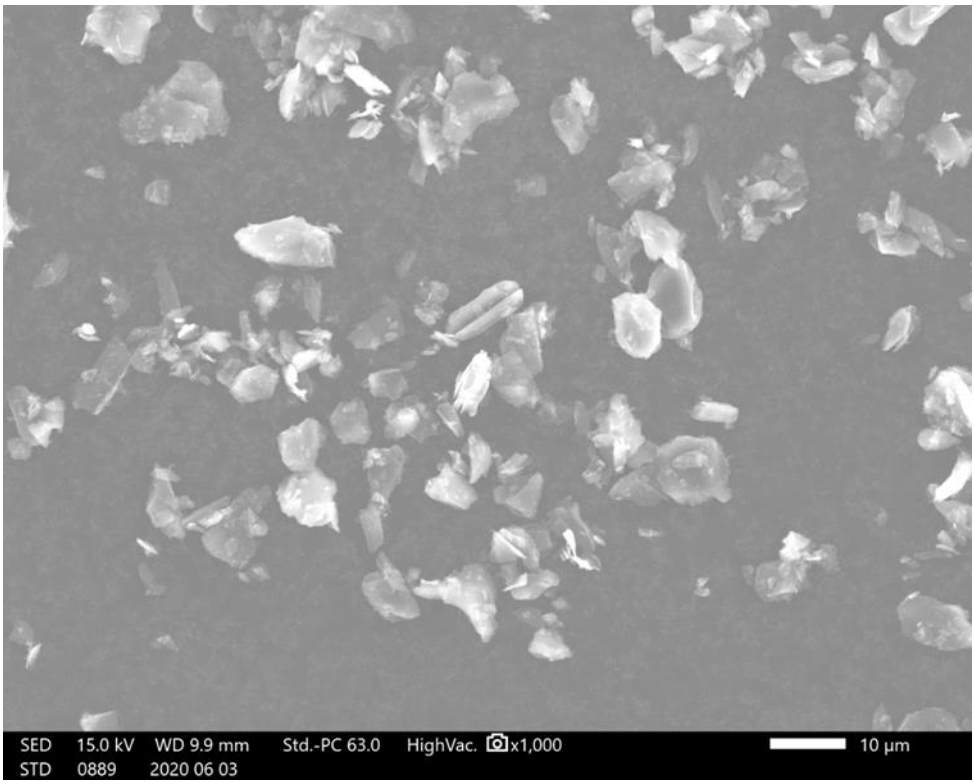
SED 15.0 kV WD 9.9 mm Std.-PC 63.0 HighVac. x1,000 10 μm
STD 0889 2020 06 03

(e) BET

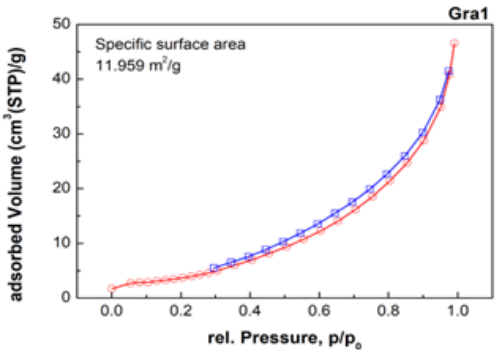
Gra1
Specific surface area
11.959 m²/g
adsorbed Volume (cm³(STP)/g)
rel. Pressure, p/p₀

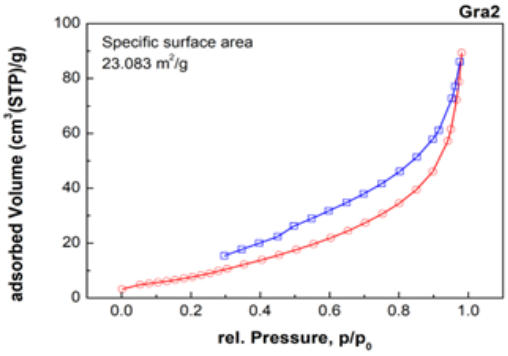
Gra2
Specific surface area
23.083 m²/g
adsorbed Volume (cm³(STP)/g)
rel. Pressure, p/p₀

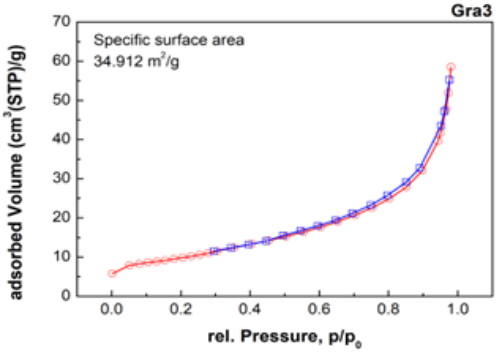
Gra3
Specific surface area
34.912 m²/g
adsorbed Volume (cm³(STP)/g)
rel. Pressure, p/p₀

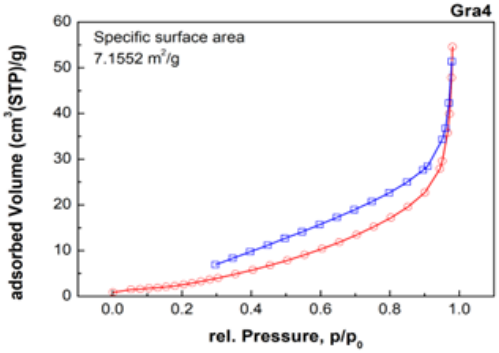
Gra4
Specific surface area
7.1552 m²/g
adsorbed Volume (cm³(STP)/g)
rel. Pressure, p/p₀

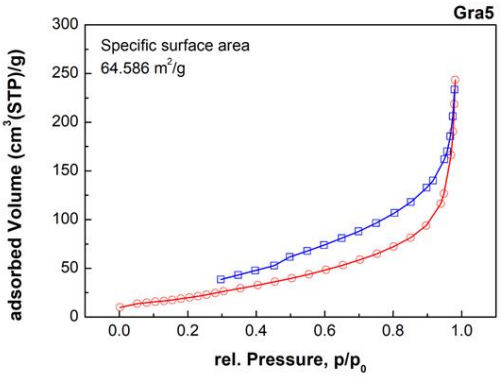
Gra5
Specific surface area
64.586 m²/g
adsorbed Volume (cm³(STP)/g)
rel. Pressure, p/p₀

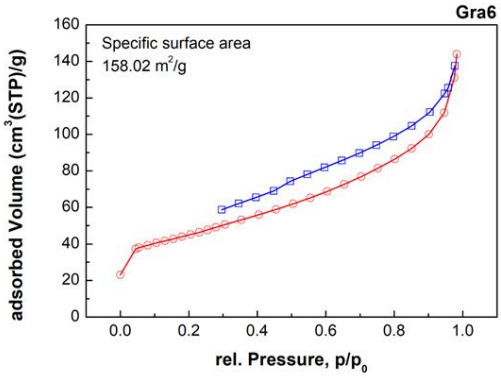
Gra6
Specific surface area
158.02 m²/g
adsorbed Volume (cm³(STP)/g)
rel. Pressure, p/p₀

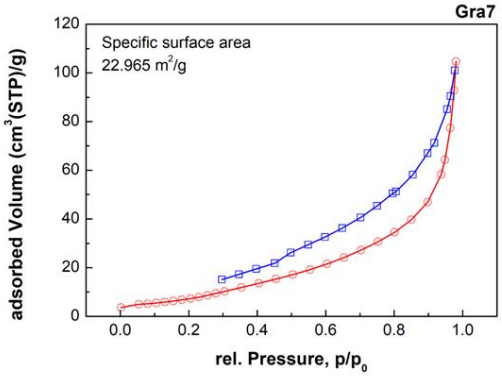
Gra7
Specific surface area
22.965 m²/g
adsorbed Volume (cm³(STP)/g)
rel. Pressure, p/p₀

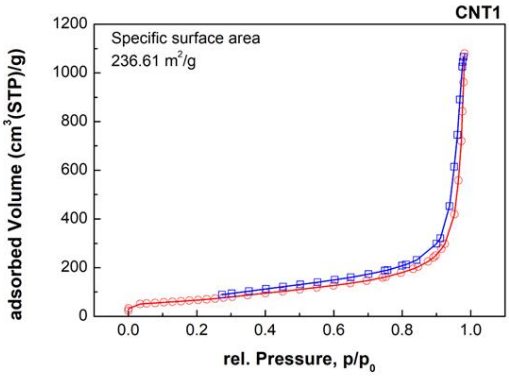
CNT1
Specific surface area
236.61 m²/g
adsorbed Volume (cm³(STP)/g)
rel. Pressure, p/p₀

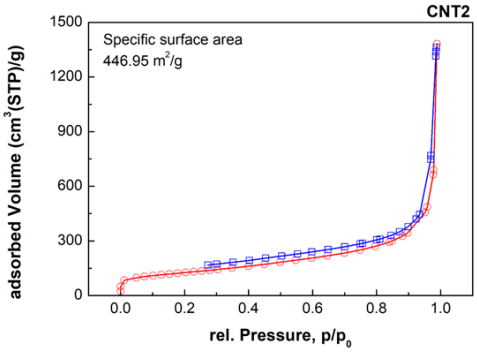
CNT2
Specific surface area
446.95 m²/g
adsorbed Volume (cm³(STP)/g)
rel. Pressure, p/p₀

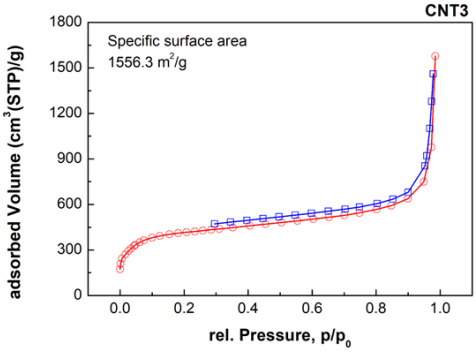
CNT3
Specific surface area
1556.3 m²/g
adsorbed Volume (cm³(STP)/g)
rel. Pressure, p/p₀

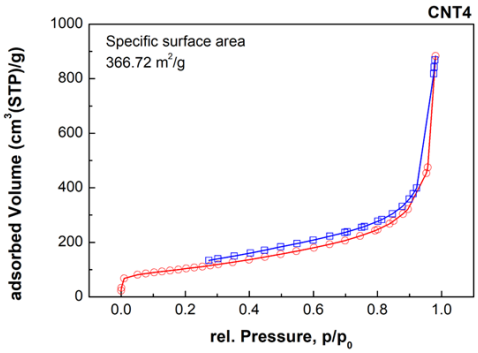
CNT4
Specific surface area
366.72 m²/g
adsorbed Volume (cm³(STP)/g)
rel. Pressure, p/p₀

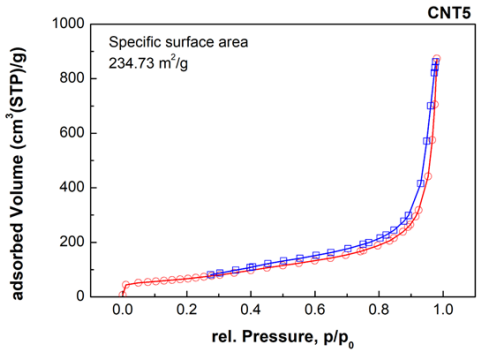
CNT5
Specific surface area
234.73 m²/g
adsorbed Volume (cm³(STP)/g)
rel. Pressure, p/p₀

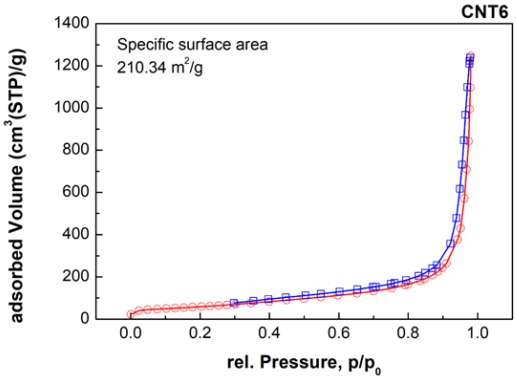
CNT6
Specific surface area
210.34 m²/g
adsorbed Volume (cm³(STP)/g)
rel. Pressure, p/p₀

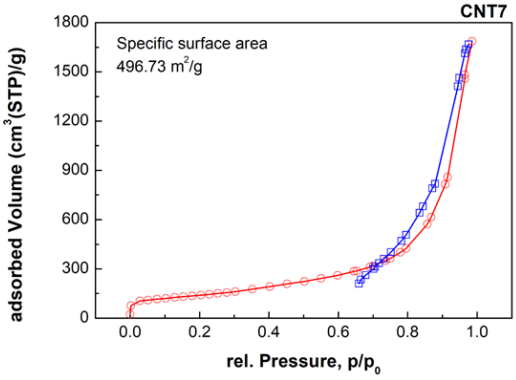
CNT7
Specific surface area
496.73 m²/g
adsorbed Volume (cm³(STP)/g)
rel. Pressure, p/p₀

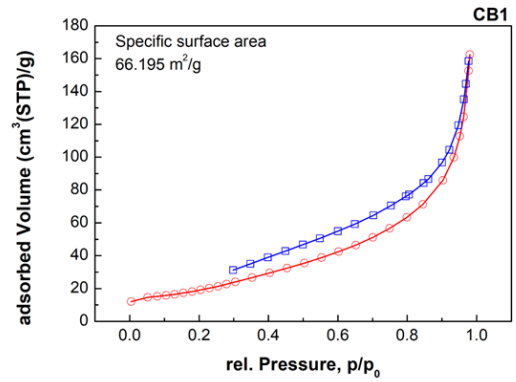
CB1
Specific surface area
66.195 m²/g
adsorbed Volume (cm³(STP)/g)
rel. Pressure, p/p₀

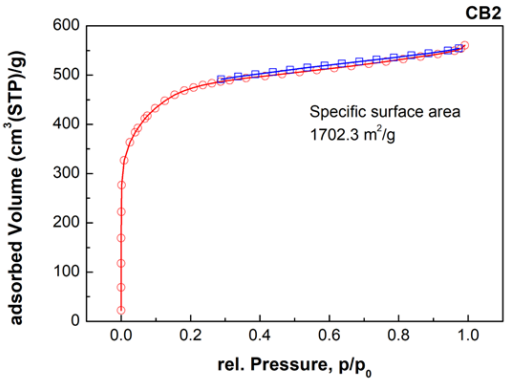
CB2
Specific surface area
1702.3 m²/g
adsorbed Volume (cm³(STP)/g)
rel. Pressure, p/p₀

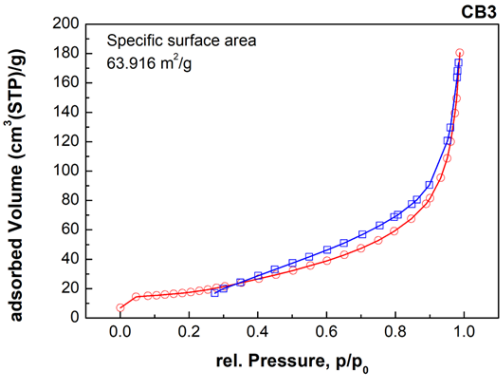
CB3
Specific surface area
63.916 m²/g
adsorbed Volume (cm³(STP)/g)
rel. Pressure, p/p₀

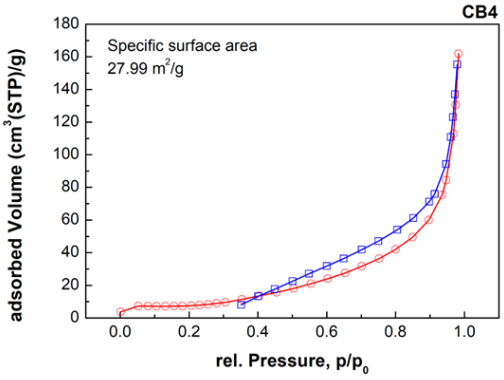
CB4
Specific surface area
27.99 m²/g
adsorbed Volume (cm³(STP)/g)
rel. Pressure, p/p₀

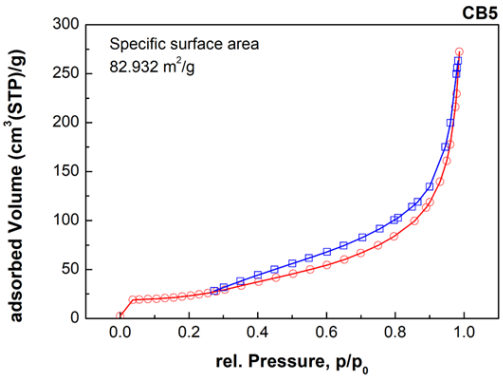
CB5
Specific surface area
82.932 m²/g
adsorbed Volume (cm³(STP)/g)
rel. Pressure, p/p₀

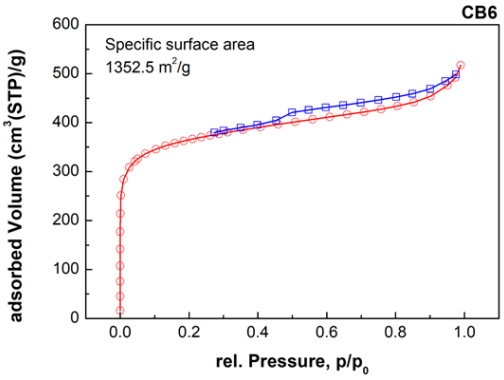
CB6
Specific surface area
1352.5 m²/g
adsorbed Volume (cm³(STP)/g)
rel. Pressure, p/p₀

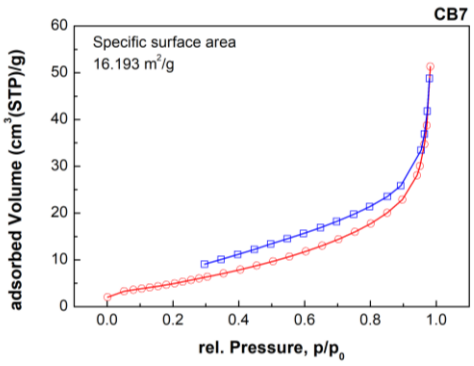
CB7
Specific surface area
16.193 m²/g
adsorbed Volume (cm³(STP)/g)
rel. Pressure, p/p₀

(f) Electrical conductivity

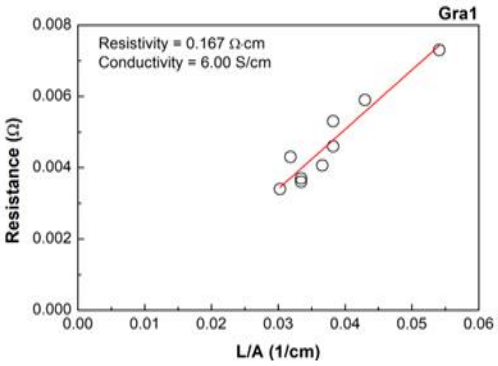

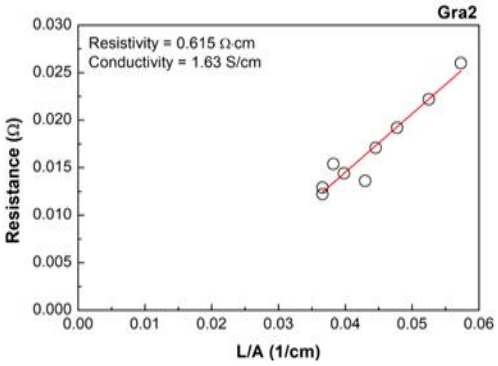

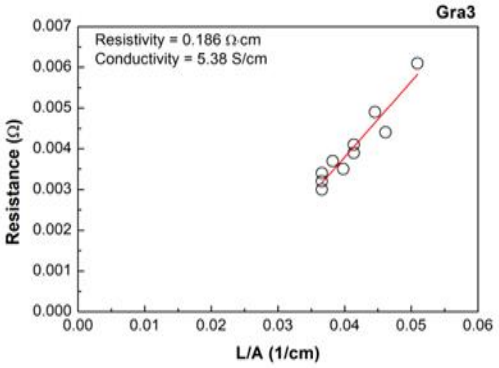

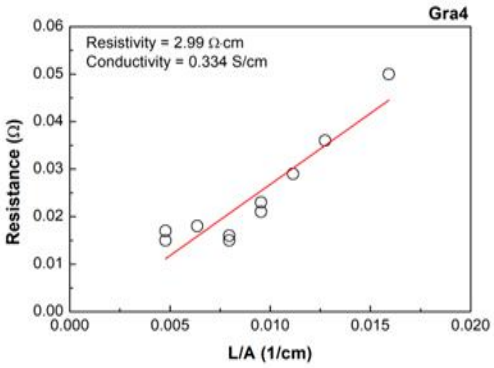

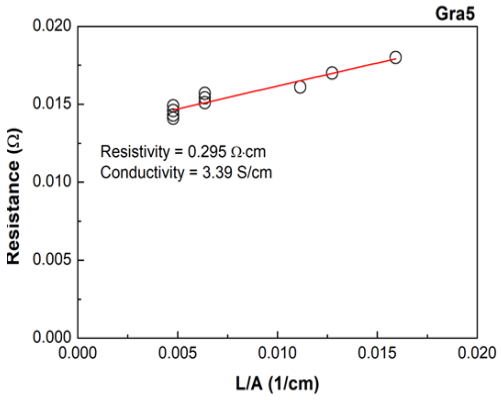
Gra5
Resistivity = 0.295 Ω·cm
Conductivity = 3.39 S/cm
Resistance (Ω)
L/A (1/cm)

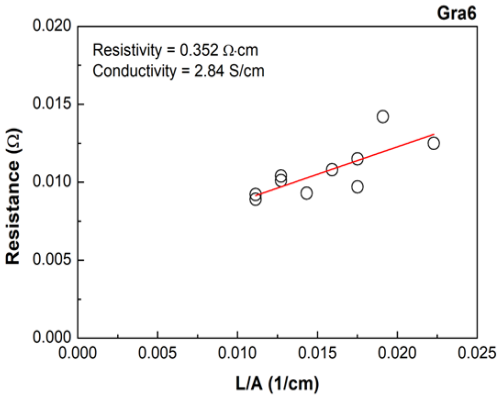
Gra6
Resistivity = 0.352 Ω·cm
Conductivity = 2.84 S/cm
Resistance (Ω)
L/A (1/cm)

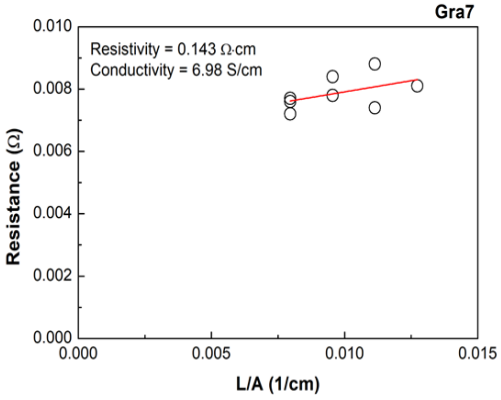
Gra7
Resistivity = 0.143 Ω·cm
Conductivity = 6.98 S/cm
Resistance (Ω)
L/A (1/cm)

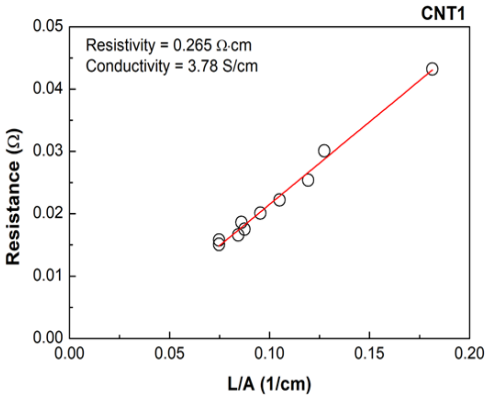
CNT1
Resistivity = 0.265 Ω·cm
Conductivity = 3.78 S/cm
Resistance (Ω)
L/A (1/cm)

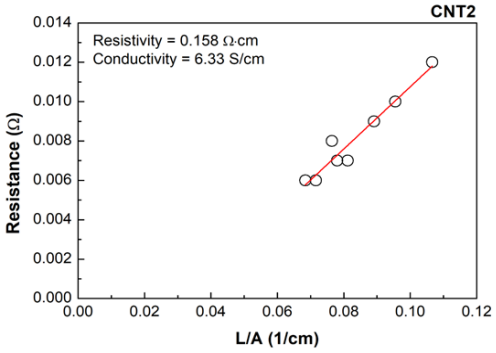
CNT2
Resistivity = 0.158 Ω·cm
Conductivity = 6.33 S/cm
Resistance (Ω)
L/A (1/cm)

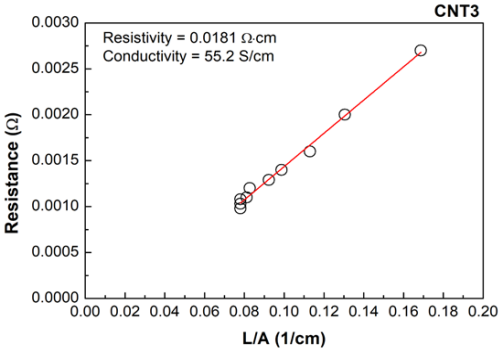
CNT3
Resistivity = 0.0181 Ω·cm
Conductivity = 55.2 S/cm
Resistance (Ω)
L/A (1/cm)

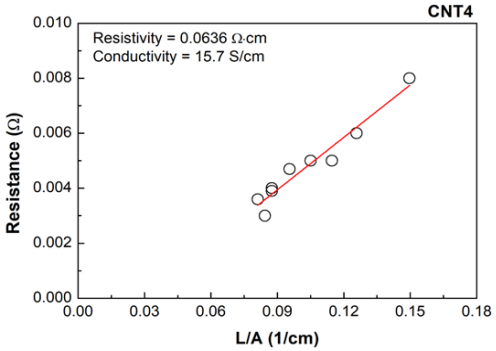
CNT4
Resistivity = 0.0636 Ω·cm
Conductivity = 15.7 S/cm
Resistance (Ω)
L/A (1/cm)

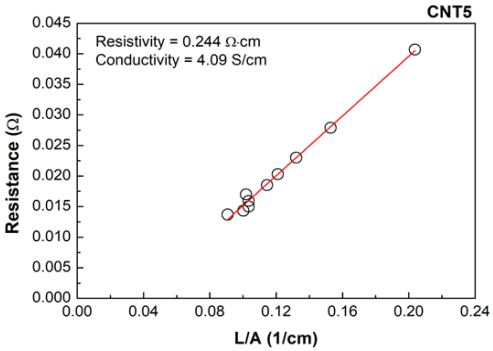
CNT5
Resistivity = 0.244 Ω·cm
Conductivity = 4.09 S/cm
Resistance (Ω)
L/A (1/cm)

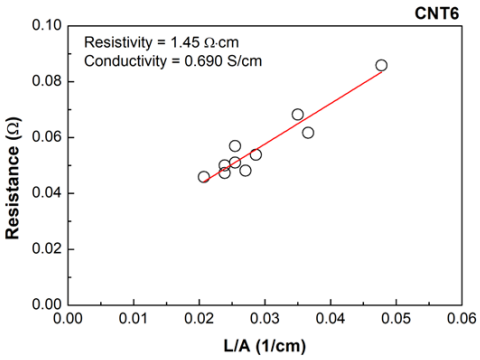
CNT6
Resistivity = 1.45 Ω·cm
Conductivity = 0.690 S/cm
Resistance (Ω)
L/A (1/cm)

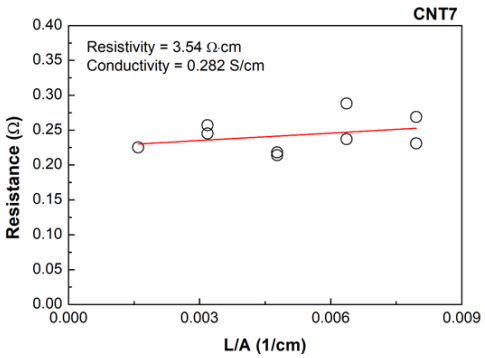
CNT7
Resistivity = 3.54 Ω·cm
Conductivity = 0.282 S/cm
Resistance (Ω)
L/A (1/cm)

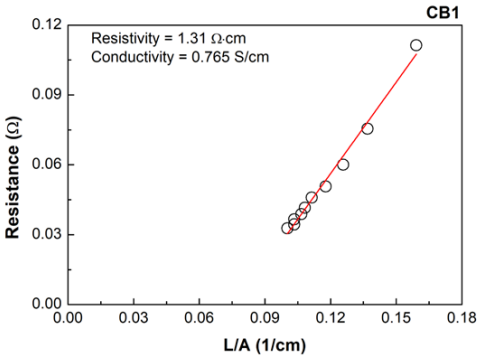
CB1
Resistivity = 1.31 Ω·cm
Conductivity = 0.765 S/cm
Resistance (Ω)
L/A (1/cm)

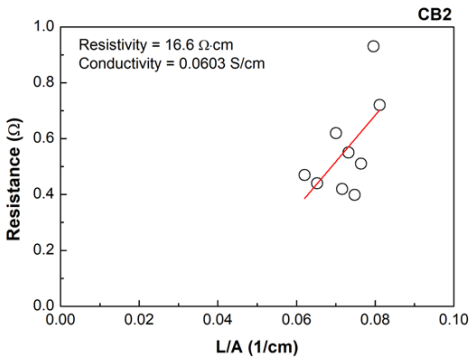
CB2
Resistivity = 16.6 Ω·cm
Conductivity = 0.0603 S/cm
Resistance (Ω)
L/A (1/cm)

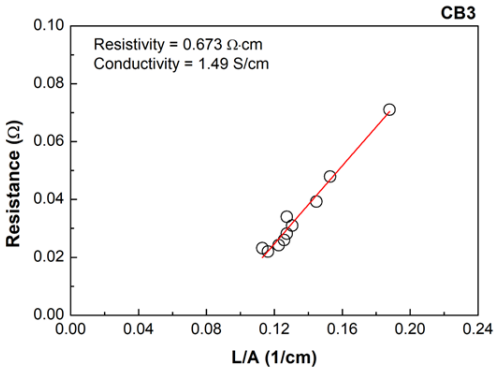
CB3
Resistivity = 0.673 Ω·cm
Conductivity = 1.49 S/cm
Resistance (Ω)
L/A (1/cm)

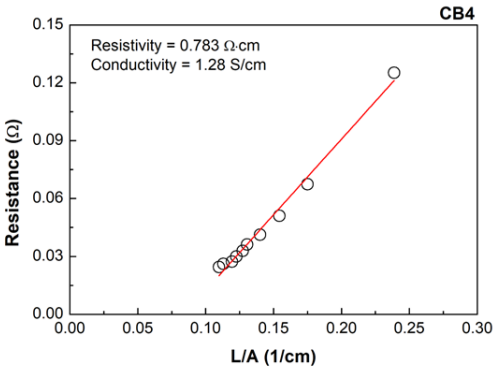
CB4
Resistivity = 0.783 Ω·cm
Conductivity = 1.28 S/cm
Resistance (Ω)
L/A (1/cm)

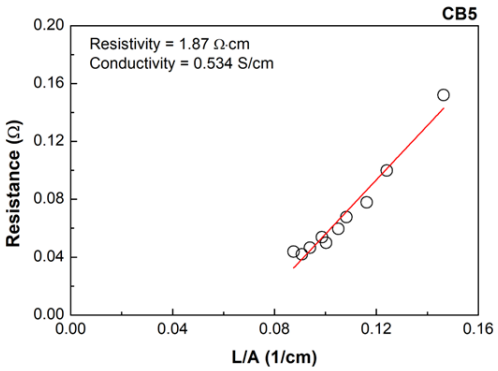
CB5
Resistivity = 1.87 Ω·cm
Conductivity = 0.534 S/cm
Resistance (Ω)
L/A (1/cm)

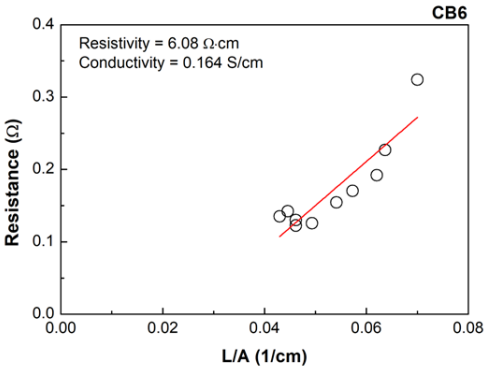
CB6
Resistivity = 6.08 Ω·cm
Conductivity = 0.164 S/cm
Resistance (Ω)
L/A (1/cm)

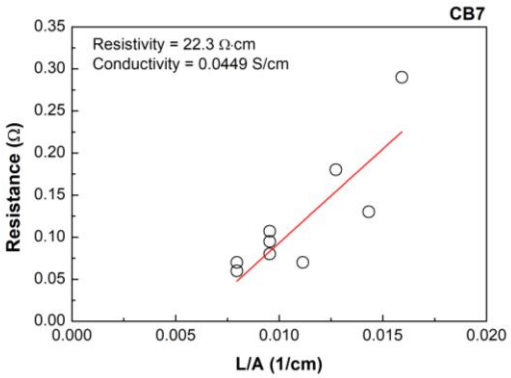

(g) Discharge capacity at 0.1 C

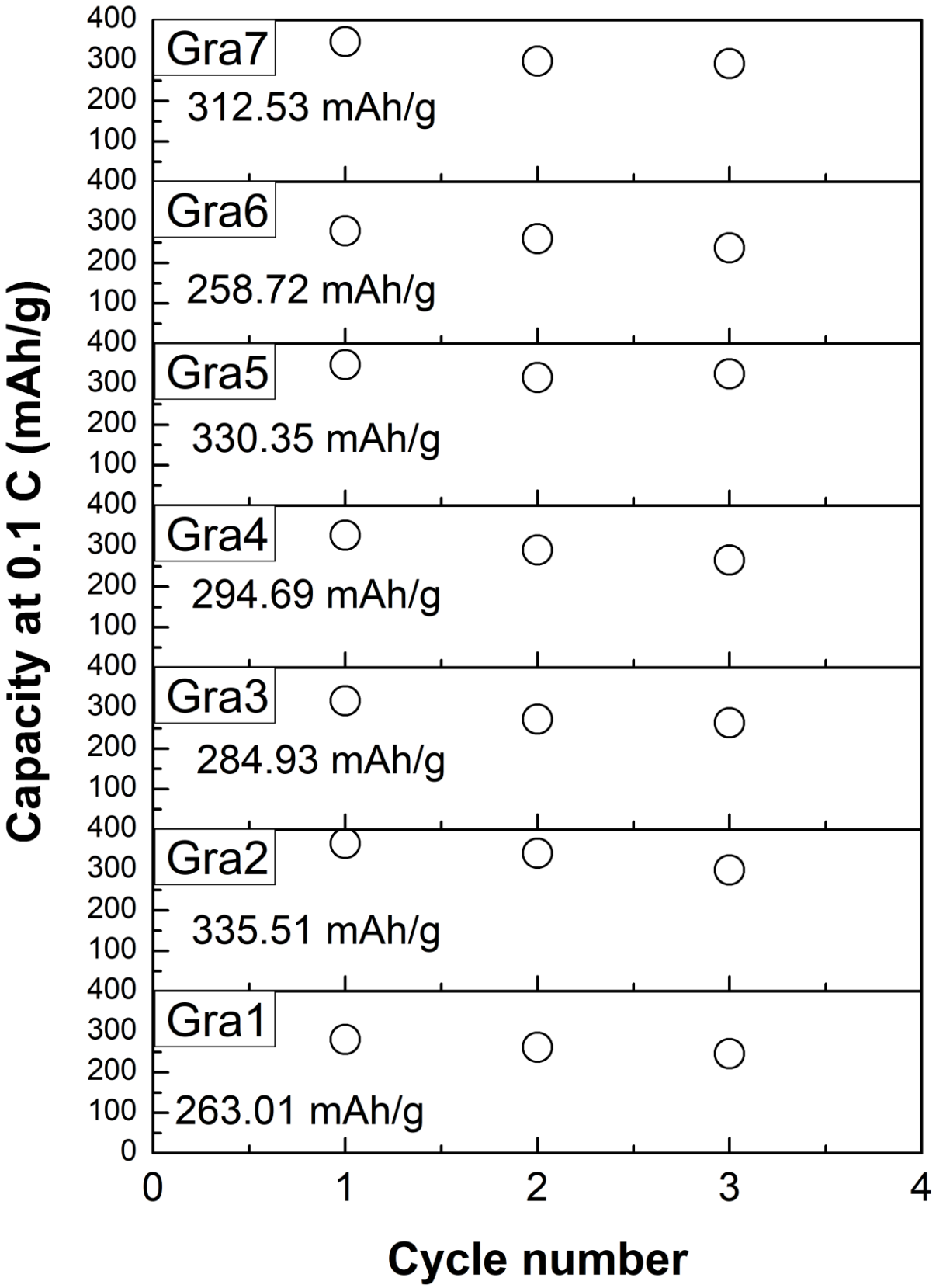
Gra7
312.53 mAh/g
Gra6
258.72 mAh/g
Gra5
330.35 mAh/g
Gra4
294.69 mAh/g
Gra3
284.93 mAh/g
Gra2
335.51 mAh/g
Gra1
263.01 mAh/g
Capacity at 0.1 C (mAh/g)
Cycle number
0
100
200
300
400
0
1
2
3
4

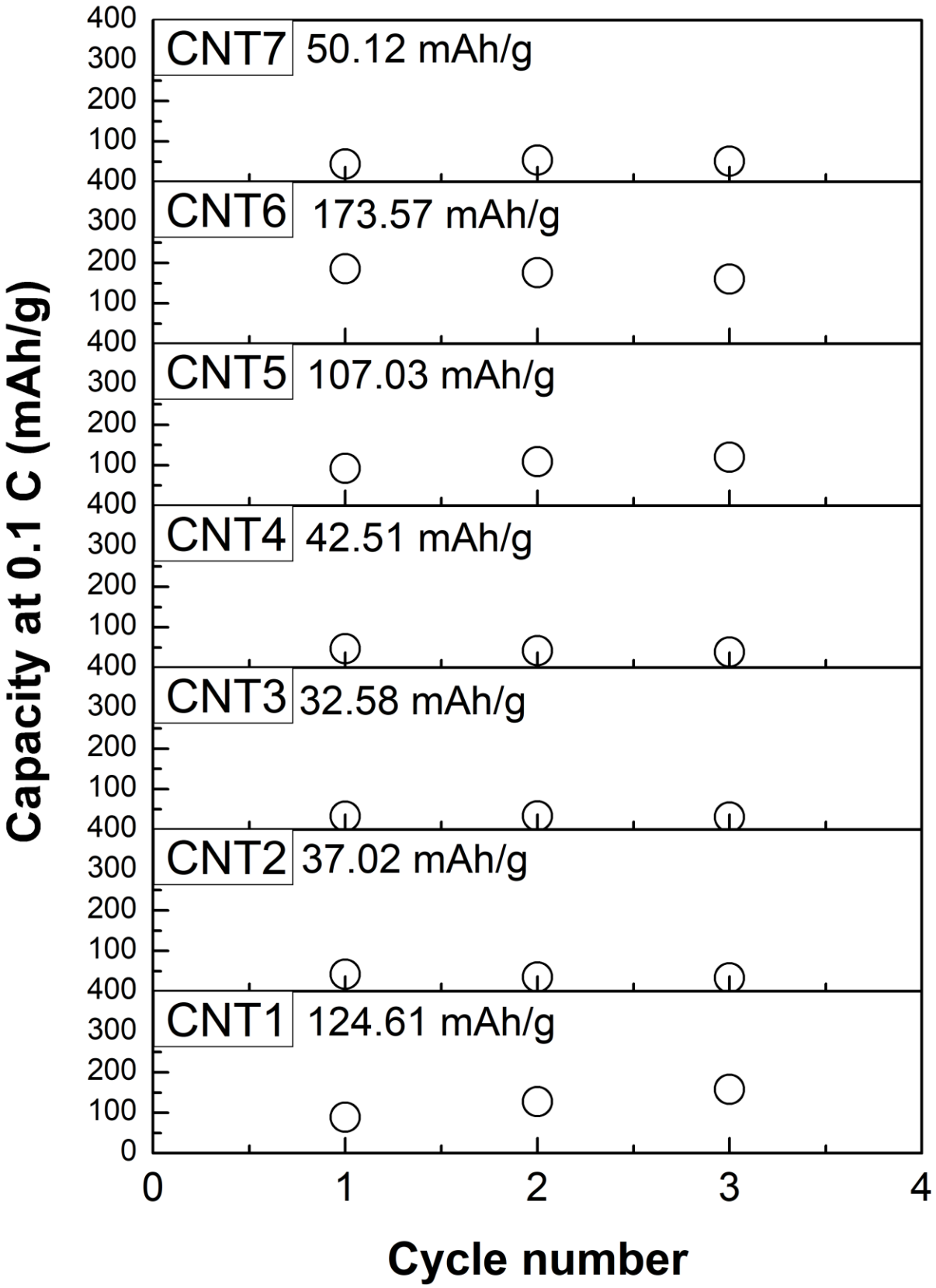
CNT7 50.12 mAh/g
CNT6 173.57 mAh/g
CNT5 107.03 mAh/g
CNT4 42.51 mAh/g
CNT3 32.58 mAh/g
CNT2 37.02 mAh/g
CNT1 124.61 mAh/g
Capacity at 0.1 C (mAh/g)
Cycle number
0
100
200
300
400
0
1
2
3
4

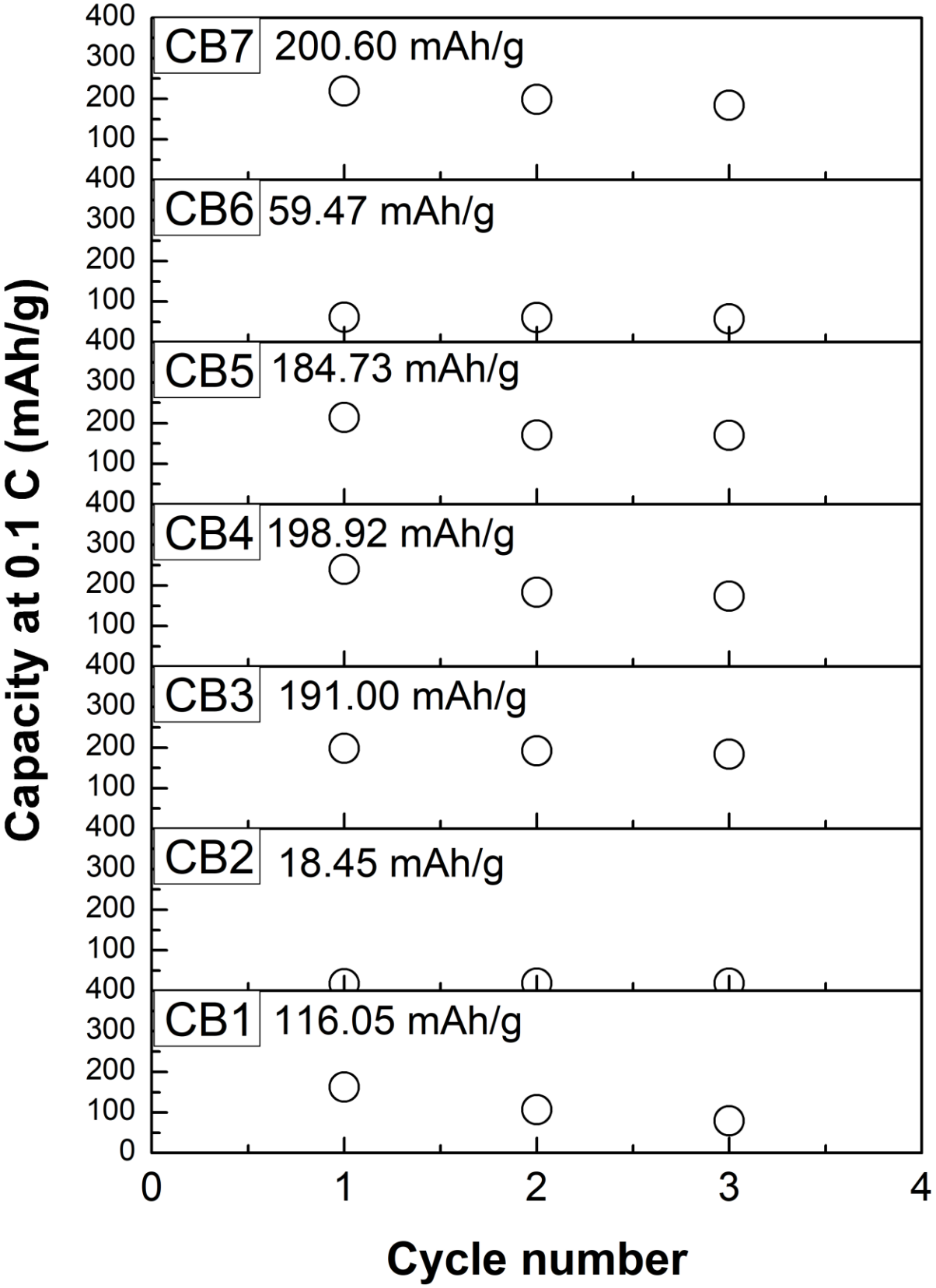
CB7 200.60 mAh/g
CB6 59.47 mAh/g
CB5 184.73 mAh/g
CB4 198.92 mAh/g
CB3 191.00 mAh/g
CB2 18.45 mAh/g
CB1 116.05 mAh/g
Capacity at 0.1 C (mAh/g)
Cycle number
0
100
200
300
400
0
1
2
3
4

Figure A 4.2 Correlation graphs between each descriptor (total 105)

(a) To d002

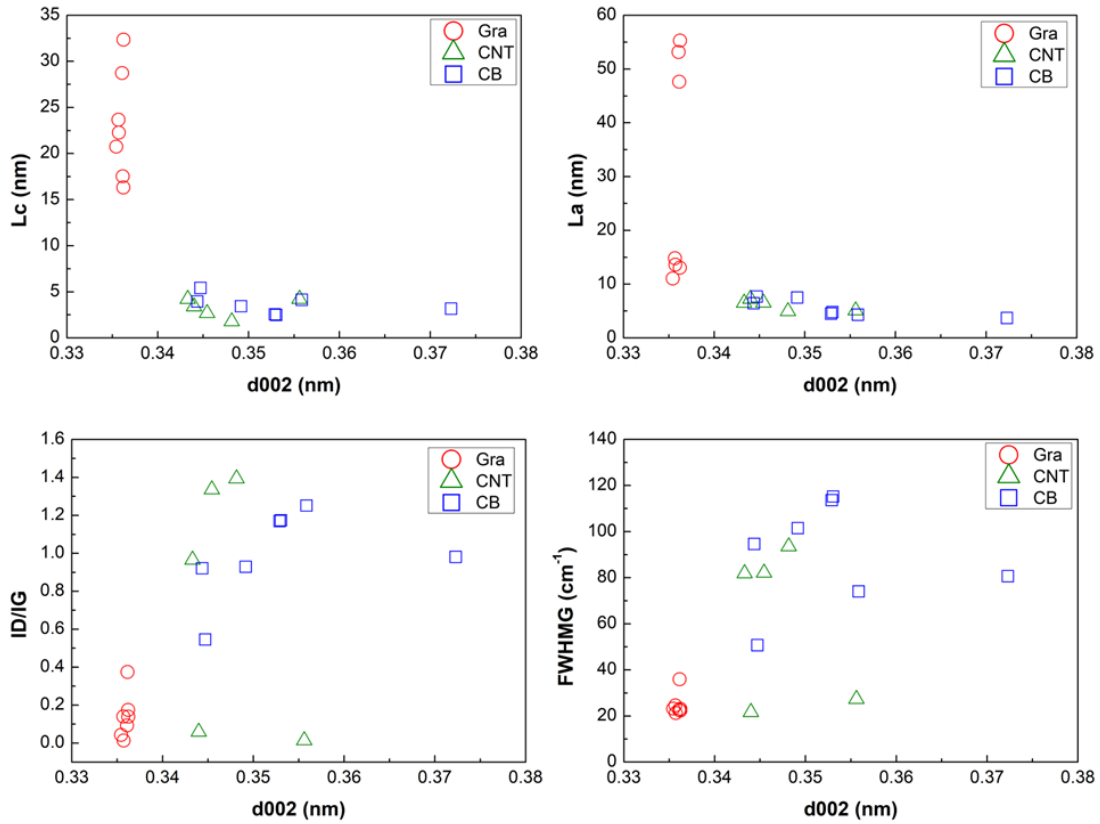

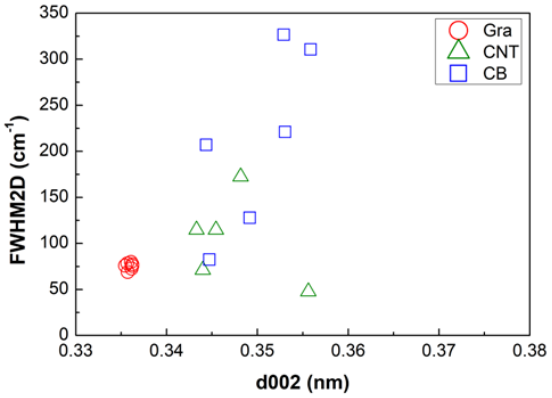
FWHM2D (cm^{-1})
d002 (nm)
Gra
CNT
CB

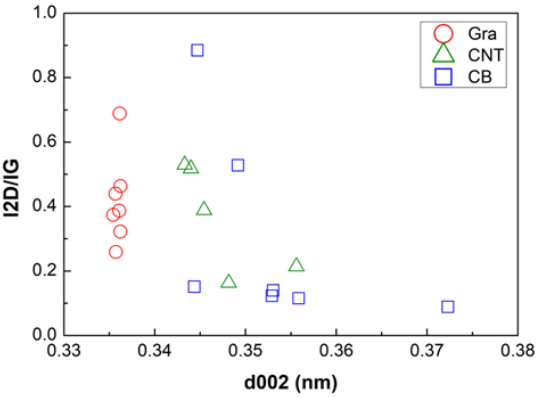
I2D/IG
d002 (nm)
Gra
CNT
CB

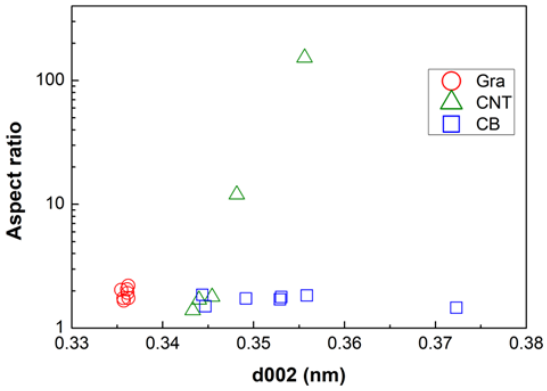
Aspect ratio
d002 (nm)
Gra
CNT
CB

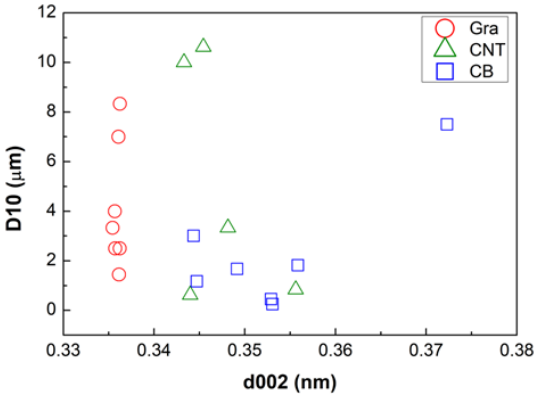
D10 (μm)
d002 (nm)
Gra
CNT
CB

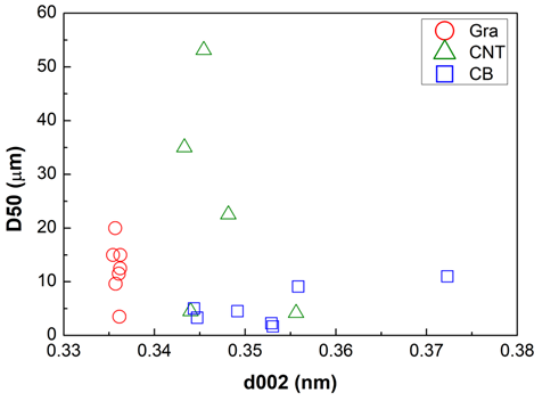
D50 (μm)
d002 (nm)
Gra
CNT
CB

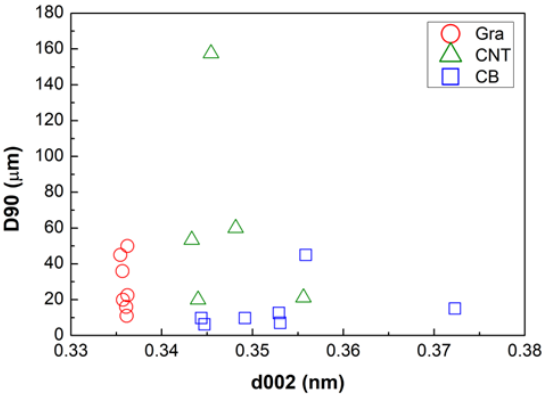
D90 (μm)
d002 (nm)
Gra
CNT
CB

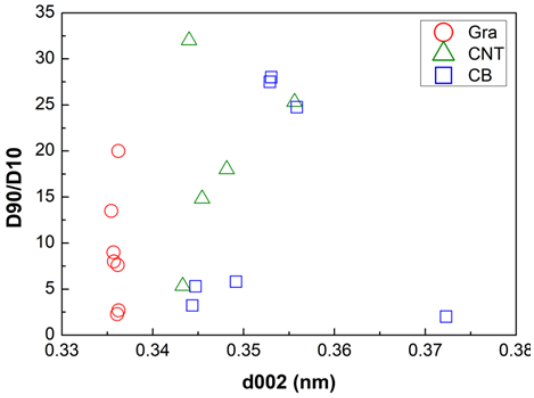
D90/D10
d002 (nm)
Gra
CNT
CB

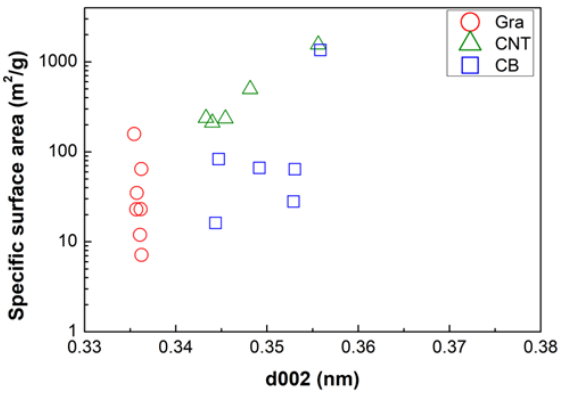
Specific surface area (m^2/g)
d002 (nm)
Gra
CNT
CB

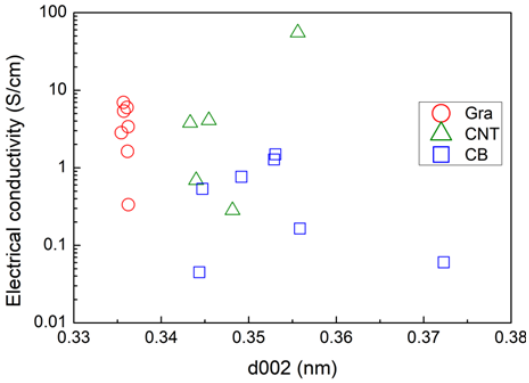
Electrical conductivity (S/cm)
100
10
1
0.1
0.01
0.33
0.34
0.35
0.36
0.37
0.38
d002 (nm)
Gra
CNT
CB

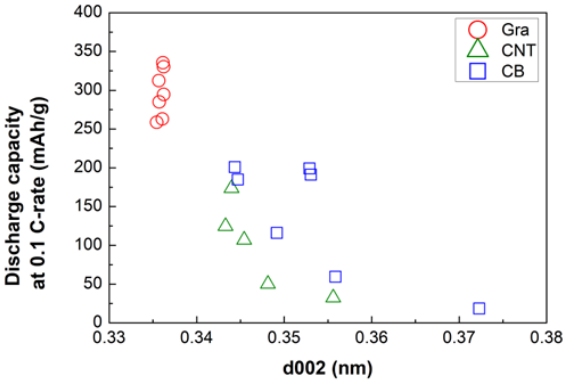
Discharge capacity at 0.1 C-rate (mAh/g)
400
350
300
250
200
150
100
50
0
0.33
0.34
0.35
0.36
0.37
0.38
d002 (nm)
Gra
CNT
CB

(b) To Lc

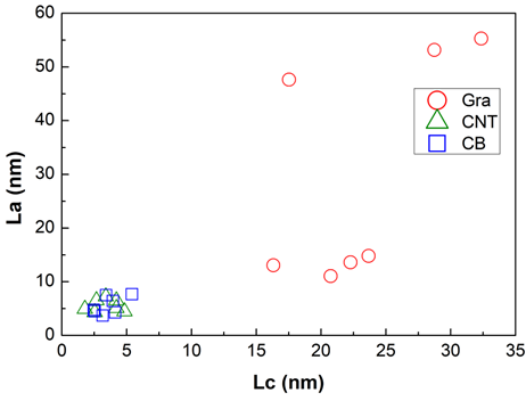
La (nm)
Lc (nm)
Gra
CNT
CB

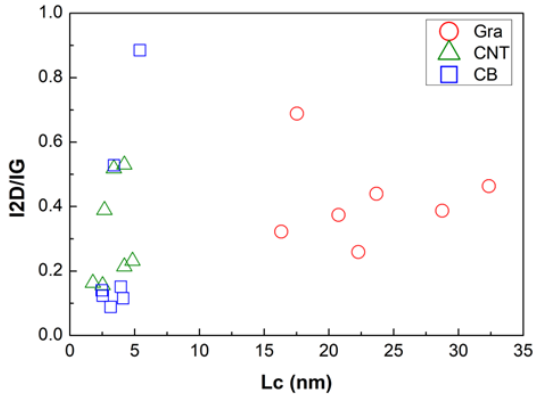
I2D/IG
Lc (nm)
Gra
CNT
CB

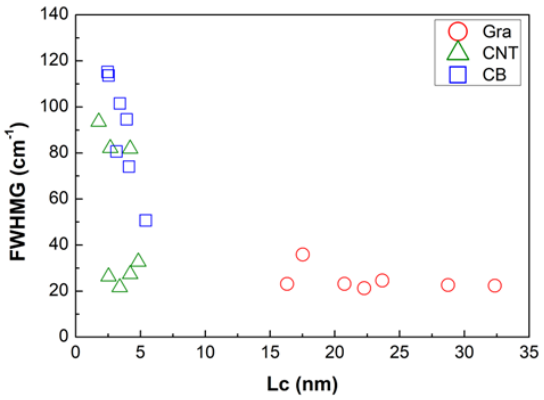
FWHMG (cm-1)
Lc (nm)
Gra
CNT
CB

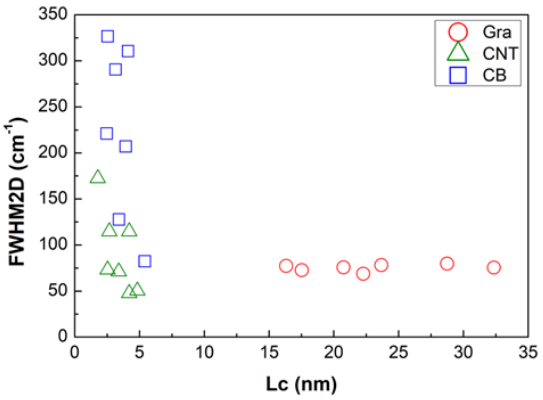
FWHM2D (cm-1)
Lc (nm)
Gra
CNT
CB

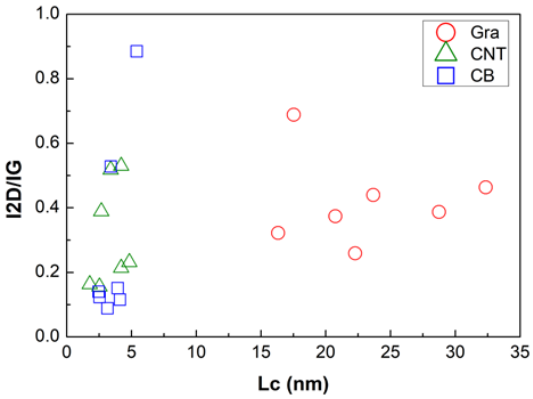
I2D/IG
Lc (nm)
Gra
CNT
CB

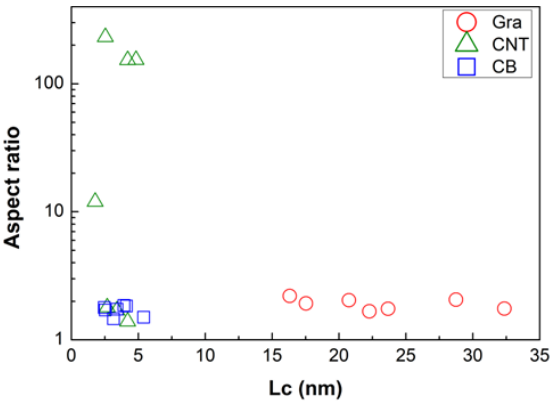
Aspect ratio
Lc (nm)
Gra
CNT
CB

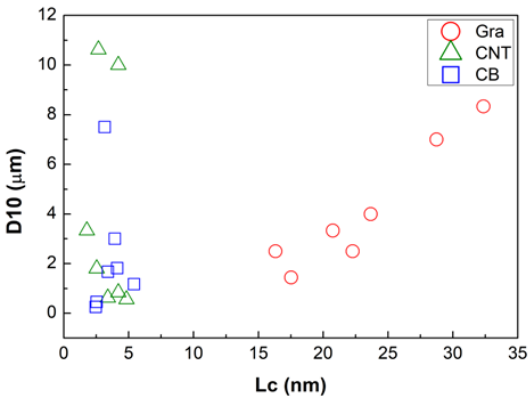
D10 (μm)
Lc (nm)
Gra
CNT
CB

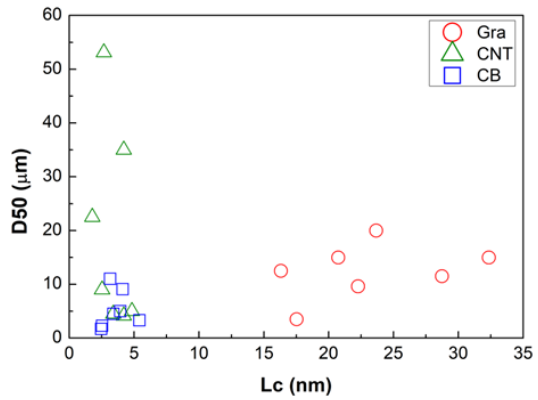
D50 (μm)
Lc (nm)
Gra
CNT
CB

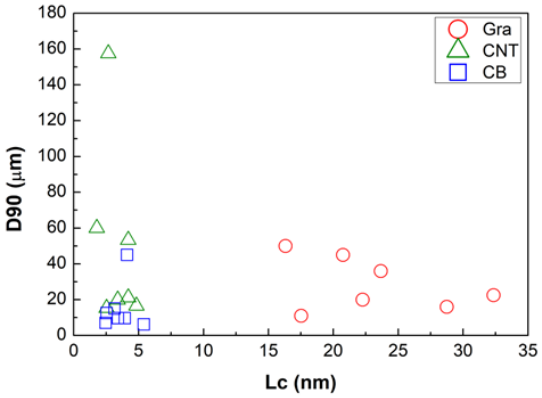
D90 (μm)
Lc (nm)
Gra
CNT
CB

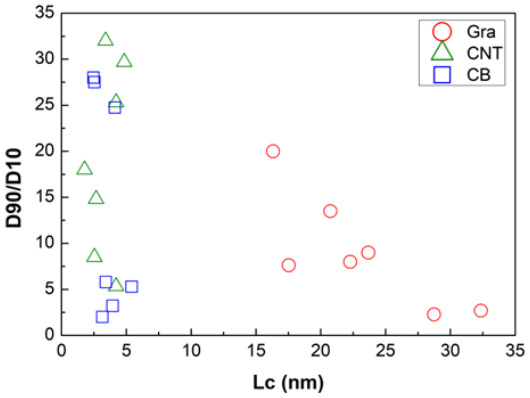
D90/D10
Lc (nm)
Gra
CNT
CB

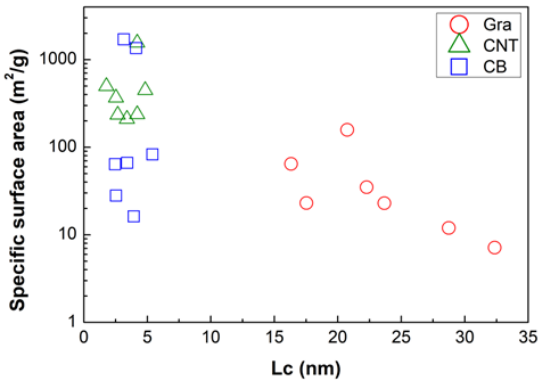
Specific surface area (m²/g)
Lc (nm)
Gra
CNT
CB

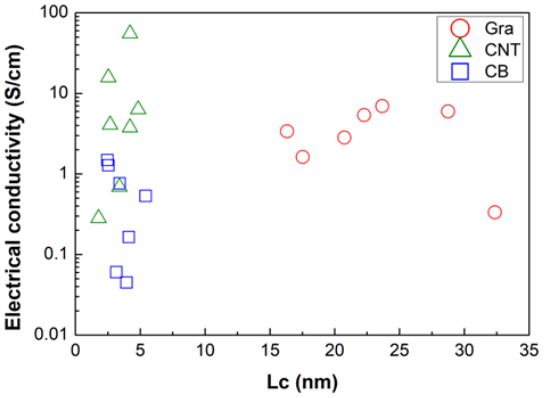
Electrical conductivity (S/cm)
Lc (nm)
Gra
CNT
CB

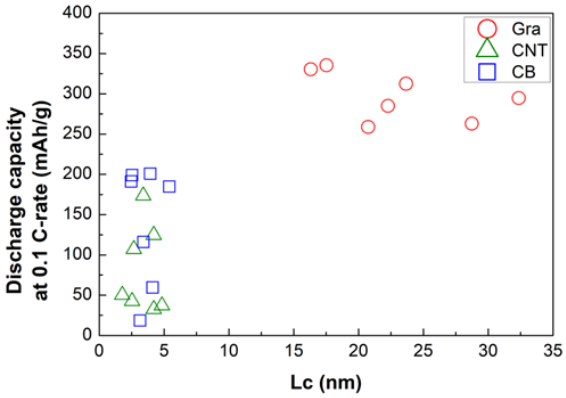
Discharge capacity at 0.1 C-rate (mAh/g)
Lc (nm)
Gra
CNT
CB

(c) To La

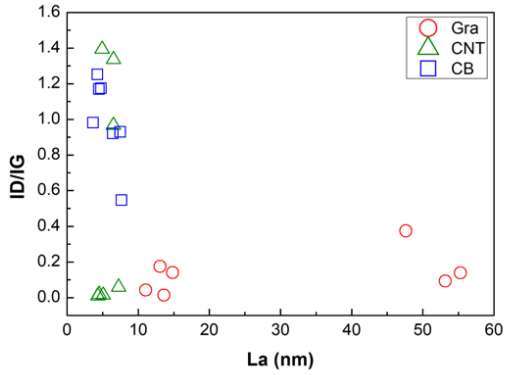
ID/IG
La (nm)
Gra
CNT
CB

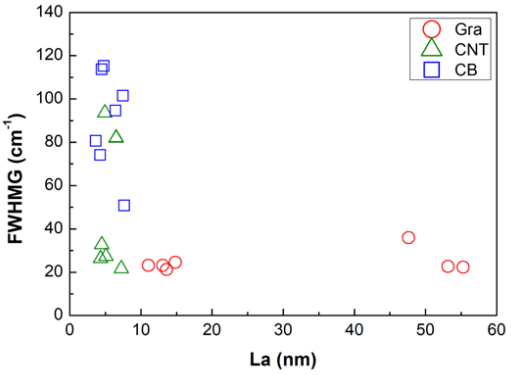
FWHMG (cm-1)
La (nm)
Gra
CNT
CB

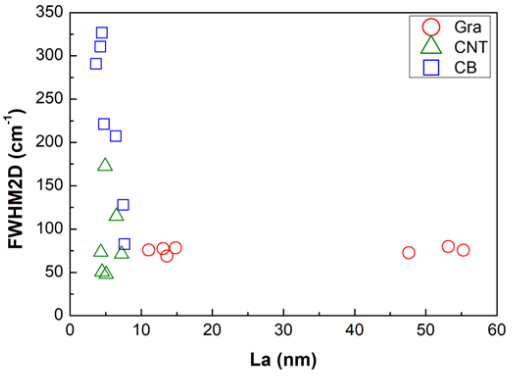
FWHM2D (cm-1)
La (nm)
Gra
CNT
CB

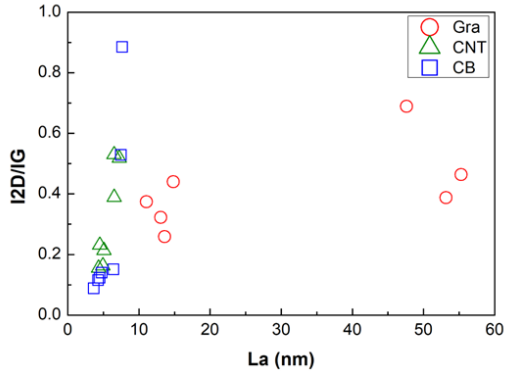
I2D/IG
La (nm)
Gra
CNT
CB

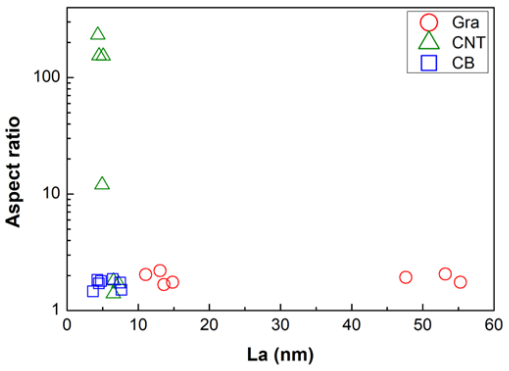
Aspect ratio
La (nm)
Gra
CNT
CB

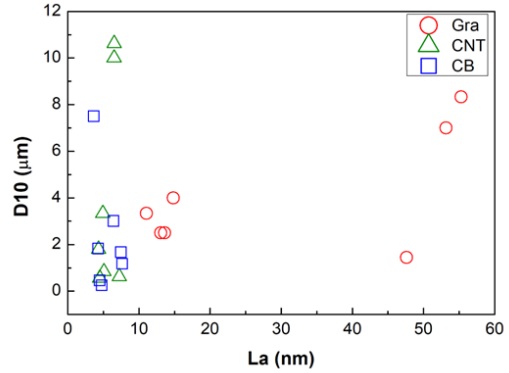
D10 (μm)
La (nm)
Gra
CNT
CB

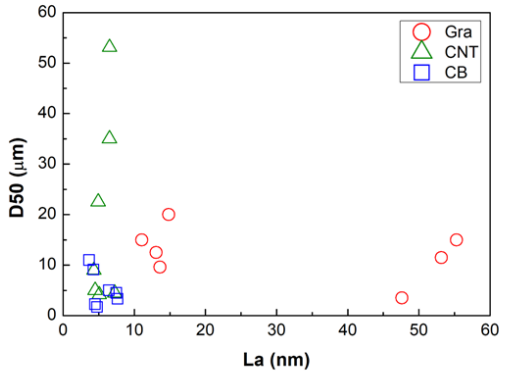
D50 (μm)
La (nm)
Gra
CNT
CB

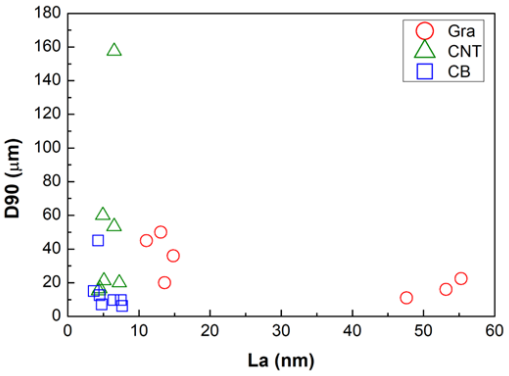
D90 (μm)
La (nm)
Gra
CNT
CB

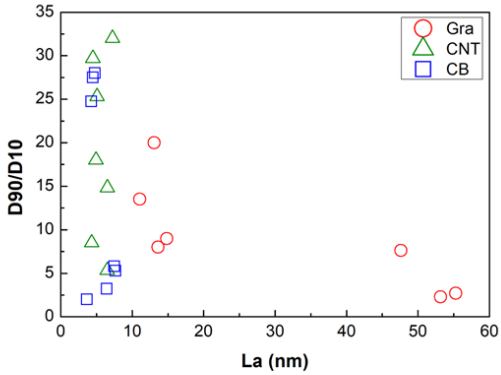
D90/D10
La (nm)
Gra
CNT
CB

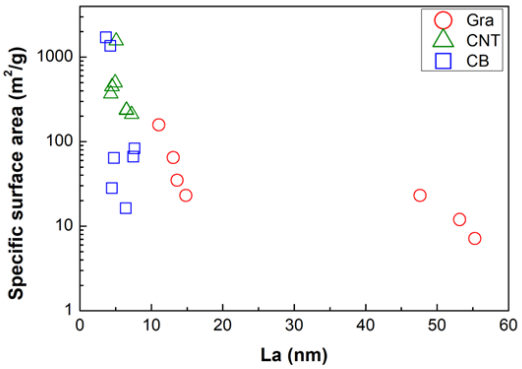
Specific surface area (m²/g)
La (nm)
Gra
CNT
CB

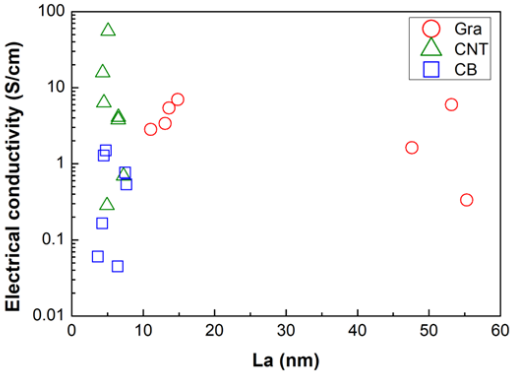
Electrical conductivity (S/cm)
La (nm)
Gra
CNT
CB

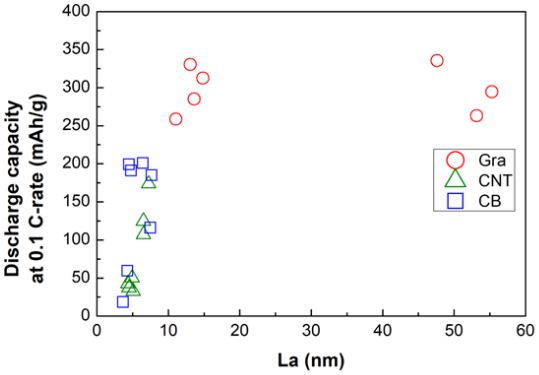
Discharge capacity at 0.1 C-rate (mAh/g)
La (nm)
Gra
CNT
CB

(d) To ID/IG

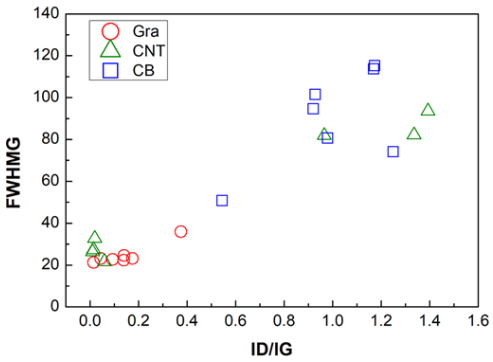
Gra
CNT
CB
FWHMG
ID/IG

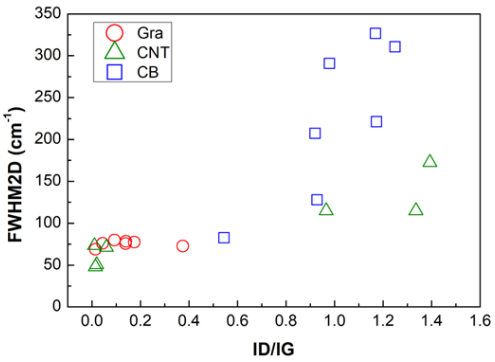
Gra
CNT
CB
FWHM2D (cm-1)
ID/IG

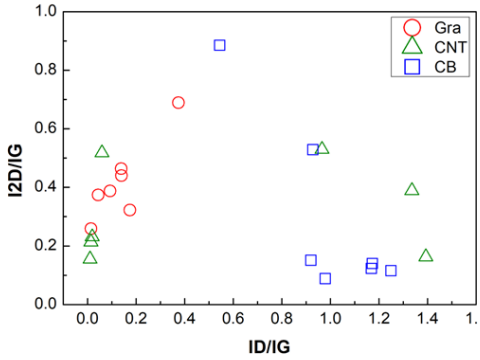
Gra
CNT
CB
I2D/IG
ID/IG

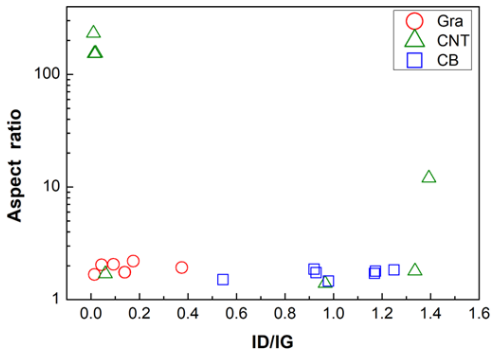
Gra
CNT
CB
Aspect ratio
ID/IG

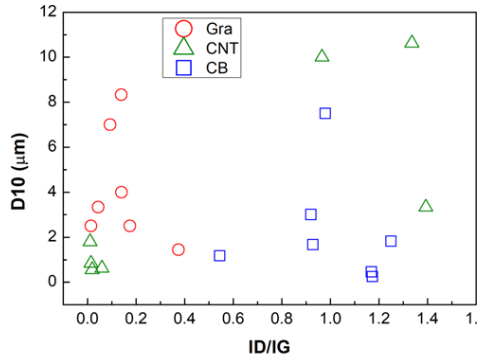
Gra
CNT
CB
D10 (μm)
ID/IG

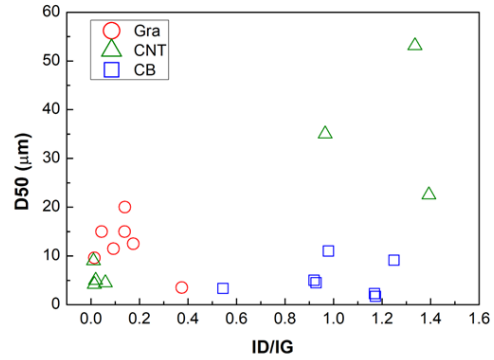
Gra
CNT
CB
D50 (μm)
ID/IG

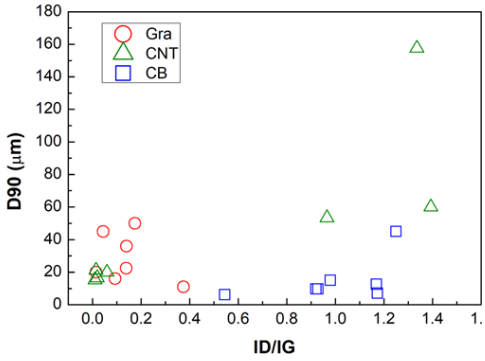
Gra
CNT
CB
D90 (μm)
ID/IG

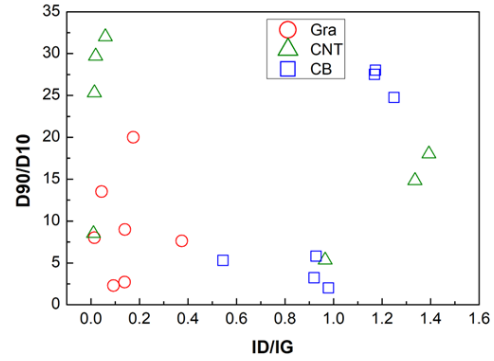
Gra
CNT
CB
D90/D10
ID/IG

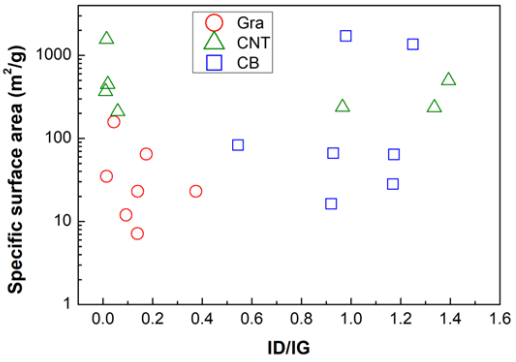
Specific surface area (m²/g)
ID/IG
Gra
CNT
CB
1
10
100
1000
0.0
0.2
0.4
0.6
0.8
1.0
1.2
1.4
1.6

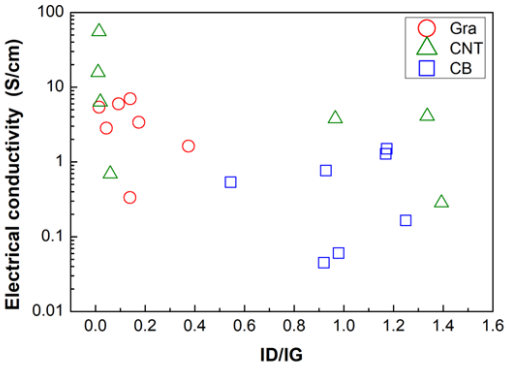
Electrical conductivity (S/cm)
ID/IG
Gra
CNT
CB
0.01
0.1
1
10
100
0.0
0.2
0.4
0.6
0.8
1.0
1.2
1.4
1.6

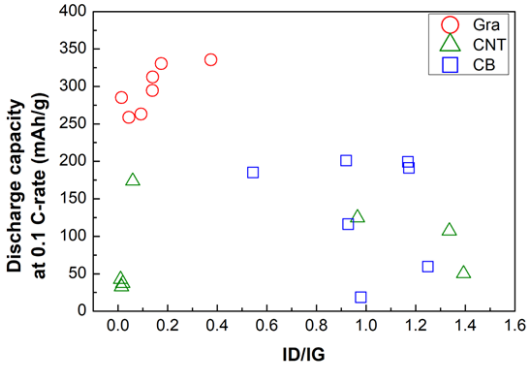
Discharge capacity
at 0.1 C-rate (mAh/g)
ID/IG
Gra
CNT
CB
0
50
100
150
200
250
300
350
400
0.0
0.2
0.4
0.6
0.8
1.0
1.2
1.4
1.6

(e) FWHMG

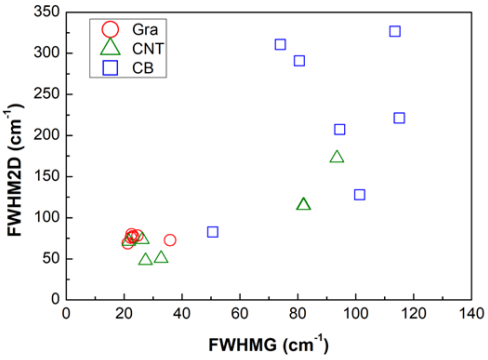
Gra
CNT
CB
FWHM2D (cm-1)
FWHMG (cm-1)

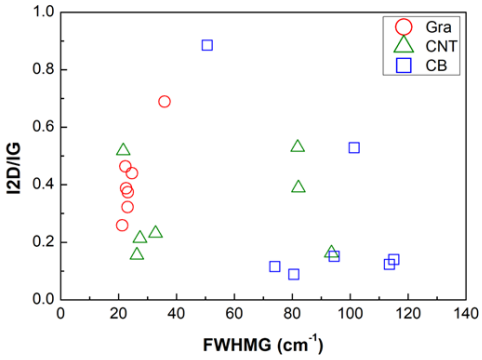
Gra
CNT
CB
I2D/IG
FWHMG (cm-1)

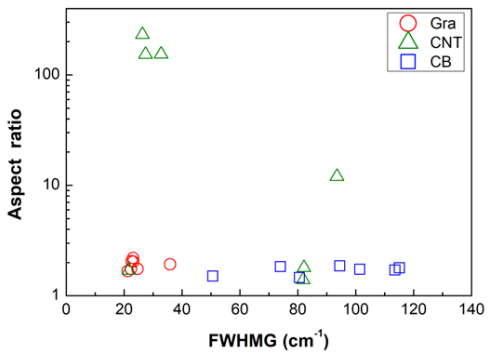
Gra
CNT
CB
Aspect ratio
FWHMG (cm-1)

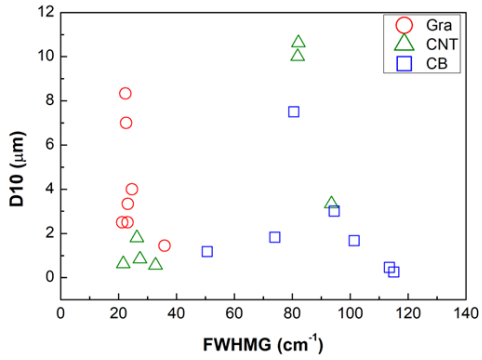
Gra
CNT
CB
D10 (μm)
FWHMG (cm-1)

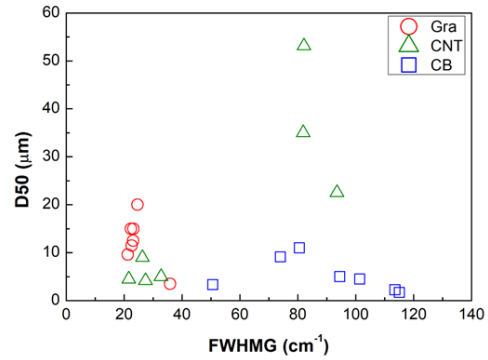
Gra
CNT
CB
D50 (μm)
FWHMG (cm-1)

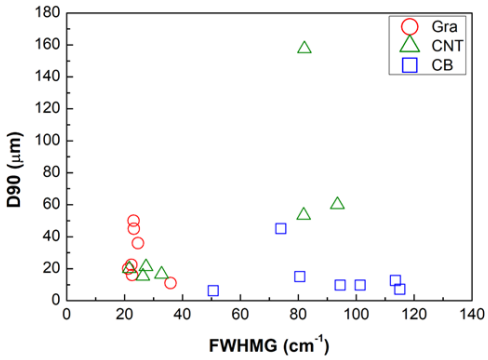
Gra
CNT
CB
D90 (μm)
FWHMG (cm-1)

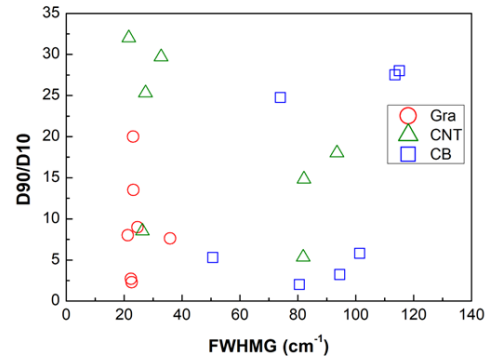
Gra
CNT
CB
D90/D10
FWHMG (cm-1)

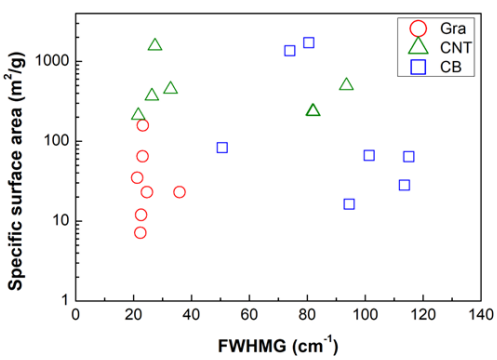
Gra
CNT
CB
Specific surface area (m2/g)
FWHMG (cm-1)

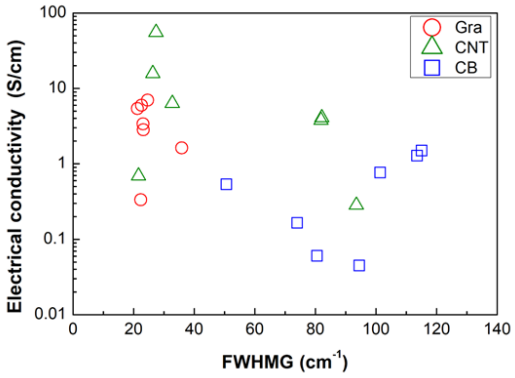
Electrical conductivity (S/cm)
FWHMG (cm-1)
Gra
CNT
CB

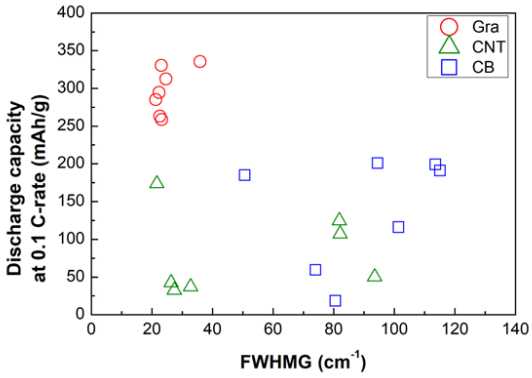
Discharge capacity at 0.1 C-rate (mAh/g)
FWHMG (cm-1)
Gra
CNT
CB

(f) To FWHM2D

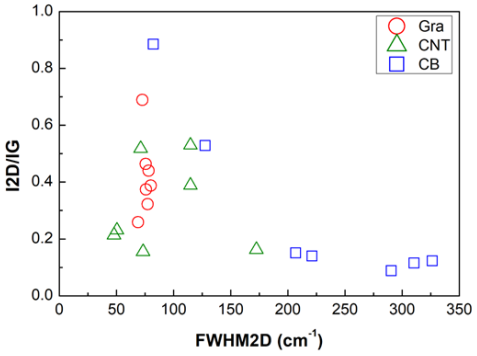
I2D/IG
FWHM2D (cm-1)
Gra
CNT
CB

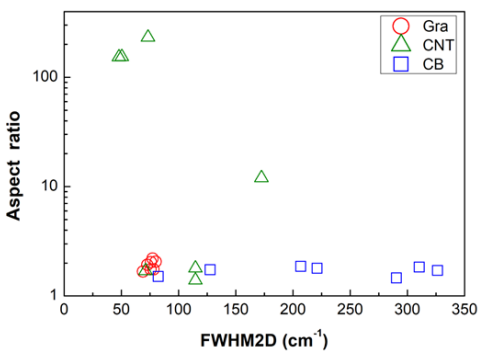
Aspect ratio
FWHM2D (cm-1)
Gra
CNT
CB

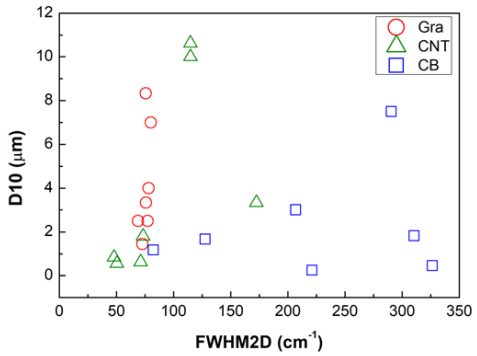
D10 (μm)
FWHM2D (cm-1)
Gra
CNT
CB

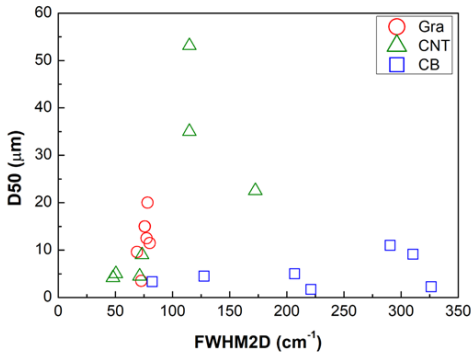
D50 (μm)
FWHM2D (cm-1)
Gra
CNT
CB

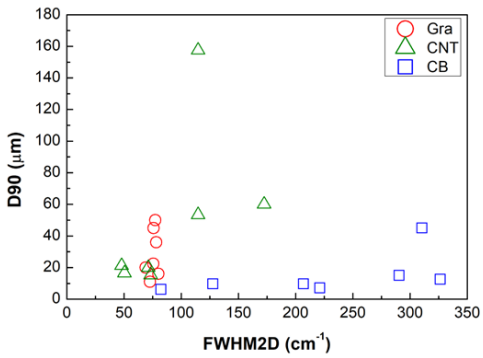
D90 (μm)
FWHM2D (cm-1)
Gra
CNT
CB

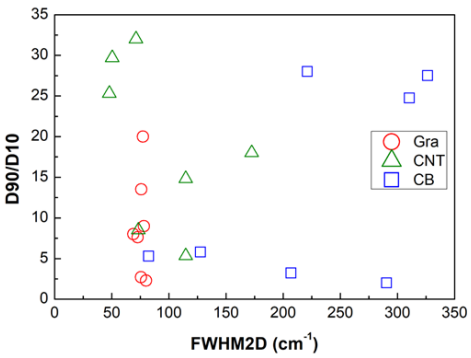
D90/D10
FWHM2D (cm-1)
Gra
CNT
CB

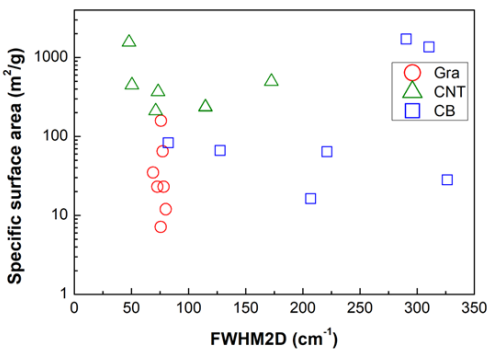
Specific surface area (m2/g)
FWHM2D (cm-1)
Gra
CNT
CB

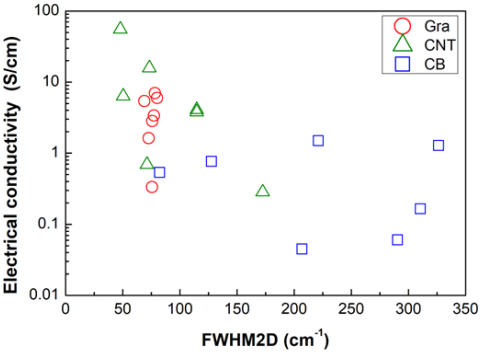
Electrical conductivity (S/cm)
FWHM2D (cm-1)
Gra
CNT
CB

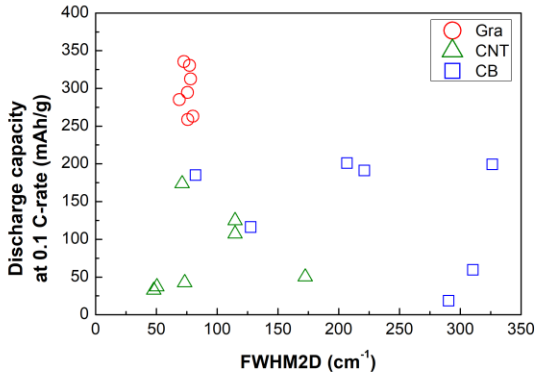
Gra
CNT
CB
Discharge capacity
at 0.1 C-rate (mAh/g)
FWHM2D (cm-1)
0
50
100
150
200
250
300
350
400

(g) To I2D/IG

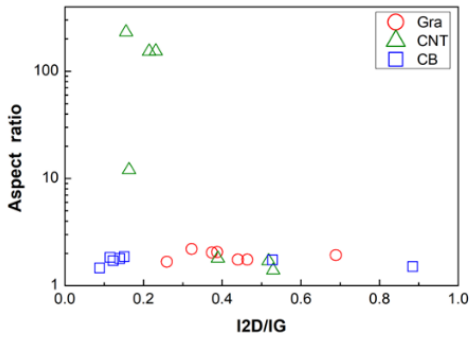
Gra
CNT
CB
Aspect ratio
I2D/IG

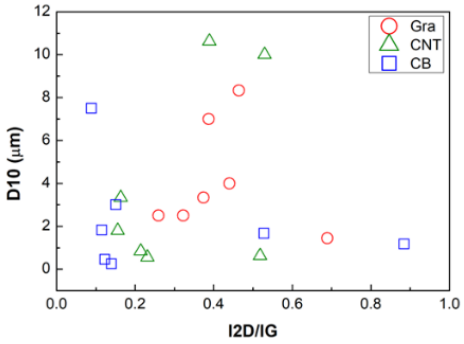
Gra
CNT
CB
D10 (μm)
I2D/IG

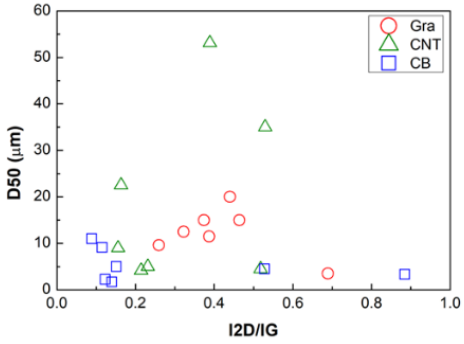
Gra
CNT
CB
D50 (μm)
I2D/IG

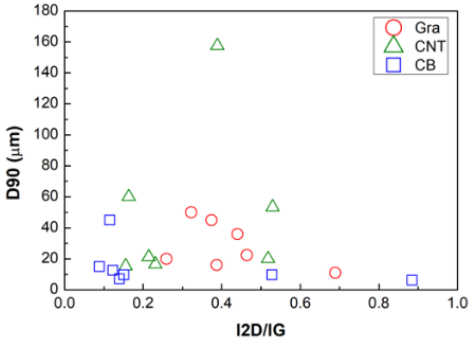
Gra
CNT
CB
D90 (μm)
I2D/IG

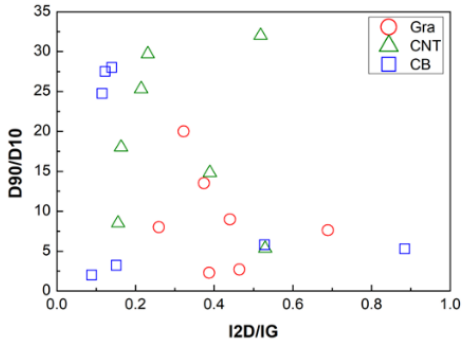
Gra
CNT
CB
D90/D10
I2D/IG

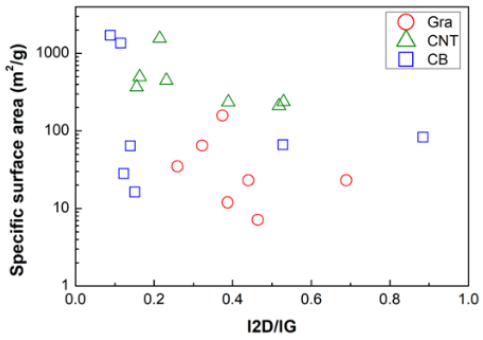
Gra
CNT
CB
Specific surface area (m²/g)
I2D/IG

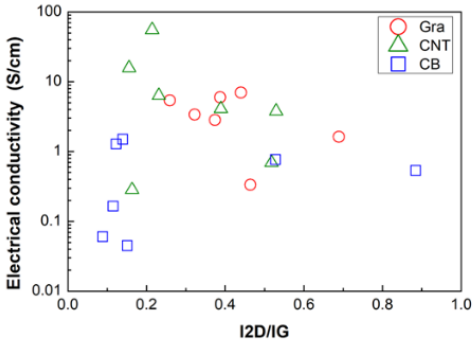
Gra
CNT
CB
Electrical conductivity (S/cm)
I2D/IG

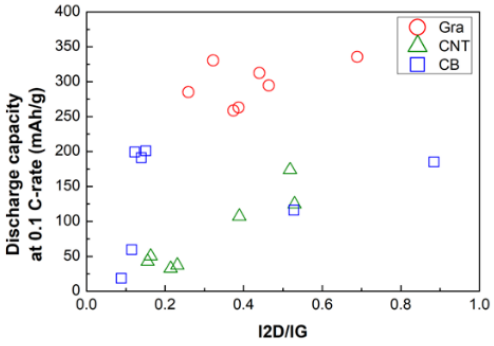
Gra
CNT
CB
Discharge capacity at 0.1 C-rate (mAh/g)
I2D/IG

(h) To aspect ratio

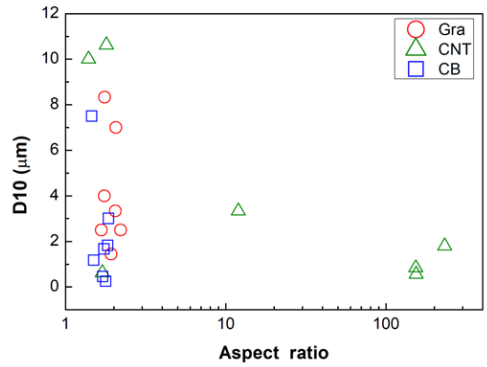

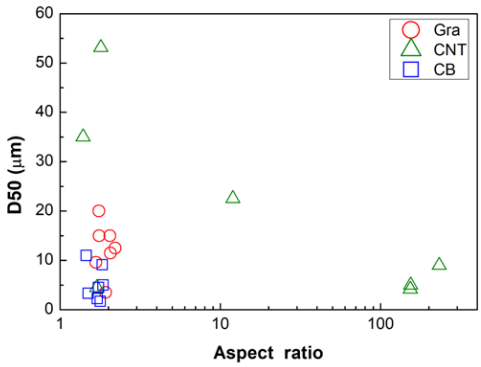

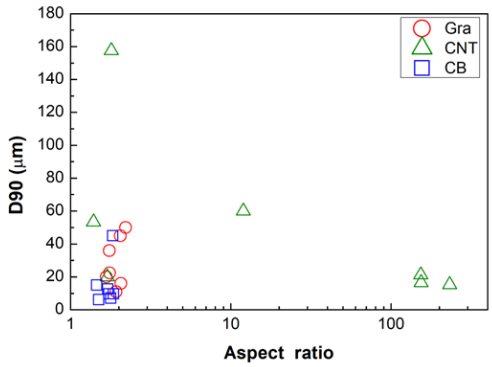

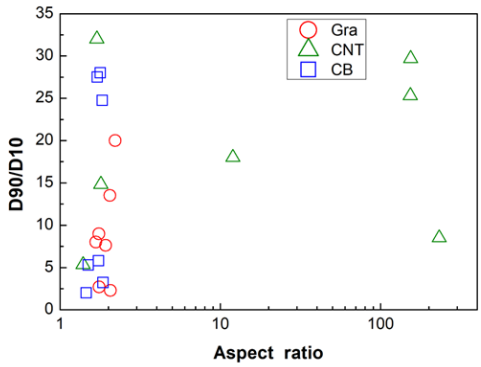

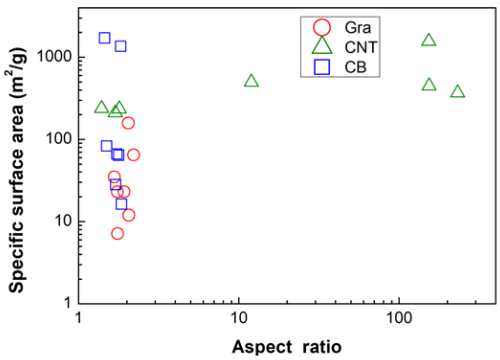

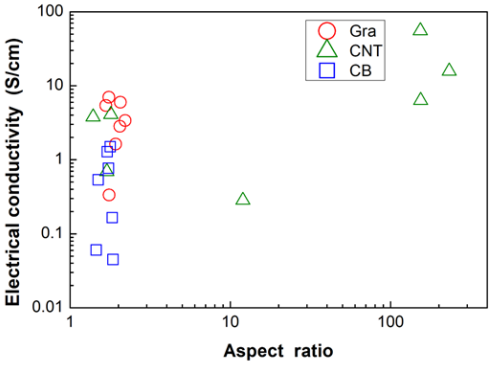

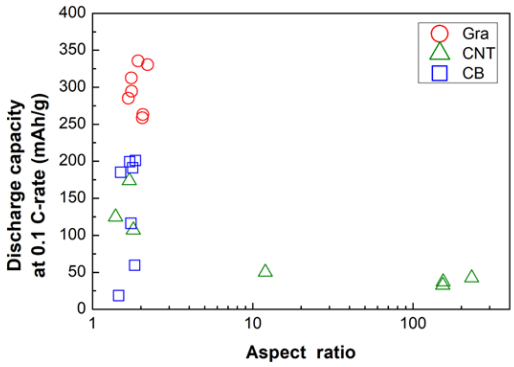

(i) To D10

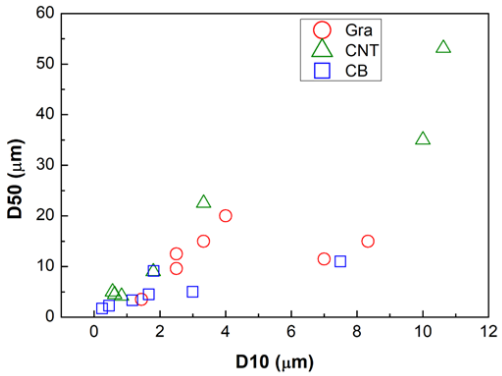
Gra
CNT
CB
D50 (μm)
D10 (μm)

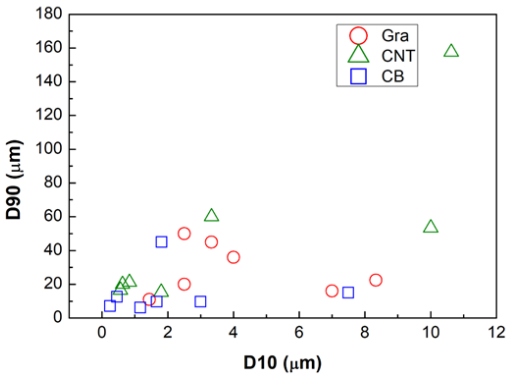
Gra
CNT
CB
D90 (μm)
D10 (μm)

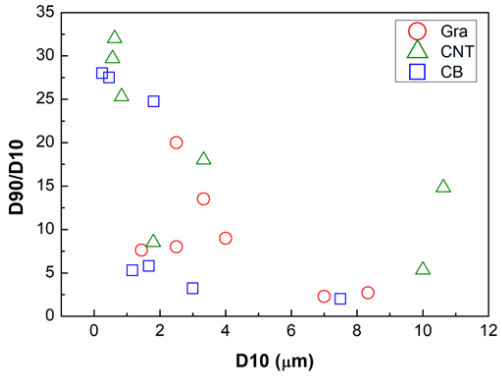
Gra
CNT
CB
D90/D10
D10 (μm)

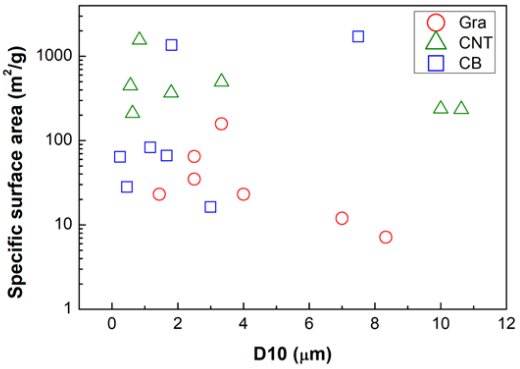
Gra
CNT
CB
Specific surface area (m²/g)
D10 (μm)

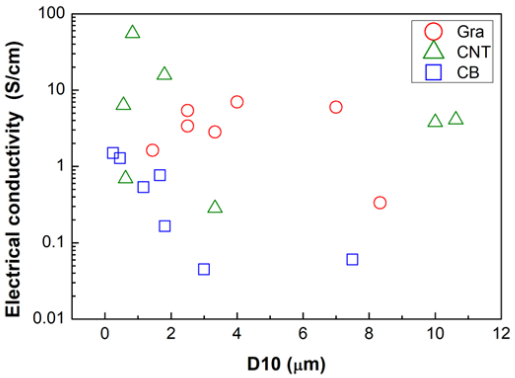
Gra
CNT
CB
Electrical conductivity (S/cm)
D10 (μm)

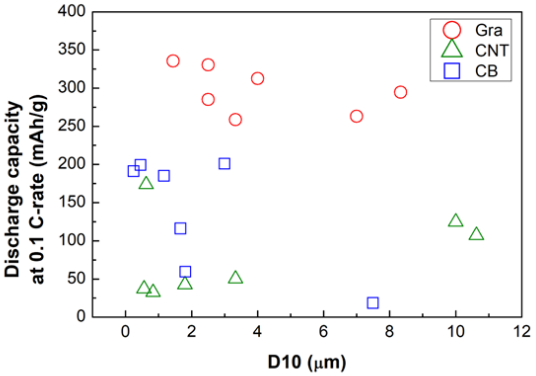
Gra
CNT
CB
Discharge capacity at 0.1 C-rate (mAh/g)
D10 (μm)

(j) To D50

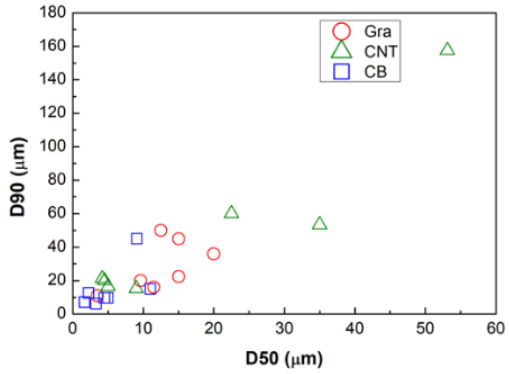
Gra
CNT
CB
D90 (μm)
D50 (μm)

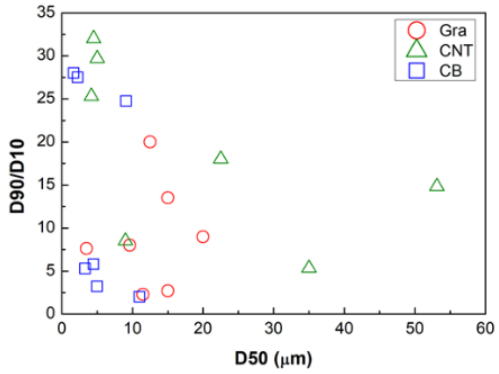
Gra
CNT
CB
D90/D10
D50 (μm)

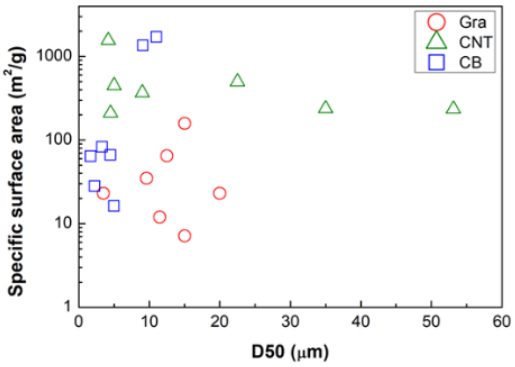
Gra
CNT
CB
Specific surface area (m²/g)
D50 (μm)

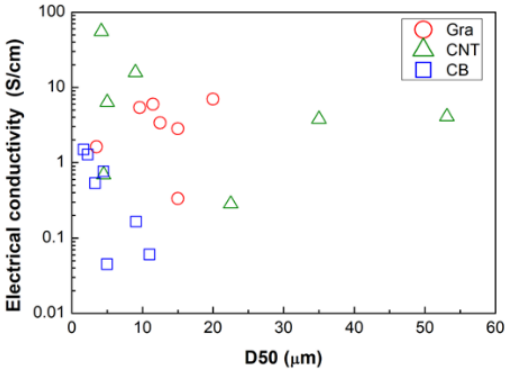
Gra
CNT
CB
Electrical conductivity (S/cm)
D50 (μm)

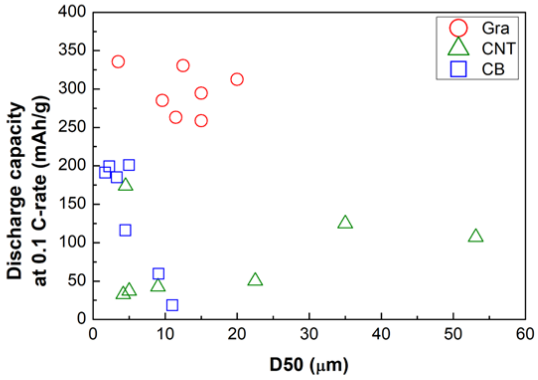
Gra
CNT
CB
Discharge capacity at 0.1 C-rate (mAh/g)
D50 (μm)

(k) To D90

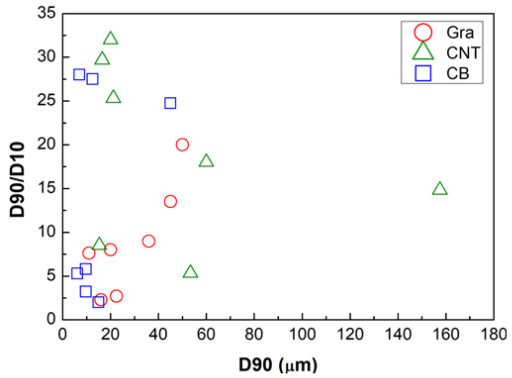
Gra
CNT
CB
D90/D10
D90 (μm)

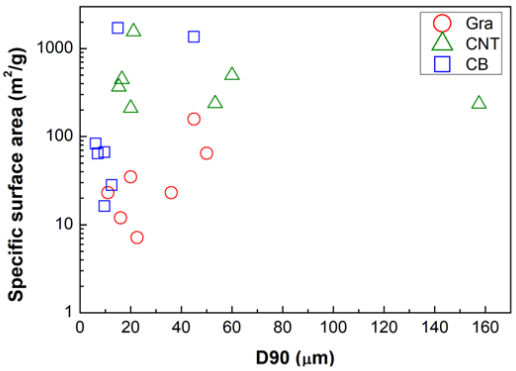
Gra
CNT
CB
Specific surface area (m²/g)
D90 (μm)

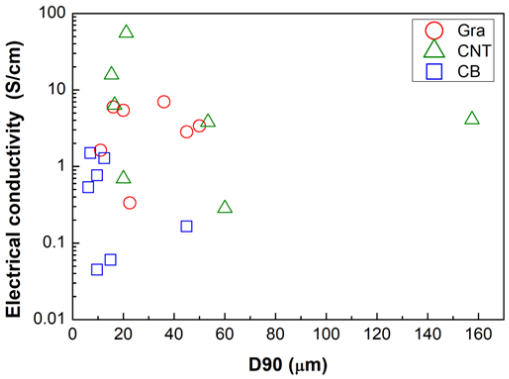
Gra
CNT
CB
Electrical conductivity (S/cm)
D90 (μm)

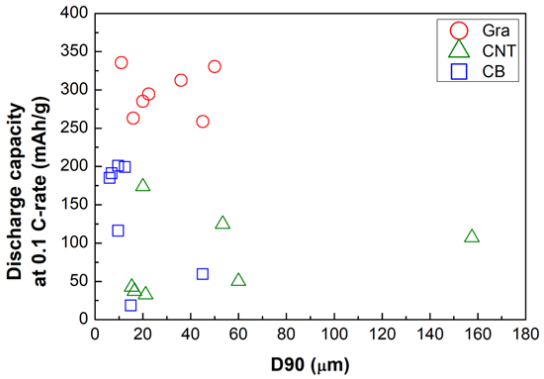
Gra
CNT
CB
Discharge capacity at 0.1 C-rate (mAh/g)
D90 (μm)

(l) To D90/D10

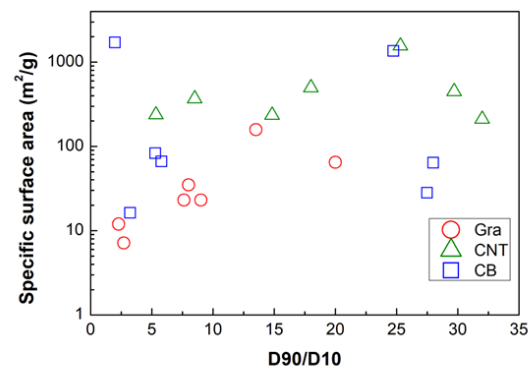
Specific surface area (m²/g)
1000
100
10
1
0
5
10
15
20
25
30
35
D90/D10
Gra
CNT
CB

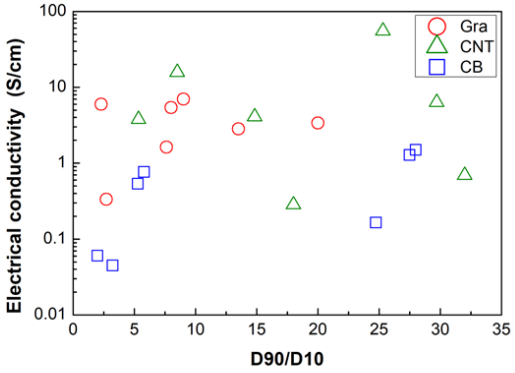
Electrical conductivity (S/cm)
100
10
1
0.1
0.01
0
5
10
15
20
25
30
35
D90/D10
Gra
CNT
CB

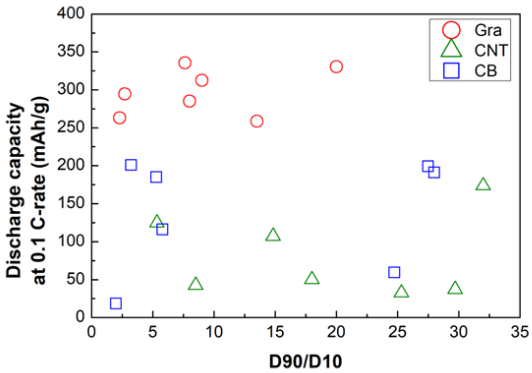
Discharge capacity at 0.1 C-rate (mAh/g)
400
350
300
250
200
150
100
50
0
0
5
10
15
20
25
30
35
D90/D10
Gra
CNT
CB

(m) To SSA

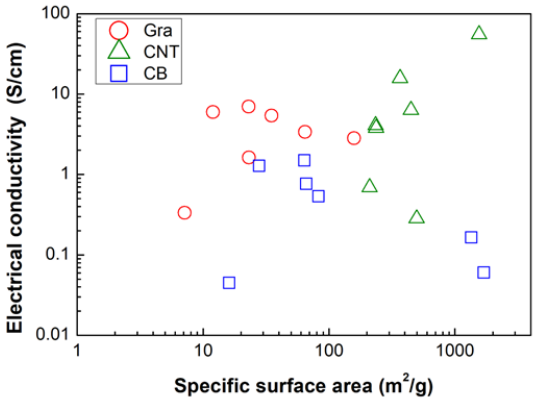
Gra
CNT
CB
Electrical conductivity (S/cm)
Specific surface area (m²/g)
100
10
1
0.1
0.01
1
10
100
1000

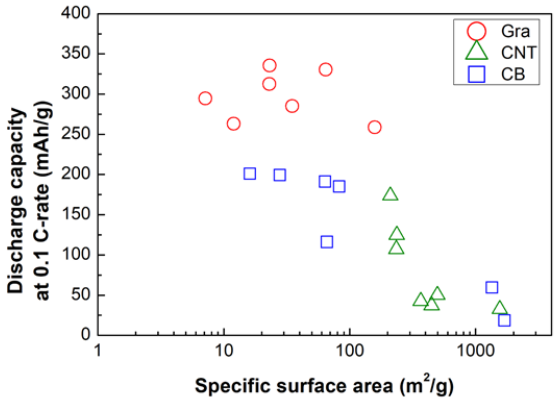
Gra
CNT
CB
Discharge capacity at 0.1 C-rate (mAh/g)
Specific surface area (m²/g)
400
350
300
250
200
150
100
50
0
1
10
100
1000

(n) To electrical conductivity

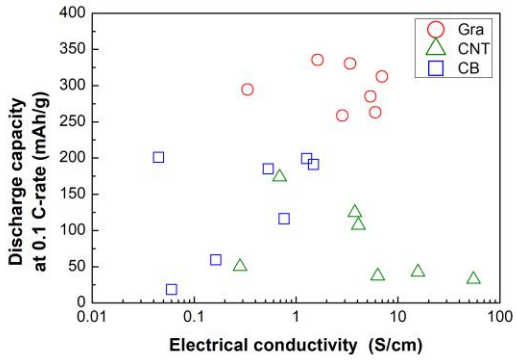

Chapter 5

Summary

Chapter 5. Summary

This research investigated the solid electrolyte, which has stability but lacks lithium-ion conductivity, and the anode material, which is responsible for the capacity related to mileage, from among the components of the electric vehicle battery, to the behavior of lithium-ion.

First, the lithium-ion conductivity was improved by introducing Zr ions to stable LiF used as a solid-state electrolyte in an easy and fast way. LiF has a weak conduction channel because it forms an FCC with a strong single bond of Li ions and F ions. However, when Zr ions, which are tetravalent cations, are introduced, they change to *P31m*, which becomes a laminated structure. Additionally, a vacancy site was created. These act as a two-dimensional diffusion channel on the nano scale, leading to an increase in the conductivity of lithium-ions. Changes in particles at the microscale are also expected to affect diffusion additionally. These effects are presumed to improve ion conduction because of a decrease in activation energy.

Next, the capacity and behavior of lithium-ion of carbon materials, which are frequently used as anode materials for batteries, were examined. In addition to graphite, a total of 21 carbon materials of various types, including SWCNT, were investigated in various ways through multivariate analysis. Among them, capacity was confirmed to be greatly affected by the crystallinity of c-axis and a-axis, and this was analyzed through Hill equation. According to the analysis, lithium-ion approaches in the same direction as (100) and (110) and the gap between graphene layers widens. The intercalation of lithium ions is then performed, and then the lithium-ion moves through the two-dimensional diffusion channel between the graphene layers in the basic plane direction. Therefore, the more sites to be intercalated, the more capacity is determined. Where intercalation is completed, the gap between the opened graphene layers is restored to the original interval. Finally, an equation for predicting the capacity using Lc, the most effective factor for explaining the capacity, was presented, and verified by previous studies. Based on phenomenon, a candidate structure with high Lc and relatively small La was suggested to increase capacity rather than a carbon material with existing structural stability.

The structural stability of the solid electrolyte and the carbon electrode is unfavorable to the diffusion of lithium-ion from the above results. However, if you take the two-dimensional diffusion

channel while taking structural stability, the "diffusion gate" becomes the most energy-intensive channel. This will be the most important diffusion path directly entering the diffusion of lithium-ion on the surface of the solid electrolyte and carbon electrode.

Achievement

List of publication

[Scientific papers related to doctoral thesis] (1 published and 1 submission)

1. Junmo Moon, Satita Thiangtham, Ruijie Zheng, Sicheng Liu, Chayanaphat Chokradjaroen, Yasuyuki Sawada, Nagahiro Saito. “The Liquid-Mediated Synthesis and Performance Evaluation of Li-Zr-F Composite for Ion-Conduction”. Journal of Energy and Power Technology 2023, Volume 5, Issue 1.

2. Junmo Moon, Hojong Yun, Junzo Ukai, Chayanaphat Chokradjaroen, Satita Thiangtham, Takeshi Hashimoto, Kyusung Kim, Yasuyuki Sawada, Nagahiro Saito. “Correlation function of specific capacity and electrical conductivity on carbon materials by multivariate analysis”. Carbon (Submitted)

[Presentation]

1. Kyusung Kim, Junmo Moon and Nagahiro Saito. “Synthesis of highly N-doped carbon dots through solution plasma for molecular detection”. Asian-European International Conference on Plasma Surface Engineering 2019, September 1-4, 2019.

2. Kyusung Kim, Junmo Moon and Nagahiro Saito. “Investigation of N-doped carbon dots synthesized by solution plasma for detecting nitro aromatic molecules”. Materials Research Meeting 2019, December 10-14, 2019.

3. Junmo Moon, Sangwoo Chae, Duangkamol Dechojarassri, Yasuyuki Sawada, Nagahiro Saito. “Sub-10 nm-scaled shell-layer of N-doped carbon for Li^+ pathway”. INTERFINISH2020, September 7-9, 2020.

4. 文　俊模, 蔡　尚佑, P. Pornaroontham, 齋藤　永宏. ″クラスター分析を用いたリチウムイオン電池向けのカーボン構造と電気伝導の関係″. 表面技術協会 September 10-11, 2020.

5. J. M. Moon, S. W. Chae, P. Pornaroontham, R. Naraprawatphong, X. Wang and N. Saito “Relationship between Carbon Structure-Electrical Conductivity by Cluster Analysis for Li-Ion Battery Application”. Pacific Rim Meeting, October 4-9, 2020.